Small Molecules Conjugated Silica Nanoparticles for Dual Targeting of Colon Cancer

by

Nayer Sultana

A dissertation submitted to the Graduate Faculty of
Auburn University
in partial fulfillment of the
requirements for the Degree of
Doctor of Philosophy

Auburn, Alabama
December 10, 2022

Keywords: Silica nanoparticles, Ligand conjugation, Receptor expression, Cancer targeting

Approved by

Allan E David, Chair, Associate Professor of Chemical Engineering
Xinyu Zhang, Professor of Chemical Engineering
Andrew Adamczyk, Assistant Professor of Chemical Engineering
Tim Moore, Professor of Drug Discovery and Development

Abstract

Colorectal cancer is categorized as the third most commonly diagnosed cancer and the second main reason for cancer death in the United States. The conventional treatments of colorectal cancer like surgery, chemotherapy and radiotherapy are hampered by recurrence, off target toxicity and tumor size respectively. Nanoparticles as targeted drug delivery carriers provide an alternative approach for the colon cancer treatment. Nanoparticle surface is modified with targeting ligands which recognize and bind to overexpressed specific biomarkers on cancer cells to deliver chemotherapeutic drug and imaging agent to the cancer cells. However, for efficient cancer targeting, the targeted receptors should be exclusively overexpressed by the cancer cells. Apart from the cell surface receptor, cancer targeting efficiency also depends on the targeting ligand's density, binding affinity and selectivity towards the targeted receptor. The targeting ligand should have high specificity and binding affinity towards the targeted receptor which will strengthen their interaction. According to literature, another way to increase the cancer cell targeting efficiency is to conjugate dual targeting ligands on the nanoparticle surface. While single targeted nanoparticles target only one type of cancer cell surface receptor, dual targeted nanoparticles simultaneously target two different types of cancer cell surface receptors which enhances targeting. So, the main objective of this project is to study the impact of nanoparticle dual ligand density on targeting of cells with different biomarker expression.

In this work, we have developed Silica nanoparticle conjugated with Hyaluronic Acid and Folic Acid to target colon cancer specific CD44 and Folate receptors respectively. We have synthesized the targeted nanoparticles using reverse micro-emulsion method along with EDC-NHS chemistry. The size of the particles characterized by Dynamic Light Scattering were in the range of 150-275nm with moderate dispersity. The morphology of the nanoparticles characterized by Transmission Electron Microscope showed their smooth spherical shape. Results from UV-Vis Spectrophotometer showed that Hyaluronic and Folic Acid conjugation on nanoparticle surface increased with their increasing concentration in the reaction system. The targeted nanoparticles showed >= 70% mammalian cell viability within the concentration and time range tested which proves them to be safe material based on literature. Based on our Flow Cytometry results, we have

used SW480 cell line as cell positive for both receptors, WI38 cell line as cell positive for CD44 receptor and Caco2 cell line as cell positive for folate receptor. Throughout the cellular uptake study we observed that increase in FA conjugation didn't have a significant impact on nanoparticle uptake increase at F:A≤7 and the highest cellular uptake was achieved at F:A=9 for FR positive cells which is the highest examined molar ratio. On the other hand, increase in HA conjugation significantly impacted the nanoparticle uptake. For CD44 positive cells, the cellular uptake increased with increasing HA conjugation but started declining beyond a certain point. So we concluded that the optimum H:A molar ratio for targeted nanoparticles was 0.5-0.75. Since the HA was longer than FA in length, it may have extended itself from the nanoparticle surface and became more accessible to the receptors. Results from the targeting studies demonstrated tremendous potential of the targeted nanoparticles as a promising candidate for theranostic approach.

Acknowledgments

First, I would like to thank my advisor Dr. Allan E. David for his motivation and mentorship throughout my Ph.D. project and in the preparation of this dissertation. Without his encouragement and guidance, this work would not have been completed. I have learnt a lot from him, not only about scientific research skills but also about being a better person in life.

I would like to thank my committee members Dr. Xinyu Zhang, Dr. Andrew Adamczyk and Dr. Tim Moore for their valuable comments and support. I would also like to thank Dr. Michael Miller for helping me with TEM characterization and taking the responsibility of the university reader for my dissertation. I would like to acknowledge Ms. Allison Church Bird for helping me with Flow Cytometer. I would like to acknowledge Dr. Michelle Kim and Dr. Stephen Ward for helping me with IHC staining.

I would like to thank all the current and past members of David Lab that include: Dr. Xin Fan, Dr. Prachi Sangle, Dr. Richard Cullum, Dr. Alan Hanley, Dr. Tareq Anani, Dr. Barry Yeh, Marjan Azadi, Braden Hahn, Shiva Rahmati and Pegah Tayeb. I would also like to thank Dr. Abhinav Sannidhi and Dr. Yuzhe Sun for their help in my research. I would also like to thank my undergrad Danika Lowe. It was wonderful to mentor her.

I would like to acknowledge Ms. Elaine Manning from the Chemical Engineering department for her help in various matters.

I would like to thank the Chemical Engineering Department of Bangladesh University of Engineering and Technology where I got my start, specifically Dr. Mohidus Samad Khan, my undergraduate research advisor. You have introduced me to the world of research. Without your help, I would not be where I am today. I would also like to acknowledge Dr. Syeda Sultana Razia, Dr. Shoukat Choudhury and Dr. Bayzid Kabir for their support of my higher studies.

Dear parents, siblings and husband – it's hard to express how thankful I am for all you've ever done for me. Thank you for always guiding me in the right direction. None of this would be

possible without your support. Last but not the least, I would like to thank all my friends here and back home for their relentless love and support over this PhD journey.

Table of Contents

List of Tables

List of Figures

List of Abbreviations

DLS	Dynamic Light Scattering
TEM	Transmission Electron Microscope
CD44	Cluster of Differentiation
FR	Folate Receptor
HA	Hyaluronic Acid
FA	Folic Acid
EDC	Ethylene dichloride
NHS	N-hydroxysuccinimide
PEG	Polyethylene Glycol
CHO	Chinese Hamster Ovary
HEK293	Human Embryonic Kidney
RWPE1	Human Prostate Epithelial
HCT116	Human Colorectal Carcinoma
HT29	Human Colorectal Adenocarcinoma
SW480	Human Colorectal Carcinoma
Caco2	Human Colorectal Adenocarcinoma

Chapter 1: Introduction

Colorectal cancer is categorized as the third most commonly diagnosed cancer and the second main reason for cancer death in the United States. Every year around 150,000 new cases of colorectal cancer and around 50,000 deaths due to it are recorded in the United States. The American Cancer Society estimates 151,030 new cases of colorectal cancer and 52,580 colorectal cancer related deaths during 2022 [1]. The 5-year survival rate for colorectal cancer depends on the cancer stage. It is about 90% for patients diagnosed with localized stage cancer and about 10% for patients diagnosed with metastatic cancer [2]. Colorectal cancer can start in the colon or rectal and can be named colon cancer or rectal cancer, based on their starting point. In my research work I am focusing on colon cancer. Colon cancer starts as a polyp in the inner layer of the colon [3] and develops slowly into cancer in 10 to 20 years of timespan [4].

The conventional treatment of colon cancer includes surgery, chemotherapy, radiotherapy and targeted therapy [2]. A combination of two or more treatment modalities is often suggested based on the cancer stage in order to achieve the best outcome. Surgery is the major treatment for patients with early stage colon cancer which removes the tumor along with some surrounding healthy tissue and adjacent lymph nodes [4]. But, surgery is challenging for metastatic colon cancer patients due to the spread of cancer in other body parts. Also, cancer recurrence after surgery can even cause death to patients [5]. Chemotherapy is the main therapeutic approach to colon cancer which kills fast growing cancer cells with different drugs or drug combinations. However, chemotherapeutic drugs cannot differentiate between cancer and normal cells. As a result, chemotherapy causes toxicity to normal cells and subsequent unwanted side effects by delivering drugs at the non-specific sites. Also, due to the non-specificity of chemotherapy, an insufficient amount of drug reaches the target site [6]. Targeted therapy is more specific in its activity which targets specific molecules expressed on the colon cancer cells but not the normal cells. These specific molecules are associated with colon cancer growth and targeted therapy works by blocking the growth and spread of the colon cancer cells. Also, targeted therapy can be applied to metastatic colon cancer patients. However, cancer cells can become resistant to targeted therapy. Resistance occurs when the targeted molecule itself undergoes alteration so that the targeted therapy does not attach to it or when the cancer cells follow an alternative pathway of growth independent of that targeted molecule [7].

Currently, there are two main targets for colon cancer: Vascular Endothelial Growth Factor (VEGF) protein and Epidermal Growth Factor Receptor (EGFR) protein. VEGF protein contributes to the formation of new blood vessel via a process called 'angiogenesis' to receive nutrients necessary for colon cancer growth. Anti-VEGF antibodies (Bevacizumab, Ramucirumab, Ziv-aflibercept) and anti-EGFR antibodies (Cetuximab, Panitumumab) are targeted therapies used to disrupt the colon cancer cell growth by binding to VEGF and EGFR proteins, respectively [4, 8]. These two targeted therapies are currently used for patients with stage IV metastatic colon cancer. Despite great promises, targeted therapy of colon cancer has not had any considerable impact on patient outcomes as there is no significant decline in the annual number of colon cancer related deaths in the United States.

Nanoparticles as targeted drug delivery carriers provide an alternative approach for the targeted treatment of colon cancer. Nanoparticles have received significant attention as targeted drug delivery carriers due to their biocompatibility, biodegradability, large surface area to volume ratio, prolonged circulation times, ability to carry a large amount of chemotherapeutic drug and easy surface functionalization [5, 9, 10]. The small sized nanoparticles provide a large surface area to volume ratio favorable for attaching multiple targeting ligands leading to enhanced targeting of cancer cells [11]. Ligand conjugated targeted nanoparticles can recognize and bind to overexpressed specific biomarkers on cancer cells [5, 8, 12, 13] and deliver chemotherapeutic drug to the cancer cells. This specific targeting increases the concentration of the cytotoxic drug at the cancer site and reduces non-specific toxicity [9, 10, 14]. Also, nanoencapsulation provides prolonged circulation time to the drug [15] by protecting it from degradation and clearance from the body [7, 12]. Targeted nanoparticles can also deliver the imaging agent to the cancer cells. However, multiple receptors targeting is necessary because of the heterogeneous nature of the cancer cell [16] and expression of some targeted receptors on normal cells [17]. Dual ligands are often conjugated on the nanoparticle surface to increase cancer cellular uptake. While single targeted nanoparticles target only one type of cell surface receptor, dual targeted nanoparticles simultaneously target two different types of cell surface receptors which enhances the targeting potency of the nanoparticles.

Several articles have reported the increase in cancer cellular uptake as a function of single ligand density. It has also been presented that dual targeted nanoparticles increase cancer cellular uptake

compared to single targeted nanoparticles. However, the effect of dual ligand density and its optimization on cellular targeting with variable biomarker expression have not been addressed. So, the goal of this project is to study the impact of nanoparticle dual ligand density on targeting of cells with different biomarker expression. To achieve this goal we have developed silica nanoparticles conjugated with hyaluronic acid and folic acid to target colon cancer specific CD44 and folate receptors respectively. To the best of our knowledge there is no report of targeting colon cancer cells with this dual targeted model system. Both CD44 and folate receptors have emerged as potential targets to treat colon cancer because of their overexpression by colon cancer cells compared to normal cells [18-21]. Hyaluronic acid and folic acid are attractive targeting ligands specific to CD44 and folate receptors respectively [22, 23]. We have hypothesized that, CD44 and folate dual receptor targeting of colon cancer cells will increase the cancer cellular uptake of nanoparticles as a function of surface ligand density. In addition to that, dual receptor targeted nanoparticles will internalize more nanoparticles into the cancer cells compared to the single receptor targeted nanoparticles by simultaneously binding to two different colon cancer cell surface receptors. So, the nanoparticle formulations will combine the benefits of dual targeting and enhanced ligand coverage.

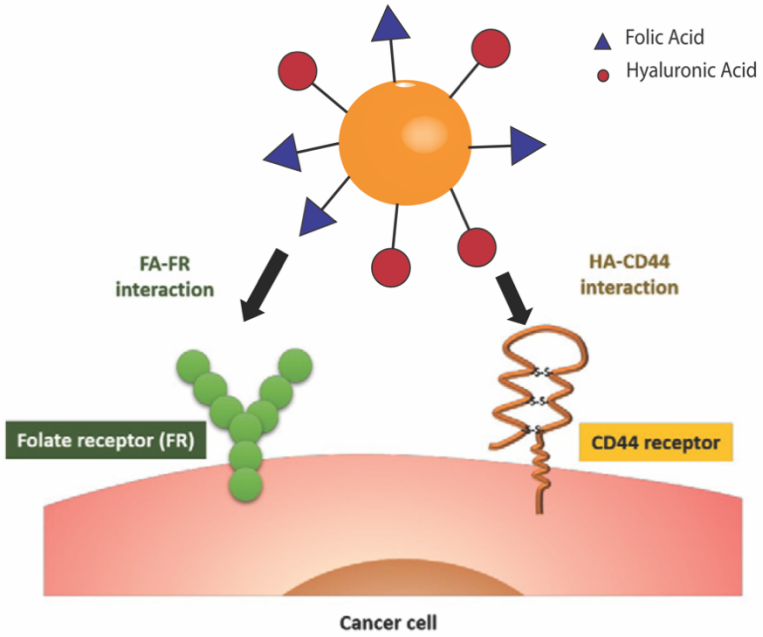

Figure 1 – Schematic representation of the novel dual targeted nanoparticle. Adapted with permission from Lee, J.-Y., et al. [24]

Chapter 2 reviews the background knowledge of cancer targeting strategies of nanoparticles, nanoparticle-cell interaction and ligand-receptor interaction. In chapter 3, we have discussed the synthesis and characterization of hyaluronic and folic acid conjugated dual targeted silica nanoparticles. In chapter 4, we have discussed the cytotoxic activity of targeted silica nanoparticles. In chapter 5, we have studied the receptor expression of different mammalian cell lines. In chapter 6, we have discussed the IHC staining on Neuroendocrine tumor. In chapter 7, we have explored the cellular targeting of targeted silica nanoparticles. Finally, Chapter 8 gives us an idea about the future direction of this project followed by Chapter 9, which is the summary of the entire project.

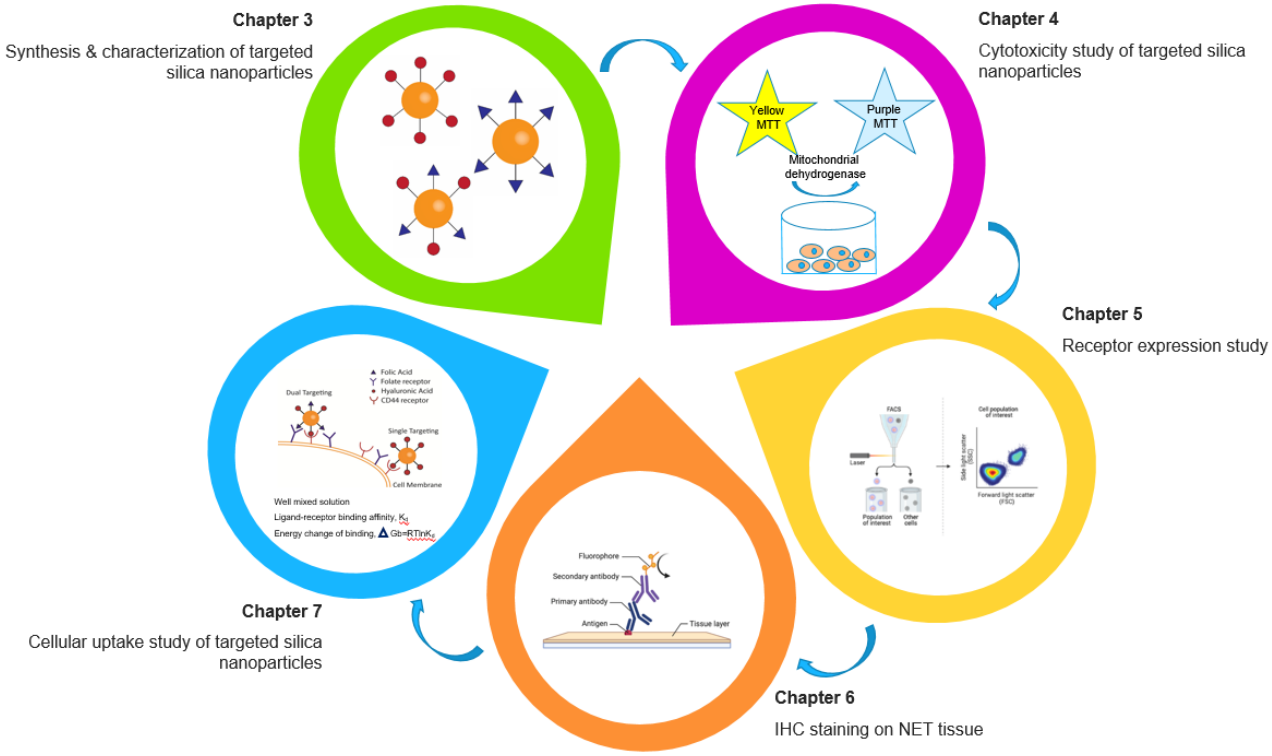

Figure 2 – Schematic representation of various topics discussed in this project. Some of the pictures are taken from BioRender and adapted from Xi, Li., et al. [25]

Chapter 2: Background

2.1 Cancer Targeting Strategies of Nanoparticles

For successful cancer treatment, therapeutic drug loaded nanoparticles must present at the cancer site which can take place by active or passive targeting. In active targeting, nanoparticles take advantage of the ligand-receptor interaction which leads to the receptor mediated uptake of the nanoparticles by the cancer cells. In passive targeting, nanoparticles accumulate at the cancer site due to the pathophysiological characteristics of the cancer cells [11].

2.1.1 Passive Targeting

Cancer cells have a faster proliferation rate than normal cells which is related to an increased rate of metabolism. This increased metabolic rate requires more nutrients and oxygen supply [26]. Cancer cells recruit the rapid formation of new blood vessels for the supply of these nutrients and oxygen [27] by a process called 'angiogenesis' (or neovascularization) [28]. This rapid angiogenesis results in a disrupted permeable leaky vasculature [29] which permits the nanoparticles to localize at the cancer site [30]. Additionally, cancerous tissues possess a poor lymphatic drainage system which allows longer retention time to the nanoparticles within the cancer site by resisting them from returning to the circulation [31]. Combination of leaky vasculature and poor lymphatic drainage causes Enhanced Permeability and Retention (EPR) effect [28] which is the major technique of passive targeting and subsequent nanoparticle accumulation at the cancer site [30]. However, passive targeting faces several challenges. For example, many drugs need to internalize into the cancer cells for effective treatment. In such a case, accumulation of drugs at the cancer site may not provide the expected therapeutic outcome [32]. Additionally, passive targeting is not effective for low molecular weight drugs as these drugs diffuse quickly into the blood circulation due to their lightweight. As a result, for low molecular weight drugs, accumulation at the cancer site is not possible for a longer time [31]. Also, degree of vascularization depends on cancer type. So passive targeting is not feasible for all types of cancer [33, 34]. These challenges of passive targeting can be overcome by attaching a targeting ligand on the nanoparticle surface [30].

2.1.2 Active Targeting

Active targeting of a specific cancer cell is achieved by attaching a targeting ligand on the nanoparticle surface that recognizes and binds to a specific receptor overexpressed on that cancer cell through receptor-ligand interaction [35]. This interaction leads to the receptor mediated endocytosis that causes cancer cellular uptake of nanoparticles [36, 37]. Thus, active targeting does not accumulate nanoparticles at the cancer site but it causes nanoparticle internalization into the specific cell [37]. This specific targeting also increases the intracellular drug concentration and reduces non-specific toxicity [9, 10, 14]. However, for efficient active targeting, targeted receptors should be exclusively overexpressed by the cancer cells but not the normal cells and this expression should be homogeneous on all the targeted cancer cells [9, 26, 31]. Multiple receptors targeting is also necessary because of the heterogeneous nature of the cancer cell [16] and expression of some targeted receptors on normal cells [17]. Apart from the cell surface receptor, active targeting efficiency also depends on the targeting ligand type, its size, density, binding affinity and selectivity towards targeted receptor [26, 38]. The targeting ligand should have high specificity and binding affinity towards the targeted receptor. It should also possess low immunogenicity. Low binding affinity of a ligand to its receptor may result in a reduced targeting efficiency [29]. In such a case, multivalent binding can help to improve the targeting efficiency which results in multiple ligand-receptor bond pairs [38]. Also, for enhancing ligand coverage and effective cellular targeting, adjusting the surface ligand density is essential [22]. However, increased ligand density and multivalency can promote protein adsorption on the nanoparticle surface which can lead to non-specific uptake by Reticuloendothelial System, thereby, reducing the targeting ability of the nanoparticle [26, 38]. In such a case, nanoparticles are covered with a hydrophilic coating like PEG to prevent protein adsorption.

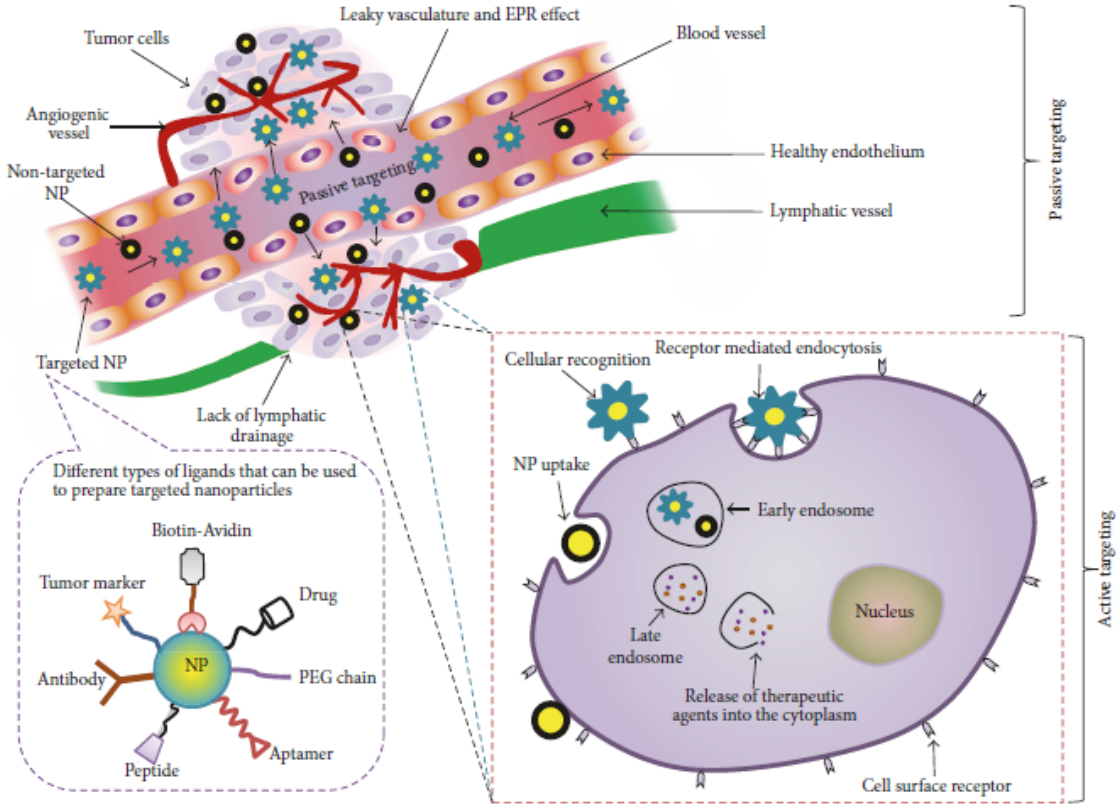

Figure 3 – Schematic representation of active and passive targeting. Reprinted from an open source article by Jahan, S.T., et al. [26]

2.2 Nanoparticles and Cell Interaction

A nanoparticle needs to pass the cell membrane in order to enter into a cell. The cell membrane protects the intracellular components by separating them from the extracellular environment and selectively controls the passage of ions, nutrients and small molecules to and from the cell [39, 40]. The cell membrane consists of a phospholipid bilayer of hydrophilic head (negatively charged phosphate group) and hydrophobic tail (carbon chain) [41]. This phospholipid bilayer makes the cell membrane an efficient selective boundary because its amphiphilic property is required for the entrance of a variety of small biomolecules into the cell [42]. The phospholipid bilayer contains proteins, cholesterol and lipopolysaccharides [43, 44] which help the cell to respond to the extracellular environment and communicate with other cells [45]. The selectively permeable cell membrane allows only specific molecules to diffuse across the membrane. Smaller and non-polar molecules like oxygen and carbon di-oxide easily diffuse through the membrane by Fickian

diffusion whereas large and polar molecules like ions are carried across the membrane through membrane transport channel proteins. Large nanoparticles, macromolecules and molecular assemblies travel into and out of the cell via endocytosis and exocytosis [46, 47]. Endocytosis depends on the receptor mediated interactions like clathrin or caveolin mediated endocytosis [48]. However, nanoparticles can cross the cell membrane via endocytosis without the receptor mediated interactions which involves deformation of the cell membrane due to nanoparticle adhesion on its surface causing full nanoparticle wrapping and subsequent uptake [45]. Another way to cross the cell membrane is to penetrate it without vesicle formation [49]. Cell penetrating peptides can provide this direct internalization of nanoparticles [50]. Other approaches to transport nanoparticles into the cells include the 'sponge effect' mechanism [51], direct microinjection [52] and use of electroporation [53].

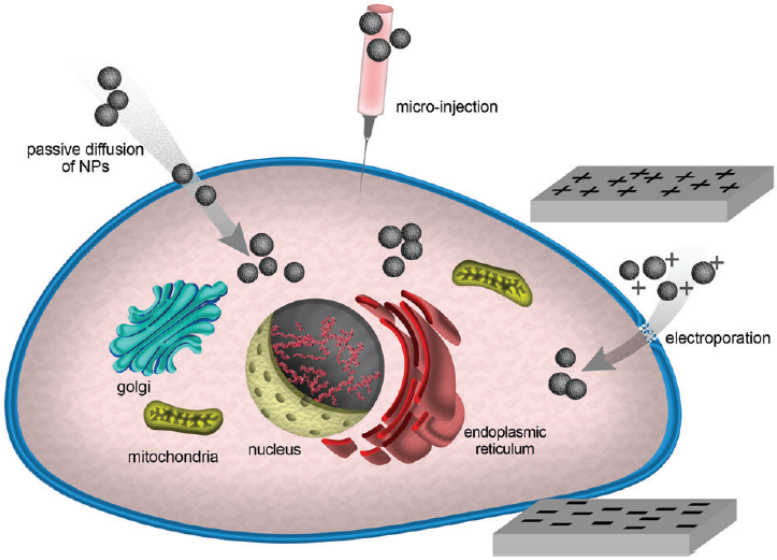

Figure 4 – Schematic representation of different approaches of nanoparticle-cell interaction. Reprinted with permission from Behzadi, S., et al. [42]

2.2.1 Endocytosis

Endocytosis of nanoparticles is a dynamic process [54] which occurs when the cell membrane engulfs the nanoparticle by fully wrapping it up. The wrapped particle is known as 'vesicle'. Nanoparticles enter the cells by different endocytic mechanisms such as phagocytosis, pinocytosis, clathrin or receptor-mediated endocytosis and clathrin or caveolae independent endocytosis [55].

Nanoparticles may localize in endosomes, lysosomes, cytoplasm, mitochondria or the nucleus, after entering into the cells, based on the nature of the nanoparticle.

2.2.1.1 Phagocytosis

Phagocytosis (cell eating) is a type of endocytosis that occurs when opsonins such as immunoglobins, proteins or other blood components get adsorbed on the nanoparticle surface, a phenomenon known as 'opsonization' [56]. Phagocytic cells of the Reticuloendothelial System (RES) such as macrophages then recognize and bind to the opsonized nanoparticles via receptor mediated interaction which leads to the internalization of the nanoparticles forming 'phagosome' [57]. Fc receptors, complement receptors, fructose receptors and scavenger receptors are some of the receptors that take part in phagocytosis. This non-specific uptake of opsonized nanoparticles by the Reticuloendothelial System (RES) or the Mononuclear Phagocyte System (MPS) removes them from the blood circulation and accumulates them in the liver or spleen from where the nanoparticles are quickly evacuated from the body [42]. Nanoparticles' physicochemical properties like size, shape and surface properties affect phagocytosis [57]. For example, larger nanoparticles, typically micron sized particles are more susceptible to phagocytosis. In a study, *Schafer et al.* reported higher phagocytic uptake of radio labelled albumin nanoparticles in the size range of 200-1500nm by human mononuclear cells [58]. In another study, *Tabata et al.* reported higher phagocytic uptake of polystyrene nanoparticles in the size range of 1000-2000nm by mouse peritoneal macrophages compared to smaller nanoparticles (<1000nm) [59]. Surface modification of nanoparticles with hydrophilic Polyethylene Glycol (PEG) can avoid opsonization and subsequent non-specific cellular uptake of the nanoparticles. PEG acts as a sterically shielding polymer that avoids opsonization by preventing protein adsorption [60].

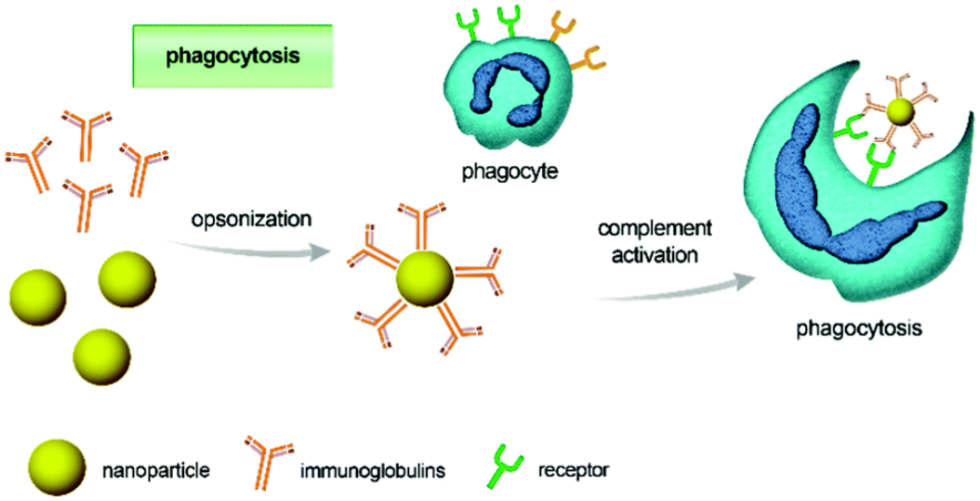

Figure 5 – Schematic representation of opsonization process. Reprinted with permission from Behzadi, S., et al. [42]

2.2.1.2 Pinocytosis

Pinocytosis (cell drinking) is of two types: Micropinocytosis and Macropinocytosis. Micropinocytosis takes place in the majority of the body cells. It includes small vesicle (0.1 micrometers in diameter) formation called 'caveolae' by budding from the cell membrane. It is caused by 'caveolin', a dimeric protein that binds to cholesterol. Micropinocytosis typically takes place in the white blood cells. It includes large vesicle (0.5 to 5 micrometers in diameter) formation by plasma membrane ruffles. Ruffles are elongated parts of the membrane that take up the extracellular fluid to form a vesicle and pull the vesicle into the cell.

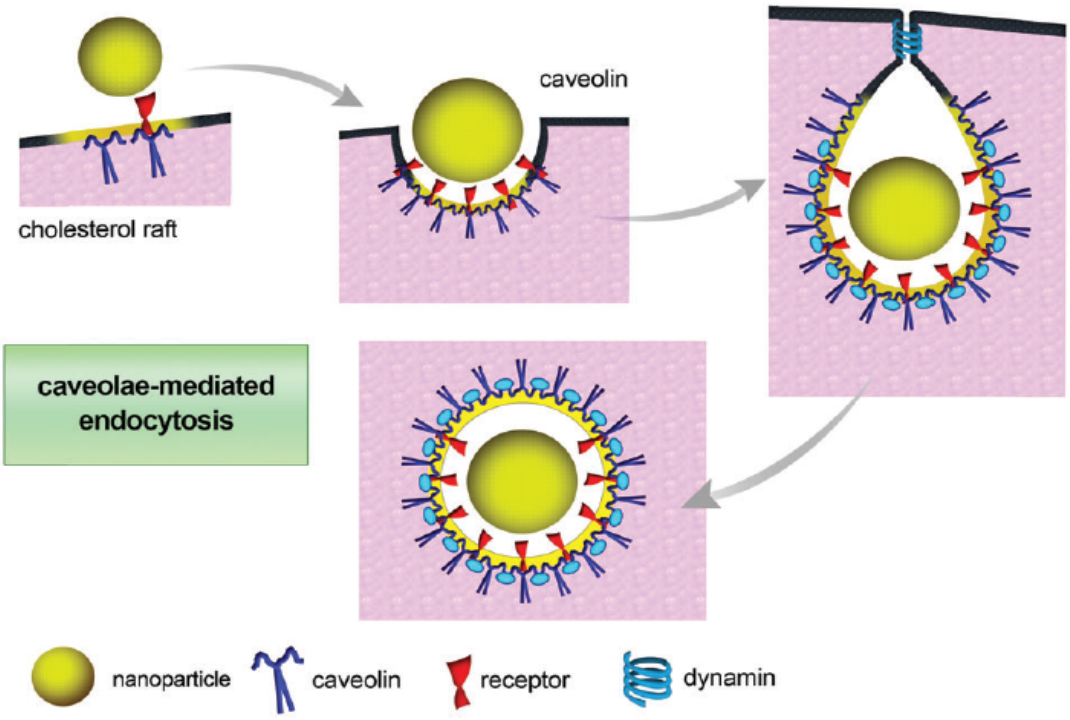

Figure 6 – Schematic representation of caveolae mediated endocytosis. Reprinted with permission from Behzadi, S., et al. [42]

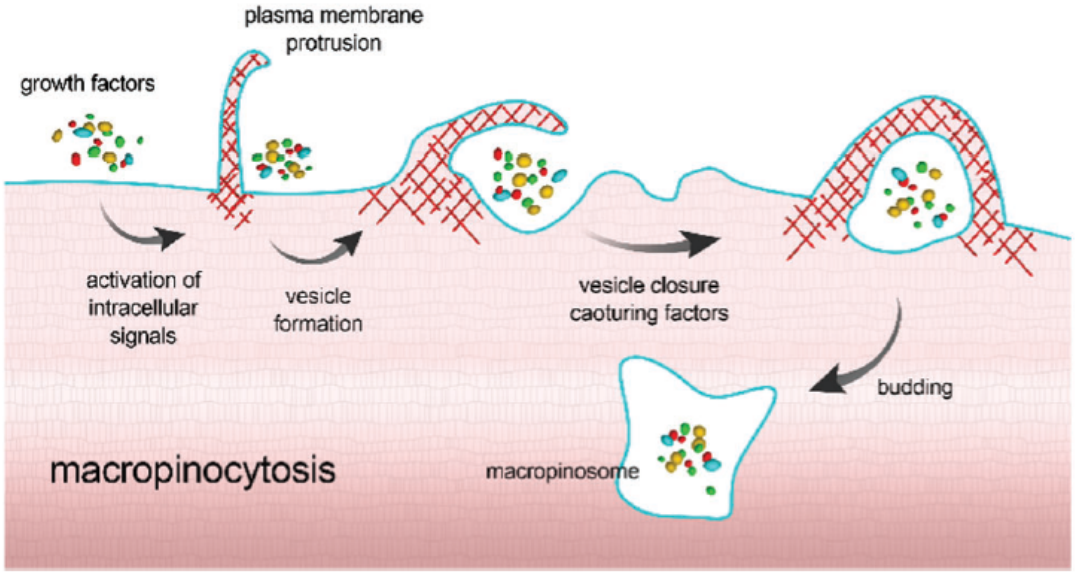

Figure 7 – Schematic representation of micropinocytosis. Reprinted with permission from Behzadi, S., et al. [42]

2.2.1.3 Receptor Mediated Endocytosis

In receptor mediated endocytosis, ligands conjugated on the nanoparticle surface recognize and bind to specific receptors on the cell membrane. The ligand- receptor conjugate moves along the membrane and localizes in a region called ‘clathrin coated pit’ which is covered by the protein ‘clathrin’. After the localization, ‘clathrin coated pit’ region is internalized by endocytosis forming a clathrin coated vesicle. This vesicle contains the ligand-receptor conjugate and the extracellular fluid. The clathrin coating is removed from the vesicle and it combines with an early endosome in the cytoplasm. The desired contents are delivered into the cell and the receptor recycles back to the cell membrane in a recycling endosome.

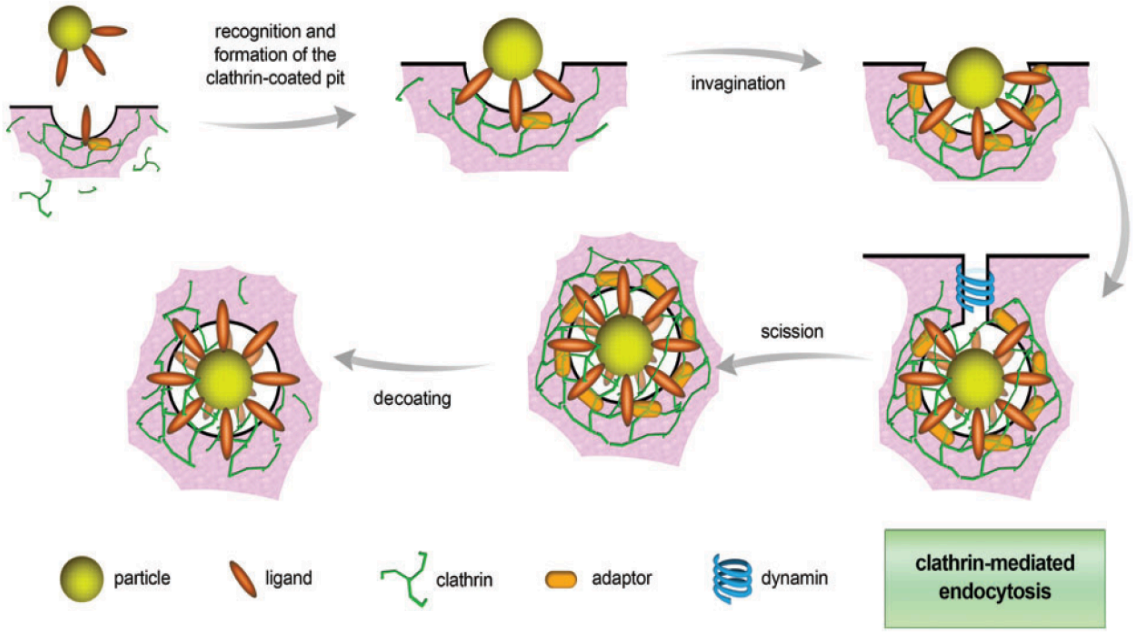

Figure 8 – Schematic representation of receptor mediated endocytosis. Reprinted with permission from Behzadi, S., et al. [42]

2.2.2 Factors Affecting Nanoparticle-Cell Interaction

Cellular internalization mechanism of nanoparticles helps to understand their biological fate which is of great importance in the field of nanomedicine [61]. However, this nanoparticle-cell interaction mechanism is a complicated process because a lot of factors (including physicochemical and biological) affect it [45]. Figure 8 shows these factors and the three interacting components.

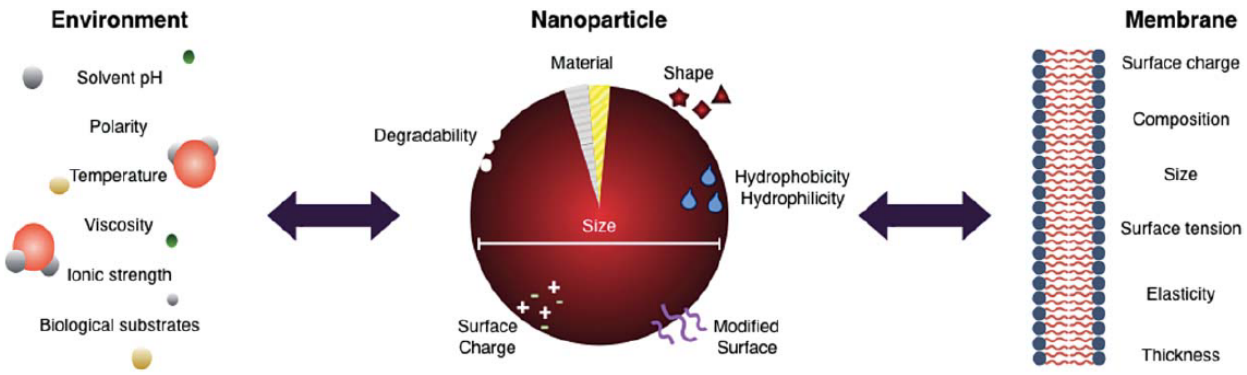

Figure 9 – Factors affecting nanoparticle-cell interaction. Reprinted from an open source article by Contini, C., et al. [45]

2.2.2.1 Biological Factors

Biological factors mainly include cell type and the protein corona which forms on the nanoparticle surface after it is introduced in the biological fluid.

2.2.2.1.1 Cell Type

Firstly, different cell types demonstrate different shapes which can produce different cellular responses during internalization of the nanoparticles. For example, human erythrocytes possess spherical shape whereas ependymal cells possess long, thin shape [62]. Secondly, different cell types express different cell surface receptors that affects cellular internalization of the nanoparticles. For example, macrophages express scavenger receptors that facilitates non-specific uptake of the nanoparticles [42] whereas colon cancer cells express folate receptors that uptakes the folate conjugated nanoparticles [19]. Thirdly, different lipid compositions of the cell membranes of different cell types may affect their membranes' physical properties and functionality. Finally, different cellular components have different effect on the nanoparticles. For example, lysosomes are acidic and make the nanoparticles undergo enzymatic degradation which results in a toxic state whereas cytoplasm is nearly neutral [54].

2.2.2.1.2 Protein Corona

Protein corona plays a major role in nanoparticle-cell interaction. When nanoparticles enter the blood circulation system, they are immediately surrounded by plasma proteins which form protein corona on the nanoparticle surface through a process known as 'opsonization' [63]. Proteins with high concentration (globular albumins, fibronectin, complement proteins, fibrinogen, immunoglobulins, and apolipoproteins) collide rapidly with the nanoparticles [64] and get adsorbed on the surface even with low binding affinity. As time passes, these low affinity proteins are substituted with high affinity proteins [65]. This protein corona changes the original surface properties of the nanoparticles and creates a new 'biological identity' of them [42] which can shield their receptor recognition and binding properties [49]. Additionally, this new identification of the nanoparticles influences their biodistribution and clearance [54] thereby, altering their destination in the body [66].

2.2.2.2 Physicochemical Factors

Physicochemical properties of the nanoparticle i.e. size, shape, hydrophobicity, surface charge and chemistry affect the nanoparticle-cell interaction.

2.2.2.2.1 Size

Nanoparticle size plays a major role in cellular internalization [67, 68]. Cellular internalization starts when the ligand conjugated nanoparticle binds to the specific cell surface receptor and the cell membrane engulfs the particle to form a vesicle via receptor mediated endocytosis [69, 70]. The thermodynamic driving force for the receptor mediated endocytosis is the receptor-ligand binding energy which results from the bond formation between the receptor and the ligand. This binding energy competes against the energy required for membrane bending [71, 72]. Receptor mediated endocytosis occurs when the ligand-receptor binding energy surpasses the membrane bending energy [73-75]. The minimum density of ligand-receptor conjugate for the nanoparticle internalization (ρ_{bond}) and the time required for the membrane to fully wrap the nanoparticle (T_w) depend on the nanoparticle size (r), receptor diffusivity on the membrane (D), elastic modulus of the membrane (k) and ligand-receptor binding energy (E_{bind}) and can be expressed by the two following quantitative equations [49].

$$\rho_{bond,min} = \frac{k}{r2 \times Ebind} \quad \text{and} \quad T_w = \frac{r2}{D}$$

From the equations, it is evident that it requires less time to engulf the smaller nanoparticles but they need higher ligand density to bind to enough receptors to exceed the membrane bending energy due to their higher curvature. On the other hand, larger particles take more time to be wrapped up but require less ligand-receptor conjugate to cause receptor mediated endocytosis due to their lower curvature. So, membrane bending is nanoparticle curvature dependent, therefore depends on the nanoparticle size [71]. There is a threshold particle size for causing membrane deformation and subsequent wrapping process which is ~50nm according to many experimental studies [76-78]. Receptor mediated endocytosis is energetically favorable for nanoparticles larger than the threshold size whereas receptor mediated endocytosis is limited for nanoparticles smaller than the threshold size as they cannot occupy enough receptor binding sites on the cell membrane to overcome the membrane bending energy barrier [42, 54, 72]. Also, very small nanoparticles are readily filtered and cleared from the body by kidney [12]. On the other hand, very large particles undergo phagocytosis and get cleared from the blood circulation [79]. Therefore, many studies have recommended nanoparticles of ~100nm size for biomedical application due to their favorable circulation time and tumor accumulation [80, 81].

2.2.2.2.2 Shape

Along with size, nanoparticle shape is another important factor for nanoparticle-cell interaction. Spherical nanoparticles show higher cellular uptake than rod shaped nanoparticles due to their lower radius of curvature [82] and less membrane wrapping time [49, 69, 83]. Ferrari and co-workers reported that isotropic spherical particles show higher cellular internalization compared to anisotropic ones like disk, rod and cube shaped particles [84, 85]. In a study, *Zhang et al.* reported that nanospheres are uptaken by the cells while nanodisks stick to the cell surface [86]. In another study, *Chithrani et al.* reported that the cellular uptake of 74nm and 14nm spherical gold nanoparticles were 5 and 3.75 times higher than the 74x14nm rod shaped gold nanoparticles respectively. For rod shaped nanoparticles, aspect ratio, the ratio of length to width of nanorod, is an important factor for cellular uptake. In the same study, *Chithrani et al.* reported that rod shaped gold nanoparticles with lower aspect ratio showed greater cellular uptake than the ones with higher aspect ratio [78].

2.2.2.2.3 Surface Charge

Surface charge of the nanoparticles also plays a major role in cellular internalization. The cell membrane has negative charge because of the phosphate group of phospholipid bilayer [41]. So, the positively charged nanoparticles exhibit more cellular uptake compared to the negative and neutral charged nanoparticles due to the attractive electrostatic interaction [54, 83, 87-91]. However, many studies have exhibited the cellular uptake of negatively charged nanoparticles [83, 90, 92]. *Patil et al.* have demonstrated lower protein adsorption and higher cellular uptake of negatively charged cerium oxide nanoparticles compared to the positively charged nanoparticles with increasing zeta potential of different pH solutions [93]. So, surface charge of nanoparticles partially contributes to the cellular uptake and there are many other factors of the nanoparticle like size, shape, protein adsorption and surface chemistry that affect the nanoparticle-cell interaction.

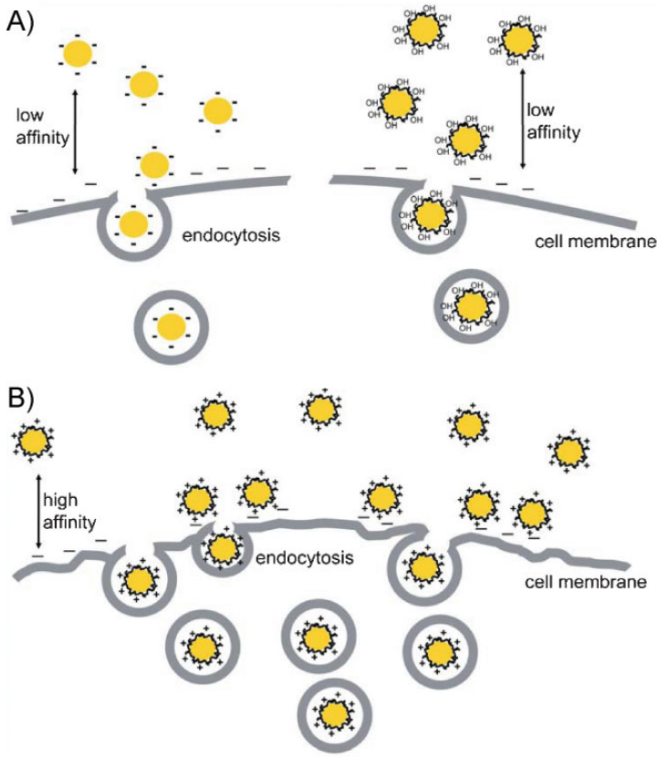

Figure 10 – Effect of nanoparticle surface charge on nanoparticle-cell interaction: (a) Negatively charged nanoparticles show low affinity towards cell membrane while (b) Positively charged nanoparticles show high affinity towards cell membrane. Reprinted with permission from Verma, A. et al. [83]

2.2.2.2.4 Surface Functionality

Nanoparticle surface functional groups also impact nanoparticle-cell interaction [42, 54]. Receptor mediated endocytosis is a common way of nanoparticle-cell interaction where affinity ligands conjugated on the nanoparticle surface recognize and attach to specific receptors on the cell membrane. The targeting ligand should have a high binding affinity for the targeted receptor [38] and produce enough ligand-receptor bond pairs to overcome the membrane bending energy barrier [71, 72]. Ligand-receptor binding can be increased with increasing ligand density on the nanoparticle surface [94-96]. However, after a certain ligand density, cellular uptake of the nanoparticles may decline with further increasing the ligand density as a result of steric crowding. The conformation and reactivity of the ligands are restricted with the addition of each ligand to effectively bind to the receptors [97, 98]. Also, increasing ligand density can promote protein adsorption on the nanoparticle surface which can lead to non-specific uptake by RES [26, 38]. In such cases, nanoparticles are covered with hydrophilic coating like PEG. PEG acts as a sterically shielding polymer that prevents protein adsorption [60]. However, increasing ligand density at the surface of PEG conjugated nanoparticles can shield the protective properties of PEG [26, 99, 100] leading to non-specific uptake and limited targeting effect. This issue has been reported by *Gu et al.* who have investigated the effect of increasing aptamer density on the PEG conjugated nanoparticle surface. They have reported a narrow range of ligand density when the nanoparticles were maximally targeted and stealth resulting in an efficient targeting of prostate cancer cell [100]. Therefore, ligand density optimization is necessary for efficient specific targeting and limited non-specific uptake [49].

2.3 Ligand and Receptor Interaction

The binding of a ligand to a receptor includes a recognition process followed by a non-covalent attachment [101, 102]. For a ligand-receptor interaction to occur, the ligand should be highly specific to the receptor and have a high binding affinity for it which will strengthen the interaction between them. The reversible interaction between a ligand, L and a receptor, R can be written as-

$$L + R \underset{k_{off}}{\overset{k_{on}}{\rightleftharpoons}} LR$$

where LR refers to the ligand-receptor complex. k_{on} (in $M^{-1}s^{-1}$unit) and k_{off} (in s^{-1} unit) refer to the association and dissociation rate constant respectively. At equilibrium, the forward reaction rate is equal to the backward reaction rate i.e. k_{on} [L][R] = k_{off} [LR] where [L], [R] and [LR] refer to the equilibrium concentration of the ligand, receptor and ligand-receptor complex. The association constant, K_a (in M^{-1} unit) is defined as-

$$K_a = \frac{kon}{koff} = \frac{[LR]}{[L][R]} = \frac{1}{Kd}$$

where K_d is the dissociation constant (in unit of M), a commonly used measurement of the binding affinity. Therefore, a high association rate along with a low dissociation rate provides a high association constant or low dissociation constant and, thereby a high binding affinity [103, 104].

The dissociation constant, K_d is related to the standard Gibbs free energy change of binding (ΔG_b) by the following Gibbs relationship-

$$\Delta G_b = -RTln(K_a) = RTln(K_d)$$

where R is the universal gas constant (8.3144 $JK^{-1}mol^{-1}$) and T is the temperature (^oK). From the above equation, it is evident that, lower the dissociation constant, the more negative the standard Gibbs free energy change of binding indicating stronger and more stable bond between the receptor and the ligand [101-104].

2.4 Silica Nanoparticle

Silica nanoparticle has been widely studied as a therapeutic delivery carrier because of its biocompatibility, low toxicity, systemic stability, relatively simple and low cost preparation [105-108]. In addition, controllable particle size, porosity and crystallinity make it suitable for various biomedical applications [105]. However, the main advantage of silica nanoparticles over other nanoparticles is the ease of surface modification to introduce different functional groups which are useful for prolonged circulation and specific targeting [105, 106, 108, 109]. Silica nanoparticle is 'Generally Recognized As Safe' (GRAS) by the United States Food and Drug Administration (US FDA) [110, 111]. Silica nanoparticles can have two forms-porous or nonporous. Silica nanoparticles can be used for drug encapsulation and delivery application; gene delivery

application; biosensor, bio-imaging devices, electronic substrates and thin film substrates production [112, 113].

2.4.1 Sol-Gel Synthesis

Flame synthesis, chemical vapor deposition, and sol-gel methods are some of the production techniques of silica nanoparticles [114]. The sol-gel method is the most commonly used among these techniques. The term "sol-gel" was first used in 1864 from Thomas Graham's study about silica gels [115]. Generally, the silica sol-gel process involves the transition from a colloidal silica sol suspension to a silica gel network [116]. Sols are colloidal suspension of solid particles in liquid [117] and gel is a rigid network with a liquid phase intercalated into its porous structure. In the silica sol-gel process, the silica nanoparticle is produced from the hydrolysis and condensation of a silica sol-gel precursor. Tetraethyl orthosilicate (TEOS) is the most commonly used silica precursor which undergoes hydrolysis when mixed with water. This hydrolysis reaction produces intermediates with the replacement of the ethoxy group (OC_2H_5) of TEOS by the hydroxyl group (OH). These intermediates contain silanol groups (Si-OH). Condensation reaction occurs after hydrolysis reaction where either two silanol groups or a silanol and an ethoxy group react and produce water or ethanol as a byproduct respectively. These condensation reactions form siloxane bonds (Si-O-Si) and known as either water condensation or ethanol condensation based on the byproduct [117-119]. Sol-gel reactions can be acid or base catalyzed with mineral acids and ammonium hydroxide are the most widely used ones. However, acid catalyzed reactions (slow hydrolysis) yield linear polymer chains that entangle to form gel network [117] whereas, base catalyzed reactions (faster hydrolysis) yield nanoparticles stable against gel transitioning [119].

Hydrolysis $Si(OC_2H_5)_4 + H_2O \rightarrow OH\text{-}Si(OC_2H_5)_3 + C_2H_5OH$

Water Condensation $(OC_2H_5)_3Si\text{-}OH + OH\text{-}Si(OC_2H_5)_3 \rightarrow (OC_2H_5)_3Si\text{-}O\text{-}Si(OC_2H_5)_3 + H_2O$

Ethanol Condensation $Si(OC_2H_5)_4 + OH\text{-}Si(OC_2H_5)_3 \rightarrow (OC_2H_5)_3Si\text{-}O\text{-}Si(OC_2H_5)_3 + C_2H_5OH$

The sol-gel method can be of two types- microemulsion and Stöber methods. Microemulsion system comprises a mixture of water, oil and amphiphilic compounds whereas Stöber method comprises a simple mixture of tetraethyl orthosilicate (TEOS) as a silica precursor, ethanol as a mutual solvent, water as a hydrolyzing agent and ammonium hydroxide as a base catalyst.

2.4.1.1 Microemulsion

Microemulsion is a colloidal dispersion consisting of a polar phase (mainly water), a nonpolar phase (mainly oil) and a surfactant. It is a macroscopically homogeneous, optically isotropic, and thermodynamically stable liquid solution [120]. There are two types of microemulsion, dispersed and bicontinuous. Dispersed microemulsion is further subdivided into water-in-oil (W/O) and oil-in-water (O/W) microemulsion. W/O microemulsion contains a low volume fraction of water dispersed in continuous oil phase; whereas O/W microemulsion contains a low volume fraction of oil dispersed in continuous aqueous phase. Bicontinuous microemulsion forms in a system of equal amount of water and oil. In all these types of microemulsion systems, a surfactant separates the polar and the nonpolar phase by forming an interfacial film [121].

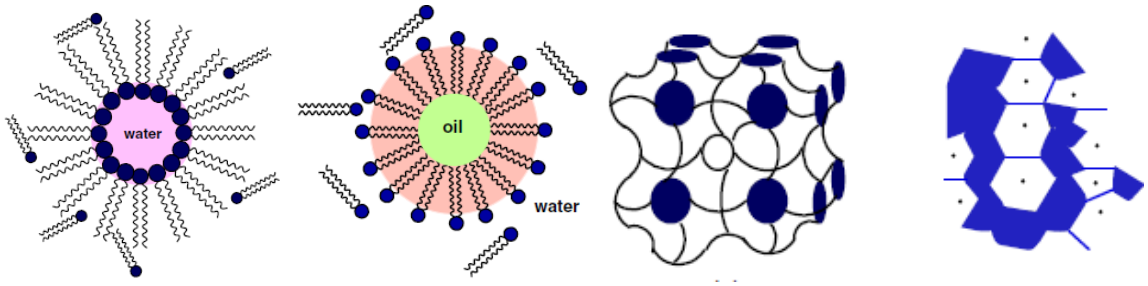

Figure 11 – Different types of microemulsion- (a) Water in oil microemulsion, (b) Oil in water microemulsion, (c) Bicontinuous microemulsion. Reprinted with permission from Malik, M.A. et al. [120]

Silica nanoparticle is produced by water in oil microemulsion (W/O) method, also known as reverse microemulsion method. W/O microemulsion is formed when a low volume fraction of water results in water droplets dispersed in a continuous oil phase [120]. An organic solvent, often an alkane serves as the oil phase [122]. The free water at the center of the microemulsion droplet is known as 'water pool' whose size can affect the nanoparticle size [120, 122]. The interface of the water in oil microemulsion is stabilized by a surfactant which decreases the interfacial tension [122, 123]. Surfactants are naturally amphiphilic. In W/O microemulsion, the hydrophilic polar head groups of the surfactant molecules point towards the aqueous core and the hydrophobic

nonpolar tail groups point towards the surrounding oil phase forming a reverse micelle. A co-surfactant is often used with the surfactant in order to further reduce the interfacial tension. Alcohols or amines in the range of C4 to C10 are usually used as co-surfactants that reduce the interfacial tension by offering a 'dilution effect' [120]. In addition, co-surfactant molecules enhance the mobility of the mono-molecular interface by continually moving between the dispersed and the continuous phase [124].

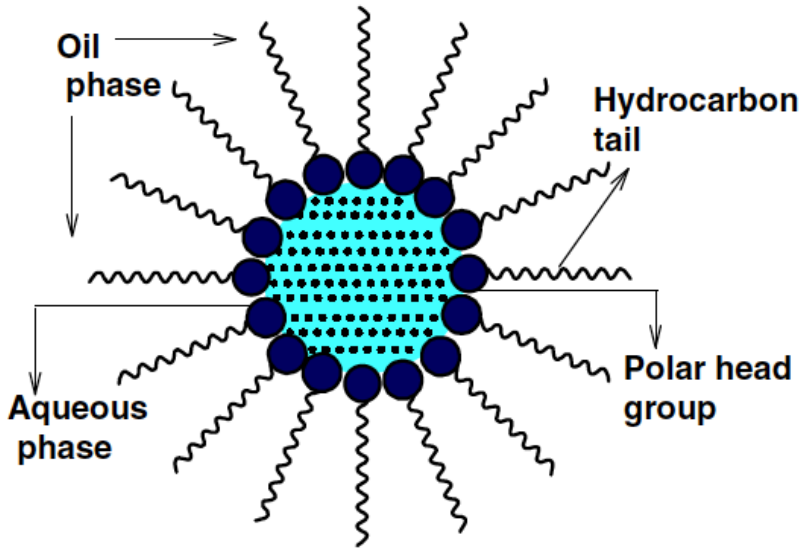

Figure 12 – Schematic representation of a water in oil (W/O) microemulsion droplet. Reprinted with permission from Malik, M.A. et al. [120]

The reverse microemulsion droplet acts as a nanoreactor where the nucleation and growth of silica nanoparticles occur in the presence of ammonium hydroxide [125]. Ammonium hydroxide occupies the aqueous core due to its polar nature [109]. Cyclohexane is often used as the oil phase which dissolves the hydrophobic silica precursor, TEOS. TEOS molecules diffuse from the continuous oil phase at the W/O interface and comes in contact with ammonium hydroxide in the water phase. As a result, TEOS molecules get hydrolyzed and monomers are formed. The hydrolyzed monomers undergo condensation either with other hydrolyzed monomers or with TEOS molecules to form polymers at the interface [125]. Nucleation occurs when the monomer occupancy number per droplet exceeds the critical nucleation number. So, based on this consideration, a large amount of nuclei will form with faster hydrolysis and condensation

reactions. Particle growth takes place either with the addition of monomers to the nuclei or via nuclei aggregation [126].

Reverse microemulsion produces spherical monodispersed silica nanoparticles of smaller size compared to the Stöber method [127, 128] and particle size can be simply controlled using various microemulsion parameters [109, 112]. Particles of various sizes produced by the microemulsion method can be used to encapsulate a broad range of organic and inorganic fluorophores [127]. However, the major challenge of reverse microemulsion method lies within the removal of surfactants from the final product [129]. This can be overcome by several washing steps.

2.4.2 Surface Functionalization of Silica Nanoparticle

Surface properties of silica nanoparticles affect their interaction with the biological system. So, surface functionalization of silica nanoparticles is of great importance to enhance their circulation time and colloidal stability in the biological fluids [130]. Also, surface functionalization of silica nanoparticles makes them available to diversified linking strategies [131] which can be used to attach biorecognition molecules on the silica nanoparticle surface to target specific receptors of the living systems [107].

Silica nanoparticle surface is mostly functionalized by covalent functionalization [130] which takes advantage of the widely used silane chemistry and introduces different functional groups like thiol (-SH), amine (-NH2) and carboxyl (COOH) groups on silica nanoparticle surface [127]. Covalent functionalization can be done either via ‘Grafting’ method or via ‘Co-condensation’ method. In the Grafting method, silica core is first prepared and then coated with organosilane containing the desired functional group. The organosilane undergoes hydrolysis to form silanol groups which condense with surface silanol groups of the silica nanoparticles to introduce the desired functional group [107]. However, many studies have reported self-condensation of the organosilane right after hydrolysis which is an undesired reaction [132, 133]. These self-condensates have the possibility of further condensation with the surface silanol groups of the silica nanoparticle forming a dense layer on the surface. Although this dense layer provides more functional groups for further linking reactions, it increases the overall size of the nanoparticles making it susceptible to phagocytosis. Additionally, surface functional groups cannot be accurately controlled in a replicative and reliable manner [107]. In the co-condensation method, also known

as ‘Direct or One-pot synthesis’ both the silica precursor and the organosilane undergo condensation simultaneously [134] resulting in uniform distribution of the functional groups [135]. However, faster condensation of the organosilane compared to TEOS buries most of the functional groups inside the particles and results in the unavailability of the functional groups on the silica nanoparticle surface. In this case, a time interval of at least 30 minutes is necessary between the addition of TEOS and the organosilane to achieve the desired outcome [109, 128].

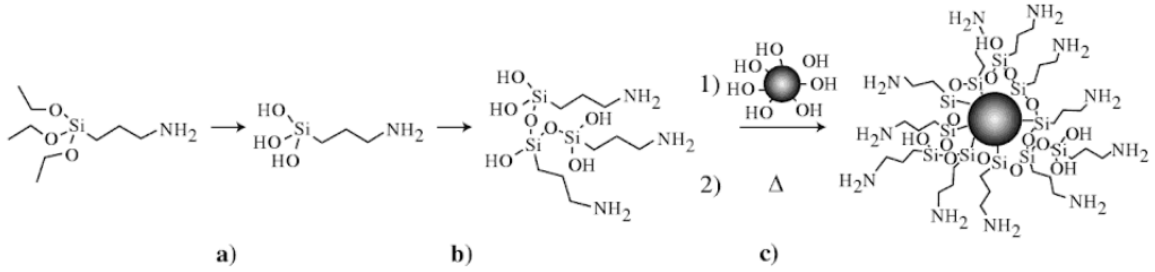

Figure 13 – Grafting process a) Hydrolysis, b) Self-condensation, c) Further condensation. Reprinted from an open access article by Hak-Sung Jung et al. [107]

Silica nanoparticle surface is mostly functionalized with silane coupling agents which have similar structures [$(OR)_3$-Si-R-] like the silica precursor, TEOS except that they have one terminal end of functional group. Also, the silane coupling agents follow the same hydrolysis and condensation reaction mechanisms of TEOS [131]. The $Si(OR)_3$ part of the silane-coupling agents bond with the inorganic materials while the functional group or (*R*-) part bonds with the organic materials [129]. 3-aminopropyl triethoxysilane (APTES), 3-mercaptopropyl trimethoxysilane (MPTS), Vinyltriethoxysilane (VTS) and various PEG-silanes are usually used as coupling agents for silica nanoparticles [105]

2.4.2.1 Silica Surface Functionalization with Amine Group

3-aminopropyltriethoxysilane (APTES) and 3-aminopropyltrimethoxysilane (APTMS) are the most commonly used amine precursors. They are used to introduce amine groups on the silica nanoparticle surface either via co-condensation or grafting method. They have similar structures like TEOS except that they have one terminal end of amine group and they follow the same hydrolysis and condensation reaction mechanisms of TEOS [136]. However, these reactions are

sensitive to silane concentration, reaction time, temperature, solvent polarity, and the amount of water [137]. Amine modified silica nanoparticles are used in composite materials, catalysts, medical diagnostics and biochemistry [134]. Also, they have applications in gene delivery, plasmid DNA transport, capture and release of bacteriophage viruses [138].

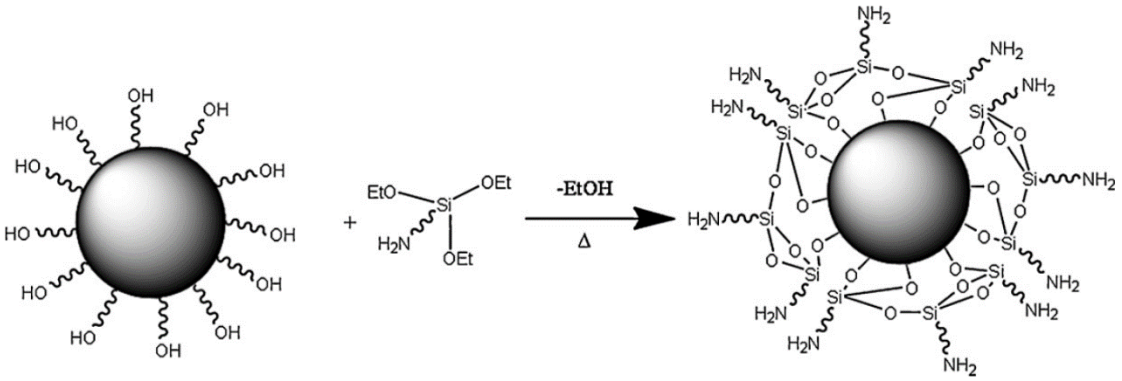

Figure 14 – Schematic representation of silanization reaction of APTES with silica nanoparticle. Reprinted with permission from Thanh, N.T. and L.A. Green [139]

2.4.2.2 Silica Surface Functionalization with PEG Group

PEG is a hydrophilic, neutral polymer of ethylene oxide monomers. It is non-toxic and FDA approved [140]. Silica nanoparticle surface is functionalized with PEG by a process known as pegylation. For pegylation, silica nanoparticle surface is first functionalized with reactive groups like amino, carboxyl, thiol or epoxy groups. These functional groups then react with mPEG bearing stable reactive groups to covalently conjugate mPEG on the silica nanoparticle surface. Amino group is the most preferred reactive group for the first step to link PEG on the silica nanoparticle surface due to its stability and mild reaction conditions [141]. PEG increases hydrophilicity on the nanoparticle surface and provides stealth properties to them which avoids interaction with the proteins and subsequent non-specific uptake. So, pegylation increases the circulation time of the nanoparticles and prevents their clearance from the body [142-146]. Protein resistance property of PEG depends on its chain length and surface grafting density [142]. PEG with longer chain length and higher grafting density provides greater protein resistance [144]. Pegylation also enhances the stability of the nanoparticles in the biological fluids by creating steric distance between them and subsequently reducing particle aggregation. Additionally, pegylation increases the solubility of the

nanoparticles in the biological fluids because of the presence of hydrophilic ethylene glycol units in PEG [105, 143, 144].

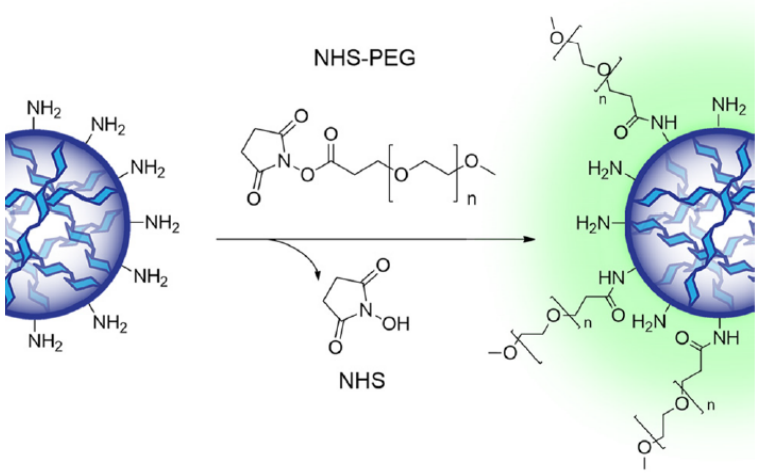

Figure 15 – Schematic representation of nanoparticle surface modification with mPEG-NHS. Reprinted with permission from Bamberger, D., et al. Copyright 2017, American Chemical Society [147]

2.4.2.3 EDC-NHS Chemistry

EDC-NHS chemistry is a well-established and versatile method of crosslinking primary amines to carboxyl groups with the use of carbodiimide compounds. Carbodiimide compounds activate carboxyl groups for direct reaction with primary amines via amide bond formation. EDC (1-Ethyl-3-(3-dimethylaminopropyl)carbodiimide) and DCC (Dicyclohexylcarbodiimide) are the two most widely used carbodiimides. Water-soluble EDC is used for aqueous crosslinking and the water-insoluble DCC is used for non-aqueous organic synthesis methods.

EDC reacts with the carboxylic acid groups to form an active O-acylisourea intermediate (Figure 38) which is easily replaced by nucleophilic attack from the primary amine groups in the reaction mixture. The primary amine forms an amide bond with the original carboxyl group and releases an EDC by-product as a soluble urea derivative. The O-acylisourea intermediate is unstable in aqueous solutions and if it fails to react with an amine group, hydrolysis of the intermediate occurs which regenerates the carboxyl and releases an N-unsubstituted urea. EDC crosslinking is effective in acidic (pH 4.5) conditions. However, phosphate buffers and neutral pH (up to 7.2) solutions are

also suitable for the reaction but with lower efficiency. In this case, increasing the EDC concentration in the reaction mixture can be effective.

In order to improve the reaction efficiency, N-hydroxysuccinimide (NHS) or its analog sulfo-N-hydroxysuccinimide (Sulfo-NHS) is frequently added in the EDC coupling reaction for efficiency enhancement [148]. EDC combines NHS to carboxyl group and forms a dry-stable amine-reactive NHS ester (Figure 39) which is considerably more stable than the O-acylisourea intermediate and allows efficient conjugation to the primary amines with the release of NHS at physiological pH. Therefore, the concentrations of the coupling agents EDC and NHS need to be optimized in order to ensure effective conjugation of hyaluronic acid and folic acid on the nanoparticle surface.

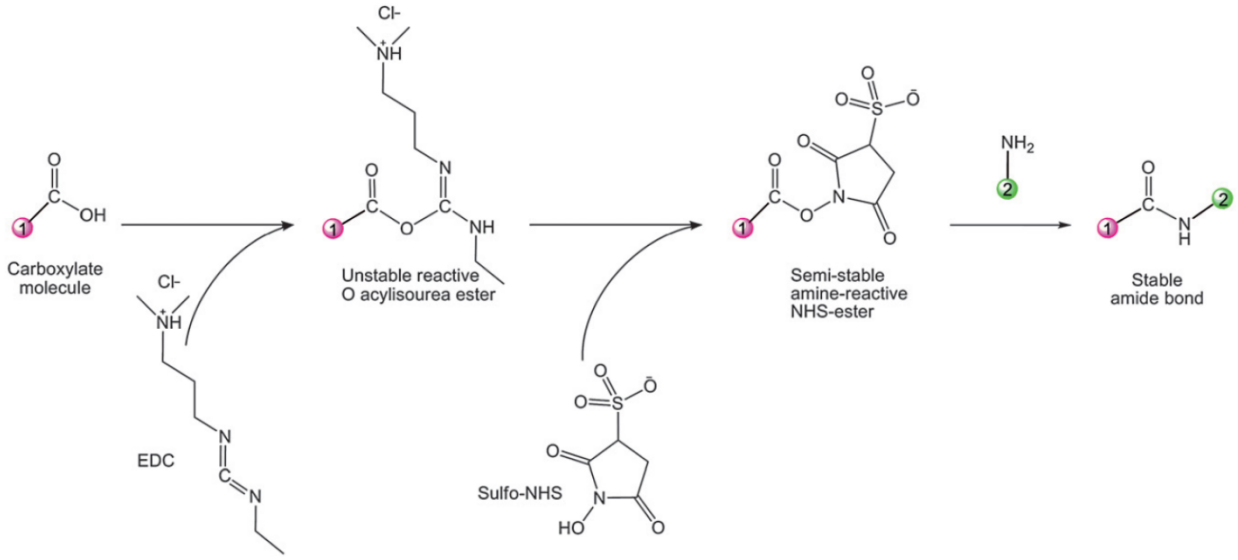

Figure 16 – EDC-NHS crosslinking reaction scheme. Reprinted with permission from Bart, J., et al. [149]

2.5 CD44 Receptor and Hyaluronic Acid

CD44 or Cluster of Differentiation receptor is a single chain transmembrane glycoprotein with molecular weight in the range of 80-250kDa [20, 22, 150, 151]. It shows higher level of expression on many cancer cells including ovarian, breast, lung, pancreatic and colon [22, 151, 152] compared to the normal cells and its density increases with the cancer stage. It plays a major role in many cellular processes like cell signaling, cell proliferation, differentiation, migration, angiogenesis,

tumor invasion and metastasis [153-155]. It has three domains- extracellular amino terminal domain, stem region and carboxyl terminal cytoplasmic domain. The amino terminal domain consists of disulfide bonds (SS) necessary for hyaluronic acid binding [156, 157] which is highly specific to the CD44 receptor.

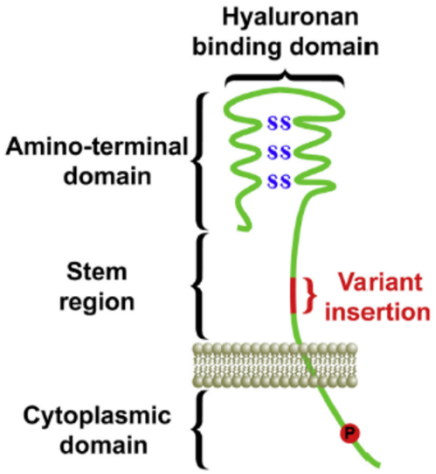

Figure 17 – Key domains of CD44 receptor. Reprinted with permission from Zavros, Y. [156]

Hyaluronic acid is a natural linear polysaccharide made of alternating units of *N*-acetyl-d-glucosamine and D-glucuronic acid disaccharides [106, 154, 158]. This vital constituent of extracellular matrix exists [151, 159, 160] in various sizes and possesses excellent properties including biocompatibility, biodegradability, hydrophilicity, non-immunogenicity, non-toxicity, high availability and low cost [17, 161, 162]. Additionally, it contains various functional groups like hydroxyl and carboxyl suitable for further functionalization [26, 163, 164]. Hyaluronic acid shows strong affinity towards CD44 receptor and is a potential targeting ligand for the development of CD44 overexpressing cancer cell targeting drug delivery system [165, 166]. This specific targeting is followed by receptor mediated endocytosis which internalizes the hyaluronic acid functionalized drug delivery carrier into the cancer cell [151]. After the receptor mediated endocytosis, hyaluronic acid undergoes degradation by hyaluronidase enzyme and produce low molecular weight components [20, 152, 161, 167].

2.6 Folate Receptor and Folic Acid

Folate receptor is a glycosylphosphatidylinositol (GPI) attached glycoprotein [168-171] with molecular weight of 38kDa [28, 29]. It shows higher level of expression on many cancer cells including colon, breast, ovarian, kidney, lung and brain [19, 21, 28, 29] compared to the normal cells and its density increases with the cancer stage. So, it is considered as a potential target for cancer diagnosis and treatment [19].

Folic acid, also known as folate, is a type of B vitamin (B9) [169, 172-174]. This small sized (441g/mol) vitamin possesses excellent properties which include biocompatibility, high stability, high availability, non-immunogenicity, non-toxicity, simple conjugation chemistry, small size and low cost [13, 175-177]. Additionally, it plays a key role in the DNA and RNA synthesis, cellular growth and survival, and metabolic processes for cells [178-180]. Folic acid exhibits high binding affinity for the folate receptors (K_d = 1nM) and serves as an attractive ligand for the development of folate receptor overexpressing cancer cell targeting drug delivery system [30, 181]. This specific targeting is followed by receptor mediated endocytosis which internalizes the folic acid functionalized drug delivery carrier into the cancer cell [26, 182].

Chapter 3: Synthesis and Characterization of Targeted Silica Nanoparticles

3.1 Motivation

In this chapter we have discussed the synthesis and characterization of dual targeted nanoparticles. Conjugation of dual targeting ligands on one nanoparticle is a surface modification process to increase cellular targeting. While single targeted nanoparticles can target only one type of cancer cell surface receptor, dual targeted nanoparticles can simultaneously target two different receptors of cancer cells and result in a combined effect in cancer cellular uptake of nanoparticles [164]. This dual targeted nanoparticle facilitates internalization of more nanoparticles into the cancer cells and consequently improves therapeutic and/or diagnostic efficacy compared to the single targeted one. However, ligand density on nanoparticle surface can influence its molecular targeting and cellular binding [183]. It was demonstrated that ligand density optimization can have a significant impact on cellular targeting [184] and it has also shown great promise in *in vivo* studies [183]. So, for ligand targeted nanoparticles, adjusting the surface ligand density is essential for enhanced ligand coverage and effective cellular targeting [22].

3.2 Materials

Tetramethyl orthosilicate (TMOS-98%), Triton X-100 and (3-Aminopropyl)trimethoxysilane (APTMS) were purchased from Acros Organics; n-hexanol (99%), fluorescamine, ethanolamine, 1-Ethyl-3-(3 dimethylaminopropyl)carbodiimide (EDC), N-Hydroxysuccinimide (NHS) and fluorescein isothiocyanate were purchased from Alfa Aesar; cyclohexane, aqueous ammonia solution (29wt% ammonia) and dimethyl sulfoxide (DMSO) were purchased from BDH Chemicals; ethanol was purchased from Decon Labs; hyaluronic Acid (8kDa) was purchased from Amazon; folic Acid (≥97%) was purchased from Enzo Life Sciences; cetrimonium bromide was purchased from Spectrum Chemicals; sodium acetate was purchased from Amresco; acetic acid was purchased from Macron Fine Chemicals; coomassie brilliant blue dye was purchased from Bio-Rad; bovine serum albumin was purchased from Sigma Aldrich. All chemicals were used without further purification. Deionized water used throughout the experiments was purified with an ELGA PURELAB Flex water purification system.

3.3 Methods

3.3.1 Synthesis of Fluorescent Silica Nanoparticles

We synthesized silica nanoparticles by water in oil microemulsion method. Initially, mixture of cyclohexane, n-hexanol, Triton X-100 and DI water was vigorously stirred at room temperature to form the microemulsion. After 15 minutes, FITC dye was added followed by the addition of TMOS and APTMS after 5 minutes. NH_4OH was added after 30 minutes of vigorous stirring. The reaction was carried on for 24 hours at room temperature. Ethanol was added to break the stability of microemulsion and recover the particles by centrifugation (14800rpm, 30mins). The particles were washed three times with ethanol and one time with water to remove the unreacted reagents.

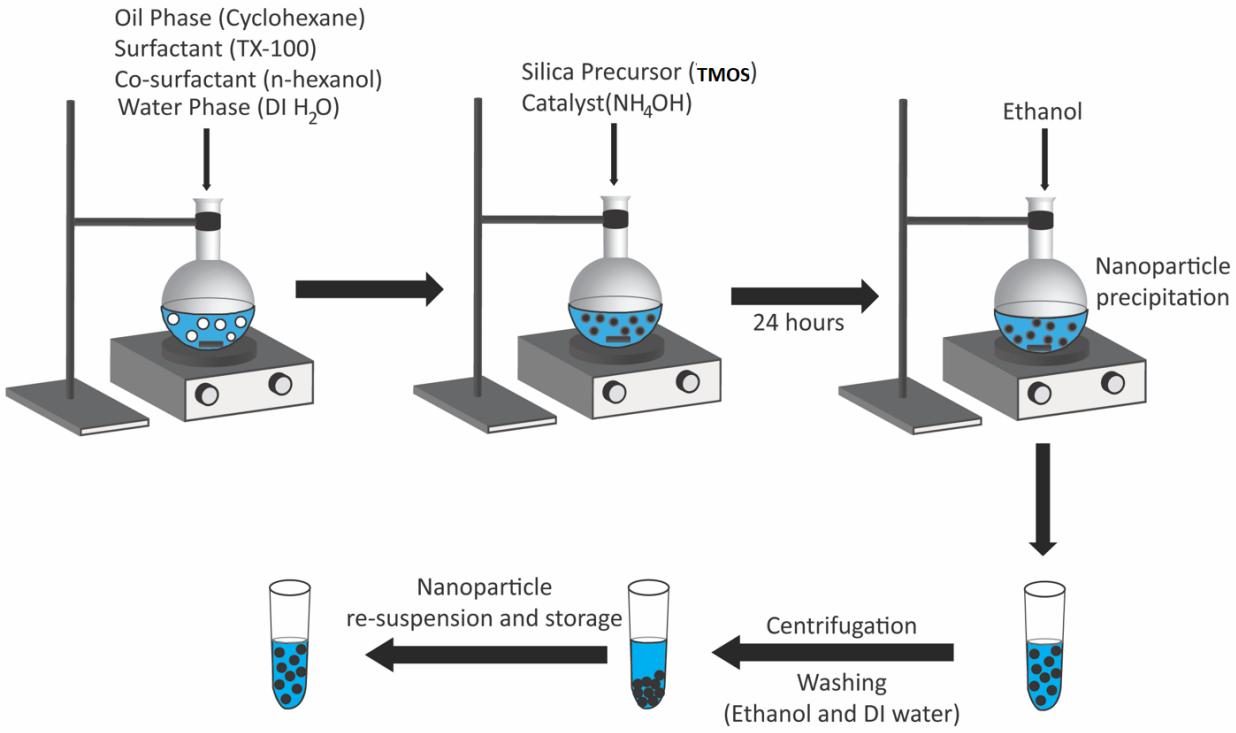

Figure 18 – Schematic representation of Silica nanoparticle synthesis by Microemulsion method

3.3.2 Synthesis of Targeted Silica Nanoparticles

We synthesized hyaluronic and folic acid conjugated dual targeted silica nanoparticles using the well-established EDC-NHS chemistry. Before conjugation of the ligands, we activated hyaluronic and folic acid to uncover free carboxylic acid group. Hyaluronic acid was activated by first dissolving it in water. EDC and NHS solutions were prepared separately in water and added to the hyaluronic acid solution. The reaction mixture was rotated overnight. Folic acid was activated by first dissolving it in DMSO. EDC and NHS solutions were prepared separately in DMSO and added to the folic acid solution. We stirred the reaction mixture overnight in dark. Following overnight activation of the ligands, hyaluronic and folic acid solutions were mixed together and stirred. Fluorescent silica nanoparticles suspended in water was added to the ligand mixture. We stirred the reaction mixture for 24 hours in dark. Following functionalization, the particles were washed two times with DMSO and two times with water to remove the unreacted reagents. The respective single targeted silica nanoparticles was synthesized following the same protocol without mixing the ligand solutions. To the best of our knowledge, this report presents the first simultaneous approach of these 2 ligands conjugation on nanoparticle surface.

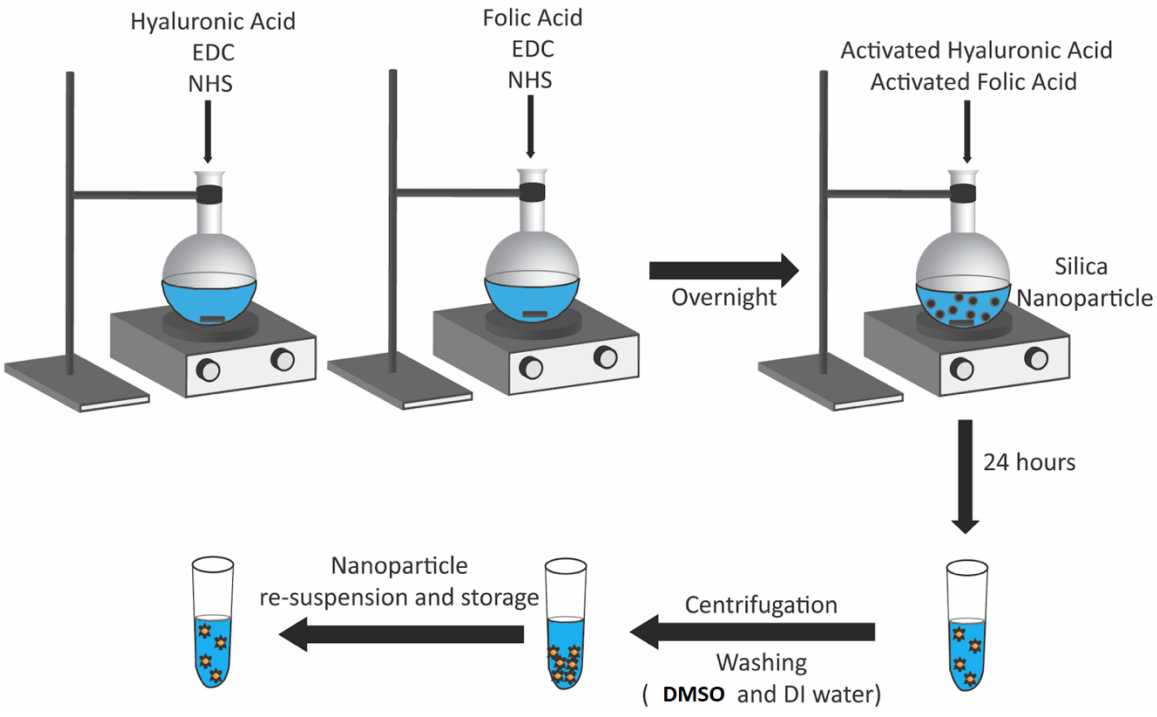

Figure 19 – Schematic representation of dual targeted silica nanoparticle synthesis

3.4 Characterization

3.4.1 Dynamic Light Scattering (DLS)

We measured the nanoparticles size and zeta potential by Dynamic light scattering (DLS) method using Malvern Zetasizer Nano ZS (Malvern, UK). The size of the nanoparticles is measured by backscatter detection at θ =173°. The zeta potential of the nanoparticles is measured using Smoluchowski model.

3.4.2 Fluorescence Microscope

We used EVOS digital inverted microscope to observe the fluorescent nanoparticles. Briefly, we took 100 µL of each nanoparticle sample in a 60x22mm micro cover glass and covered it with 22x22mm coverslip to use in the microscope.

3.4.3 Transmission Electron Microscopy (TEM)

We used a Zeiss EM 10 transmission electron microscope (TEM) operating at a voltage of 60K to characterize the morphology of the nanoparticles. TEM samples were prepared by dropping 10 µL of nanoparticle suspension on formvar-carbon film of a 300-mesh copper grid. After 15 minutes, the remaining solution was wiped away using a filter paper. The grid was then placed in a petri dish and allowed to dry overnight at room temperature.

3.4.4 Amine quantification

We measured the primary amine content of the silica nanoparticles using a quantitative fluorescamine assay. Fluorescamine (4'-phenylspiro[2-benzofuran-3,2'-furan]-1,3'-dione) reacts with primary amines to form a fluorescent pyrrolinone moieties. Briefly, 150 µL of nanoparticle suspension was taken into a 96 well plate. 50 µL of 3 mg/mL fluorescamine dissolved in DMSO was added to each well and allowed to react for 10 minutes in dark. Fluorescence of each sample were measured at 400 nm excitation and 460 nm emission with a FlexStation 3 (Molecular Devices, Sunnyvale, CA). Ethanolamine of known concentrations was used as a standard.

3.4.5 Hyaluronic Acid quantification

We measured the hyaluronic acid content of the silica nanoparticles using an indirect quantitative hexadecyltrimethylammonium bromide (CTAB) turbidimetric method. CTAB is an anionic surfactant that forms an insoluble complex with polyanionic hyaluronic acid in a solution. Formation of this complex has a linear relation with the hyaluronic acid concentration in the solution and it exhibits strong light absorption at a wavelength of 570nm. Briefly, 50µL of supernatant samples after each centrifugation was added in triplicate to a 96-well plate. The samples were incubated with 50µL of 0.2 M sodium acetate buffer (pH 5.5) at 37°C for 10 minutes. Then, 100µL of 10mM CTAB solution was added to the wells. The absorbance of the precipitated complex was read within 10 minutes against the control at 570 nm using a microplate reader. The amount of conjugated hyaluronic acid was measured by subtracting the total amount of hyaluronic acid in the supernatant solutions from the initial amount added to the reaction mixture. Hyaluronic acid of known concentrations was used as a standard.

3.4.6 Folic Acid quantification

We measured the folic acid content of the silica nanoparticles using a quantitative ultraviolet (UV) spectrophotometric method. Folic acid shows characteristic peak at 358nm wavelength. So, the absorbance of 0.2 mg/ml of each nanoparticle samples was measured at 358nm wavelength using UV spectrophotometer. Folic acid of known concentrations was used as a standard.

3.4.7 Protein adsorption

We measured the protein adsorption on targeted nanoparticles using Bradford assay with coomassie brilliant blue dye. Briefly, 0.1 mg/ml of each nanoparticle sample was incubated with 0.5 mg/ml of Bovine Serum Albumin (BSA) at 37°C and 7.4 pH. After 2 hours, the mixture was centrifuged at 12,000 rpm for 20 mins. Then 5ul of the supernatant of each nanoparticle sample was added in the 96 well plate with 250ul of the Bradford Reagent. After keeping the mixture at room temperature for 10 minutes, absorbance of each sample was measured at 595 nm. The adsorbed BSA was calculated using the equation: $q = (C_i - C_f)V/m$ where C_i and C_f are the initial and final BSA concentrations in the solution respectively; V is the BSA solution volume; m is the

mass of the nanoparticles added into the solution. BSA of known concentrations was used as a standard.

3.4.8 Fluorescence stability

We measured the fluorescence stability of the targeted nanoparticles using spectrophotometric method. Briefly, we incubated three different concentration of each nanoparticle sample in colon cancer cell culture media at 37^{o}C and 7.4 pH. After fixed time points, we measured the fluorescence of each nanoparticle sample at Ex:495nm and Em:525nm using FlexStation 3 Molecular Device fluorescence spectrophotometer. Culture media without nanoparticle was used as a control.

3.5 Results and Discussion

We have synthesized targeted nanoparticle in a two-step process. In step 1, we have synthesized fluorescently labeled amine conjugated silica nanoparticle. The amine on the nanoparticle provides reaction sites for ligand conjugation and the fluorescent nanoparticle is used for particle tracking in cells. In step 2, we have synthesized HA and FA conjugated silica nanoparticle to be used for cellular targeting.

Step 1 – Amine conjugated silica nanoparticle

In this experiment, we have synthesized 4 nanoparticles by water in oil microemulsion method. We have used water to surfactant mole ratio, R=16.08 and co-surfactant to surfactant mole ratio, P=4.82. First, we have optimized the APTMS concentration and to do this optimization we have characterized the nanoparticle without dye addition. We have varied the amine moles (moles of APTMS) with respect to silica moles (moles of APTMS+TMOS) in the synthesis reaction. We have characterized the nanoparticles by measuring their size, PDI, zeta potential, primary amine group and morphology. We ran the experiments in triplicates and presented the data as mean ± standard deviation.

3.5.1 Size

Figure 20 shows the effect of APTMS mole fraction on nanoparticle size. As can be seen from the figure, the size of the nanoparticle characterized by DLS increased from 97nm to 230nm with increasing mole fraction of APTMS. This is because higher concentration of amine group fastens the reaction rates of hydrolysis and condensation. This faster reaction rate consequently reduces nucleation period and induces particle growth which results in larger particle size [185]. Particles aggregated when excess amount of APTMS was used in the reaction. So, we used appropriate amount of APTMS in the reaction to reduce the gelation of silica nanoparticles. Particles were moderately dispersed with polydispersity index (PDI) ranging from 0.08-0.22.

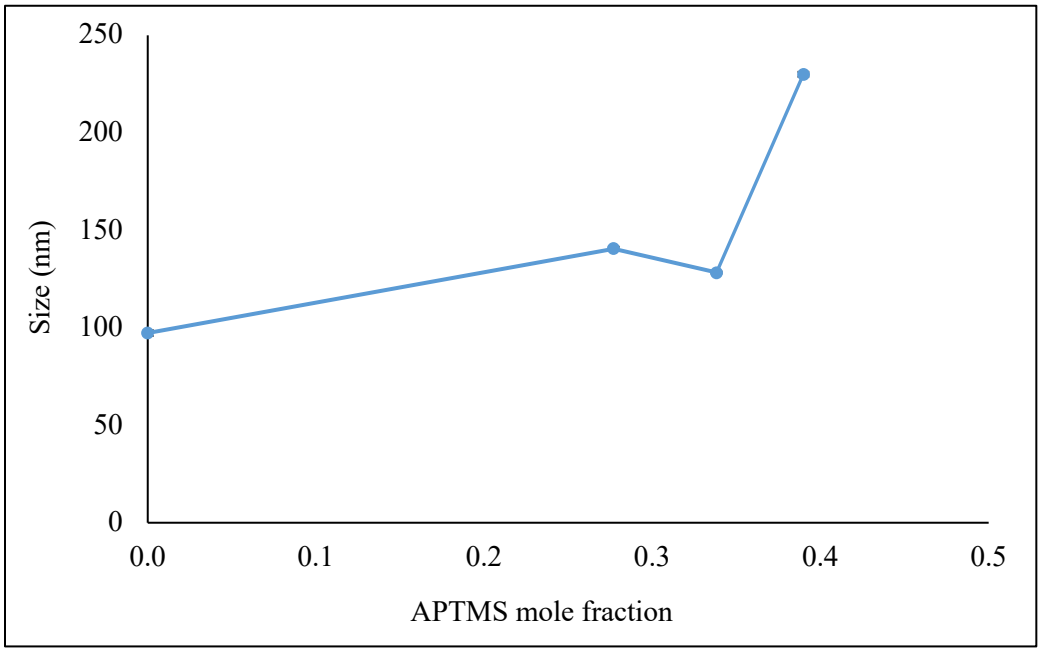

Figure 20 – Effect of APTMS mole fraction on nanoparticle size

3.5.2 Zeta potential

Figure 21 shows the effect of APTMS mole fraction on nanoparticle zeta potential. As can be seen from the figure, the control silica nanoparticles has negative zeta potential characterized by DLS because of the presence of negatively charged deprotonated hydroxyl groups on the nanoparticle surface. The zeta potential of the nanoparticles increased from -24mV to 15mV with increasing mole fraction of APTMS due to the conjugation of positively charged protonated amine groups on

the silica nanoparticle surface [186]. So, the zeta potential measurement validated the amine group conjugation on the nanoparticle surface in the tested range.

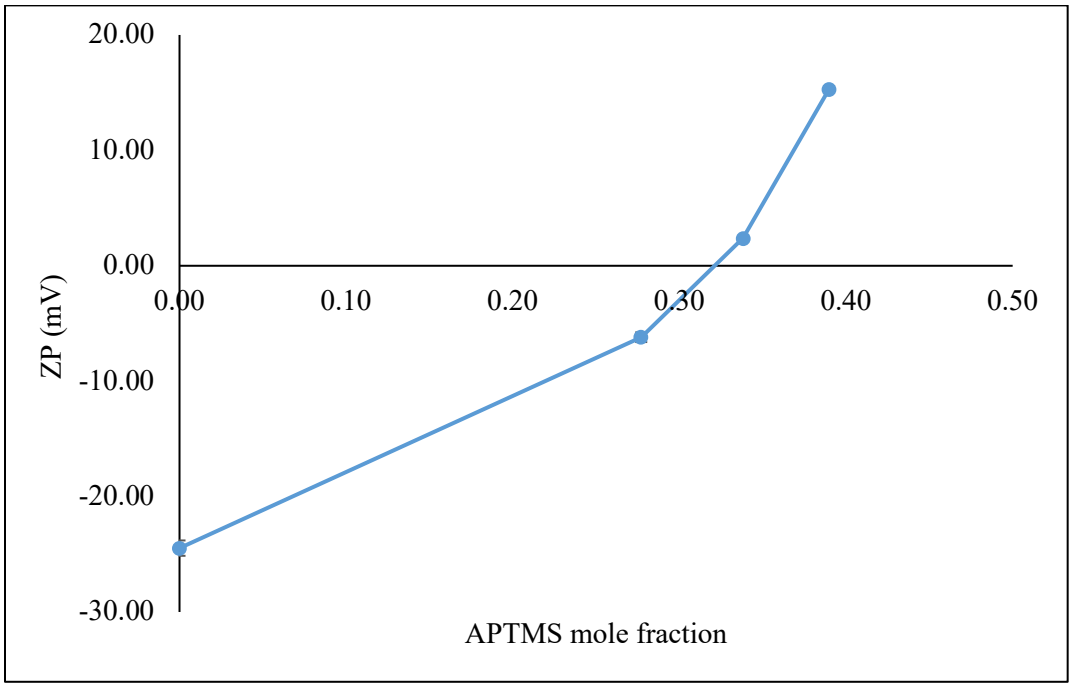

Figure 21 – Effect of APTMS mole fraction on nanoparticle zeta potential

3.5.3 Amine group quantification

Figure 22 shows the effect of APTMS mole fraction on surface amine group. As can be seen from the figure, no amine group was detected on the bare silica nanoparticle surface. However, the amine group on the nanoparticle surface increased to 0.74µmol/mg nanoparticle with further addition of APTMS in the reaction system. So, the fluorescamine assay further confirmed the presence of amine group on the silica nanoparticles surface in the tested range.

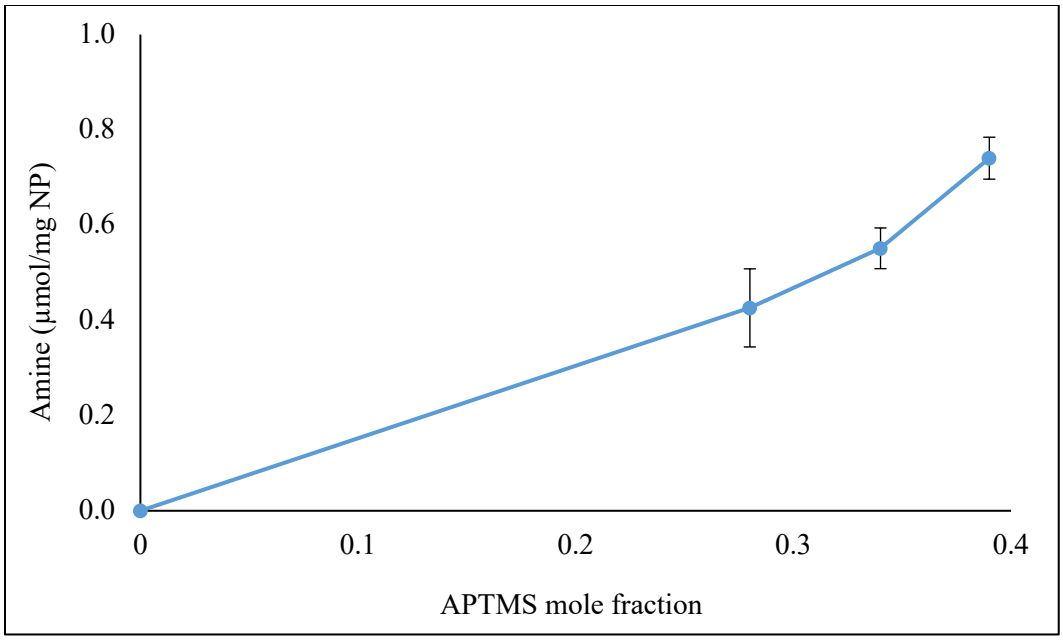

Figure 22 – Effect of APTMS mole fraction on nanoparticle surface amine group

3.5.4 Morphology

Figure 23 shows the surface morphology of amine conjugated silica nanoparticles characterized by TEM. As can be seen from the figure, nanoparticles have smooth spherical shape and monodispersity with low aggregation [185].

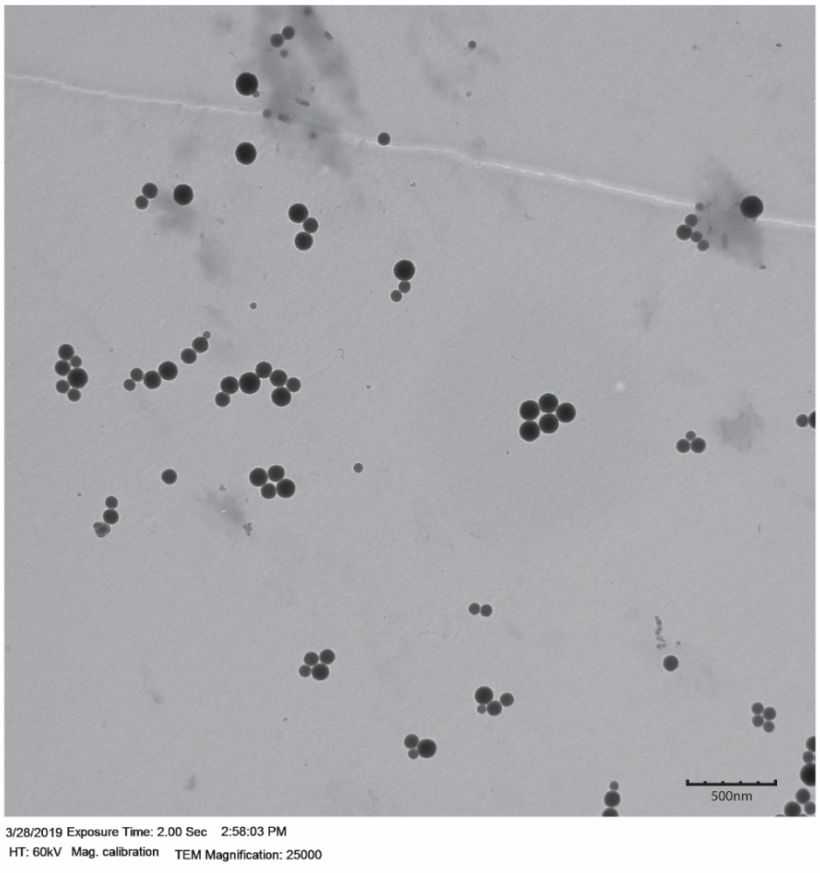

Figure 23 – Surface morphology of amine conjugated silica nanoparticle visualized with TEM (APTMS mole fraction=0.39)

Step 1 – Fluorescent silica nanoparticle

In this experiment, we have synthesized 6 nanoparticles by water in oil microemulsion method. We have used water to surfactant mole ratio, R=16.08 and co-surfactant to surfactant mole ratio, P=4.82. For optimization of dye concentration, we have used APTMS mole fraction=0.145 because beyond this point we were having issues like aggregation and fluorescence quenching. Using APTMS=0.145, we were able to produce core nanoparticle of ~100nm size with moderate dispersity. Also, it falls in our tested range where we were able to successfully conjugate amine group on nanoparticle surface. We have varied the FITC dye concentration from 0.015M to 0.082M in the synthesis reaction. We have characterized the nanoparticles by measuring their size, PDI, fluorescence and fluorescence image. We ran the experiments in triplicates and presented the data as mean ± standard deviation.

3.5.5 Size

Figure 24 shows the effect of FITC dye concentration on nanoparticle size. As can be seen from the figure, the size of the control nanoparticle characterized by DLS was 96nm. Addition of FITC in the reaction system increased the size up to 132nm indicating that FITC has been attached to the surface [187]. Particles were moderately dispersed with polydispersity index (PDI) ranging from 0.15-0.34.

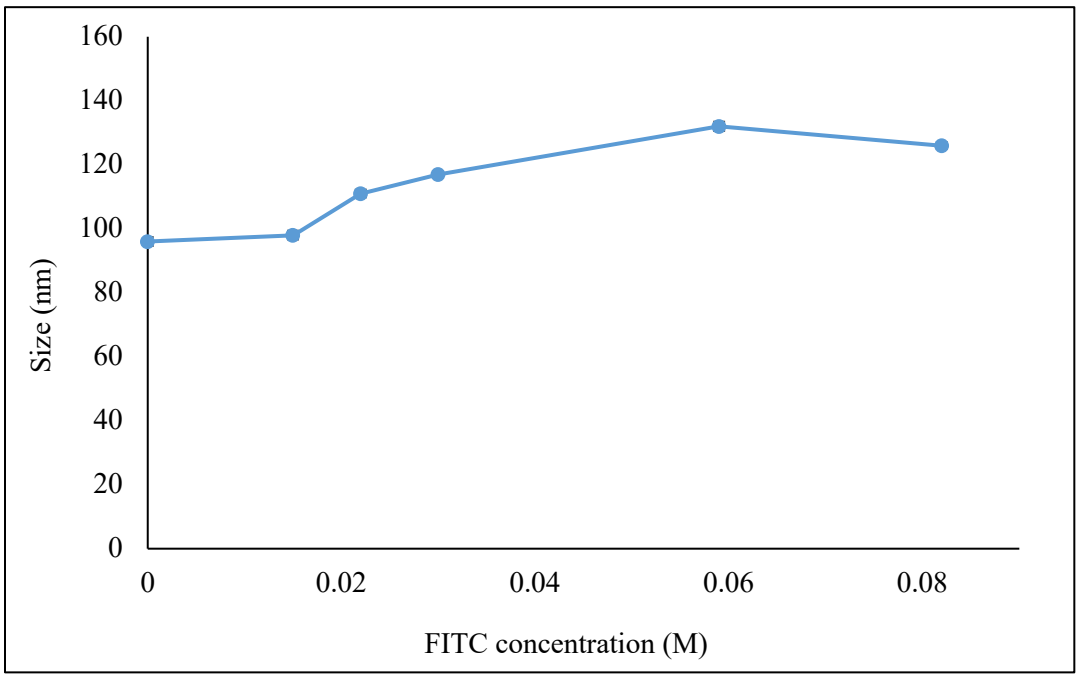

Figure 24 – Effect of FITC concentration on nanoparticle size

3.5.6 Fluorescence

Figure 25 shows the effect of FITC dye concentration on nanoparticle fluorescence. As can be seen from the figure, the particle fluorescence increased with increasing FITC concentration over a narrow range indicating more FITC molecules were incorporated into the silica nanoparticle. The isothiocyanate group of FITC covalently attaches with the amine group of APTMS and forms a stable substrate-dye complex. However, the particle fluorescence reached a plateau at higher FITC concentration suggesting the consumption of all reaction sites on APTMS [137, 188].

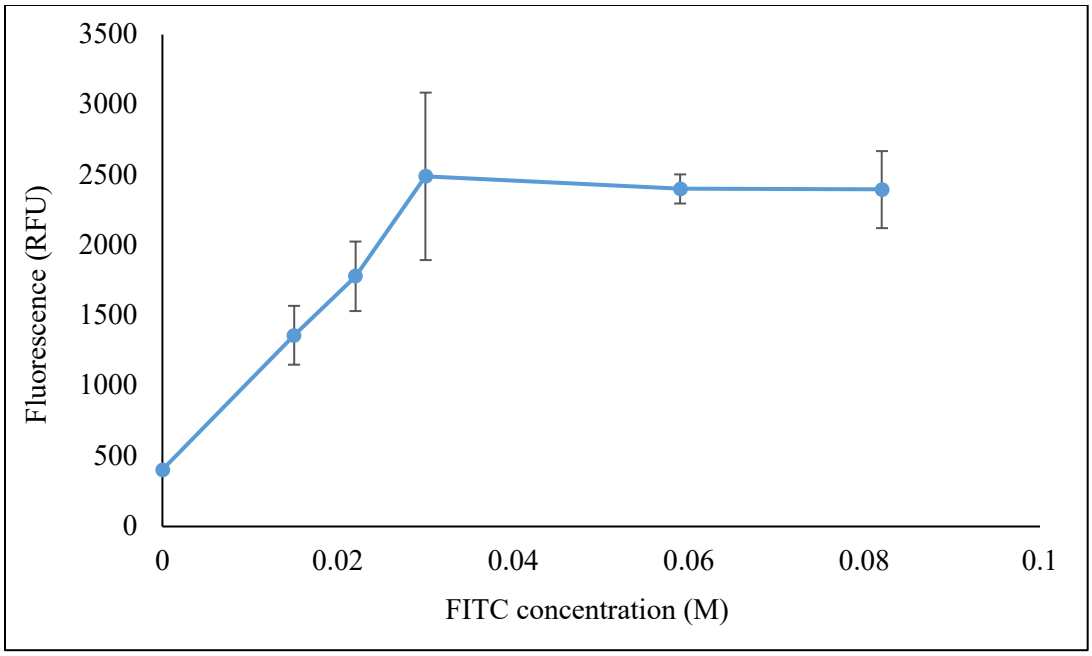

Figure 25 – Effect of FITC concentration on nanoparticle fluorescence

3.5.7 Fluorescence image

Figure 26 shows the image of fluorescent silica nanoparticles at different particle density. As can be seen from the figure, the particles showed strong green fluorescent signals originating from FITC [189].

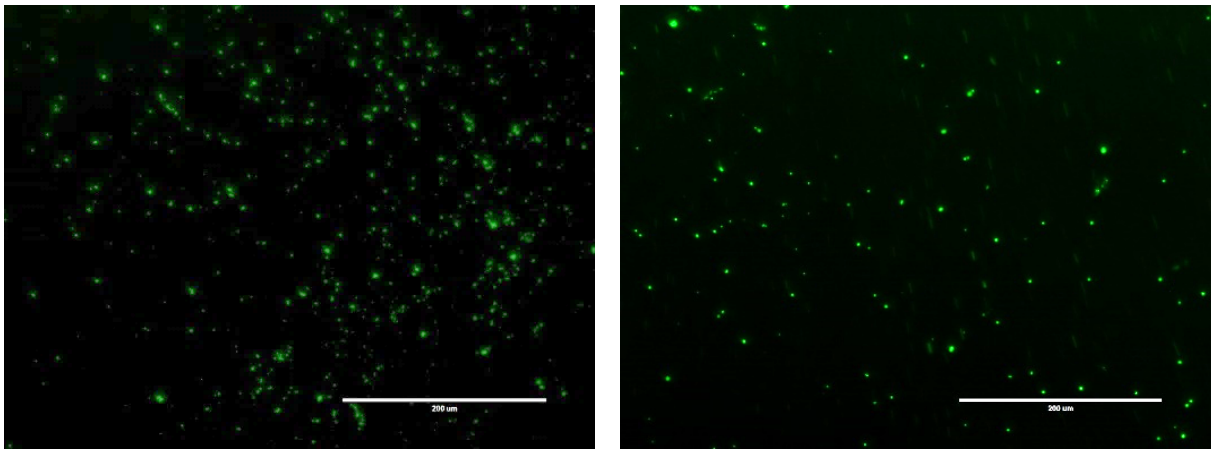

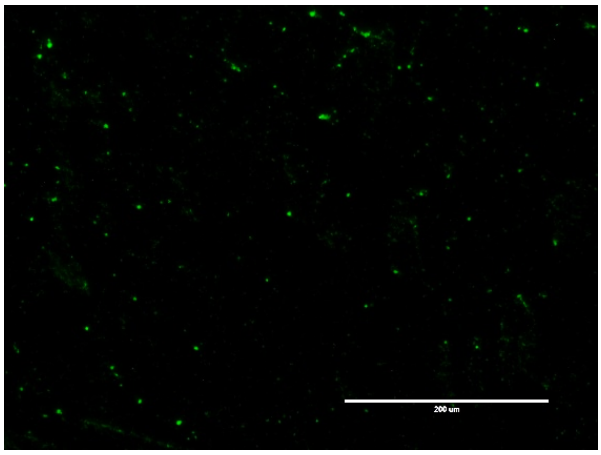

Figure 26 – Image of fluorescent silica nanoparticles visualized with Fluorescence Microscope (APTMS=0.145 and FITC=0.01M)

Step 2 – Ligand conjugated targeted silica nanoparticle

In this experiment, we have synthesized 1 non-targeted, 8 single targeted and 16 dual targeted nanoparticles by EDC-NHS method. We have used water to surfactant mole ratio, R=16.08, co-surfactant to surfactant mole ratio, P=4.82. We have used APTMS mole fraction=0.12 and FITC=0.01M because beyond this point we were having issues like aggregation and fluorescence quenching. Using APTMS mole fraction=0.12 and FITC=0.01M, we were able to produce core nanoparticle of ~100nm size with moderate dispersity. Also, it falls in our tested range where we were able to successfully conjugate amine group and dye respectively with nanoparticle. We have varied the ligand density on nanoparticle surface by varying the mole ratio of ligand to surface amine group. We have chosen 4 different mole ratios of HA to surface amine group with HA in the range of 0.5-1.25. Under each of this mole ratio, we have chosen 4 different mole ratios of FA to surface amine group with FA in the range of 3-9. We have chosen these ranges for H:A and F:A molar ratio based on ligand identification, control of size and higher nanoparticle yield. We have used EDC:HA and NHS:HA mole ratio to 50:1 and EDC:FA and NHS:FA mole ratio to 2:1 based on literature. We have characterized the nanoparticles by measuring their size, PDI, zeta potential, morphology, ligand quantification, protein adsorption and fluorescence stability. We ran the experiments in triplicates and presented the data as mean ± standard deviation. H:F:A is defined as the HA and FA molar ratio with respect to surface amine group.

3.5.8 Size

Table 1 shows the size and PDI of the targeted nanoparticles. As can be observed from the table, the nanoparticle sizes were in the range from 150-275nm. The difference in size can be due to the different orientation of ligands on nanoparticle surface. The nanoparticles were moderately dispersed with PDI in the range from 0.07-0.28.

Table 1 – Size and PDI of targeted nanoparticles

Mole			Size (nm)	PDI
Amine (A)	HA (H)	FA (F)		
1	0	0	271.57±4.46	0.23±0.02
		3	264.10±3.10	0.21±0.01
		5	261.80±3.24	0.23±0.01
		7	247.07±2.37	0.21±0.01
		9	234.93±2.49	0.20±0.01
	0.5	0	269.23±5.01	0.15±0.02
		3	156.33±3.15	0.07±0.04
		5	155.30±2.19	0.12±0.02
		7	207.93±2.64	0.22±0.01
		9	225.30±1.18	0.22±0.02
	0.75	0	155.77±4.56	0.16±0.01
		3	219.77±7.49	0.20±0.01
		5	194.97±3.46	0.16±0.01
		7	193.07±3.51	0.19±0.02
		9	252.67±6.06	0.22±0.01
	1	0	198.83±5.03	0.13±0.01
		3	147.37±2.46	0.28±0.02
		5	239.27±1.44	0.24±0.01
		7	195.90±1.31	0.17±0.04
		9	250.93±2.29	0.23±0.03
	1.25	0	211.43±4.90	0.12±0.02
		3	231.13±3.10	0.24±0.02
		5	164.63±1.95	0.21±0.02
		7	181.60±2.95	0.16±0.03
		9	193.63±2.45	0.19±0.01

3.5.9 Zeta potential

Figure 27 shows the zeta potential of the targeted nanoparticles. The average zeta potential of the non-targeted nanoparticle was -15mV due to the presence of negatively charged deprotonated

silanol groups on the nanoparticle surface [190]. The zeta potential of the nanoparticles shifted towards the positive direction following the modification with only folic acid (marked by orange line) due to the presence of protonated amino acid groups of folate [19]. The zeta potential of the nanoparticles reversed to the negative direction following the addition of hyaluronic acid in the reaction system due to the presence of negatively charged deprotonated carboxyl group on the nanoparticle surface [161]. So, measurement of zeta potential confirmed the successful linkage of HA and FA to the nanoparticle surface.

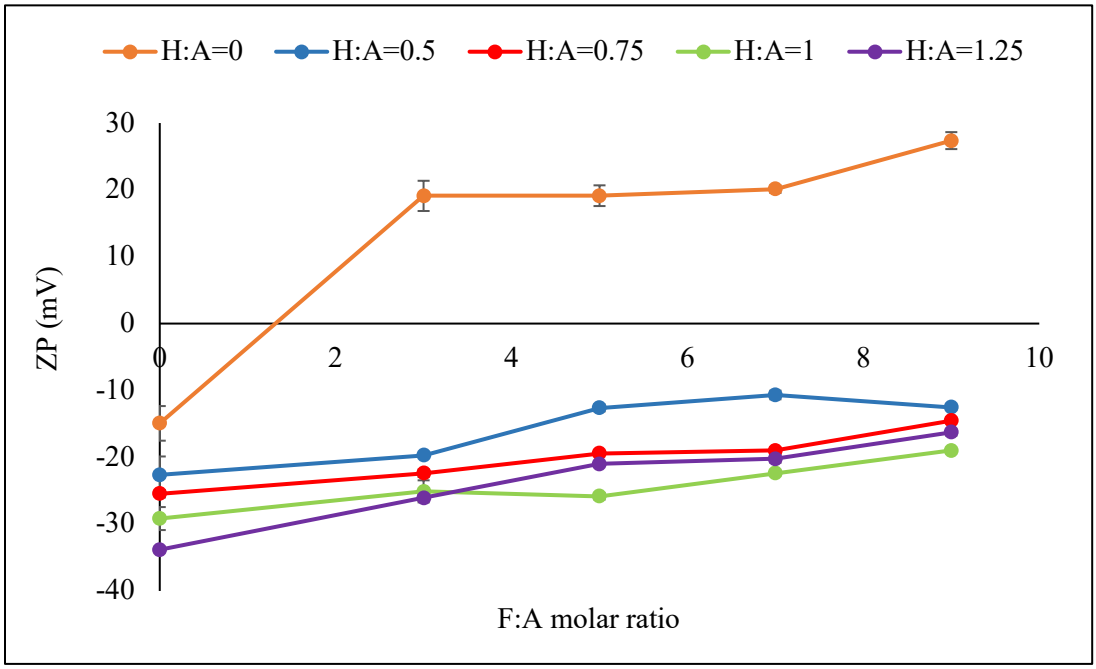

Figure 27 – Effect of ligand conjugation on nanoparticle zeta potential

3.5.10 HA quantification

Figure 28 shows the HA conjugation on the targeted nanoparticles measured by CTAB turbidimetric method. As can be seen from the figure, at higher F:A molar ratios i.e. ≥7, increase in H:A molar ratio from 0.5 to 1.25 didn't significantly change the nanoparticle surface coverage by HA. However, at lower F:A molar ratios i.e. ≤ 5, increase in H:A molar ratio from 0.5 to 1.25 significantly increased HA conjugation on nanoparticle surface. With increasing F:A molar ratio from 0 to 9, less HA were conjugated on the nanoparticle surface which probably could be due to the lack of availability of reaction sites.

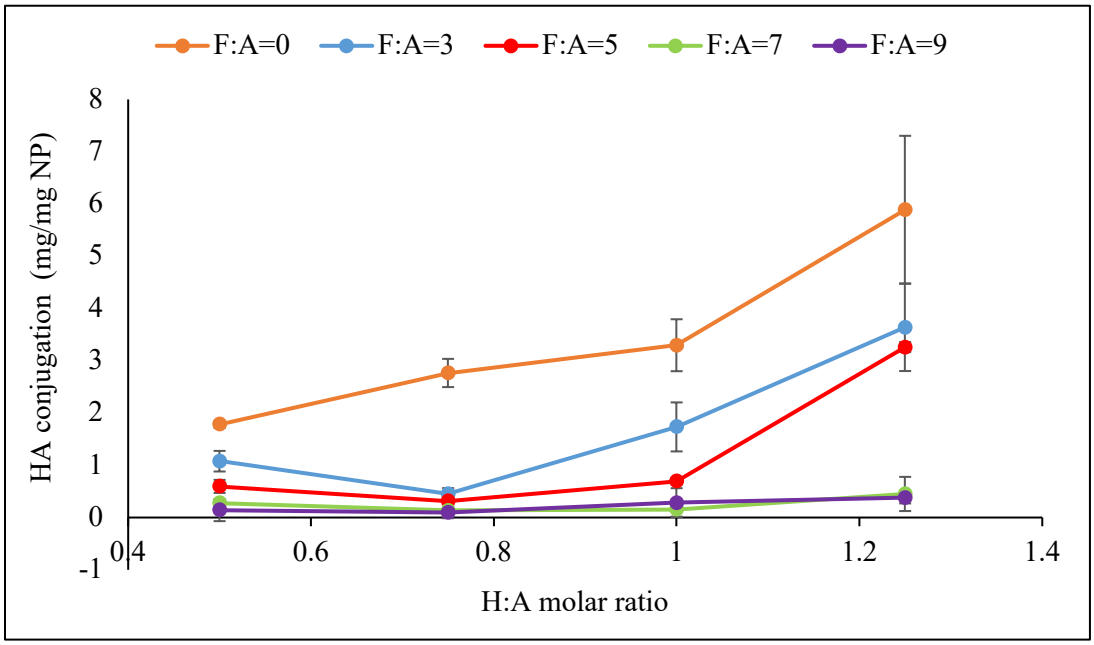

Figure 28 – Effect of H:A molar ratio on nanoparticle surface conjugation by HA

3.5.11 FA quantification

Figure 29 shows the FA conjugation on the targeted nanoparticles measured by spectrophotometric method. As can be seen from the figure, at higher H:A molar ratios i.e. ≥0.75, increase in F:A molar ratio from 3 to 7 didn't significantly change the nanoparticle surface coverage by FA. However, further increase in F:A molar ratio to 9 significantly improved the surface coverage. At lower H:A molar ratio i.e. ≤0.5, increase in F:A molar ratio from 0 to 9 significantly increased FA conjugation on nanoparticle surface. At F:A=9, less FA were conjugated on the nanoparticle surface with increasing H:A molar ratio from 0 to 1.25, which probably could be due to the lack of availability of reaction sites.

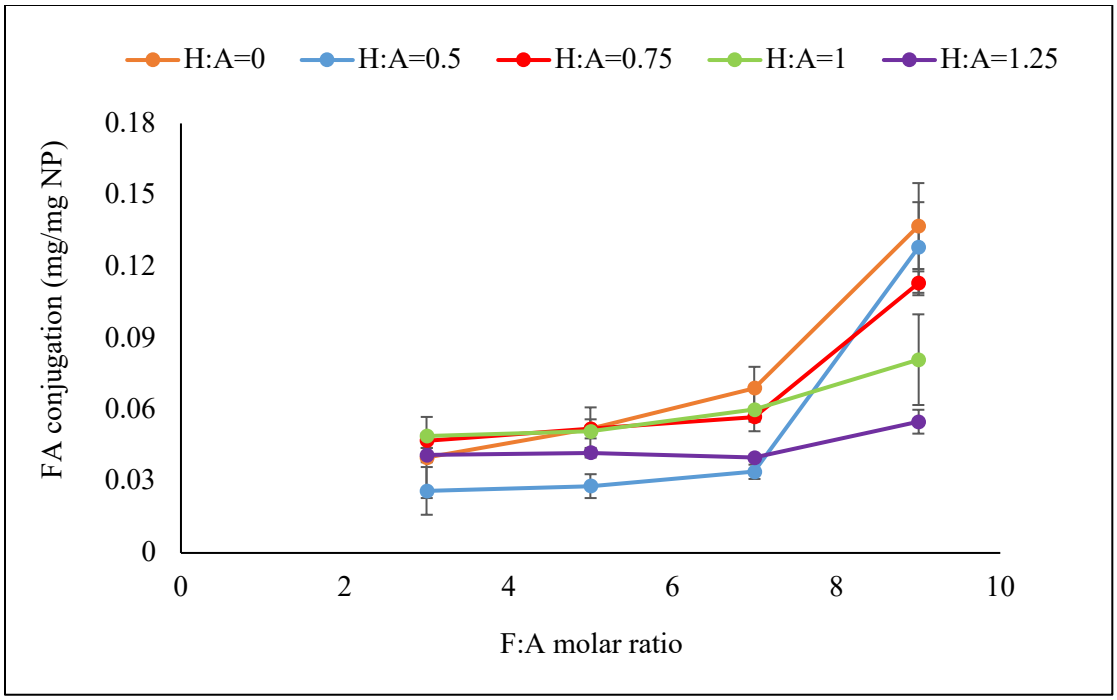

Figure 29 – Effect of F:A molar ratio on nanoparticle surface conjugation by FA

3.5.12 Protein adsorption

The interactions between the nanoparticles and the proteins affect the biological fate of the nanoparticles. When nanoparticles enter the blood circulation upon intravenous administration, protein corona is formed over them which creates a new 'biological identity' of the nanoparticles [42]. This new 'biological identity' of the nanoparticles influences their biodistribution and clearance [54], thereby altering their destination in the body [66]. So, it is required to have a balance between targeted cellular uptake and protection from protein corona. Figure 30 shows the BSA protein adsorption on the targeted nanoparticles measured by spectrophotometric method. As can be seen from the figure, there was no significant change in protein adsorption on nanoparticle surface with an increase in F:A molar ratio from 0 to 9. It indicated that FA conjugation had negligible impact on protein adsorption. However, with an increase in H:A molar ratio from 0 to 1.25, BSA protein adsorption was substantially reduced on the nanoparticle surface which could be due to the zeta potential and hydrophilicity of the HA conjugated nanoparticles. From figure 26 we have observed that, the zeta potential of the nanoparticles were negative following the conjugation of HA on nanoparticle surface. This negative charge could result in an electrostatic

repulsion with BSA protein of negative charge and eventually reduce protein adsorption [191]. Also, addition of HA could form a hydrophilic shell on nanoparticle surface and repel plasma protein from adsorption [26]. So, modification of nanoparticle surface with ligand reduces protein adsorption which will increase targeted cellular internalization by avoiding non-specific uptake.

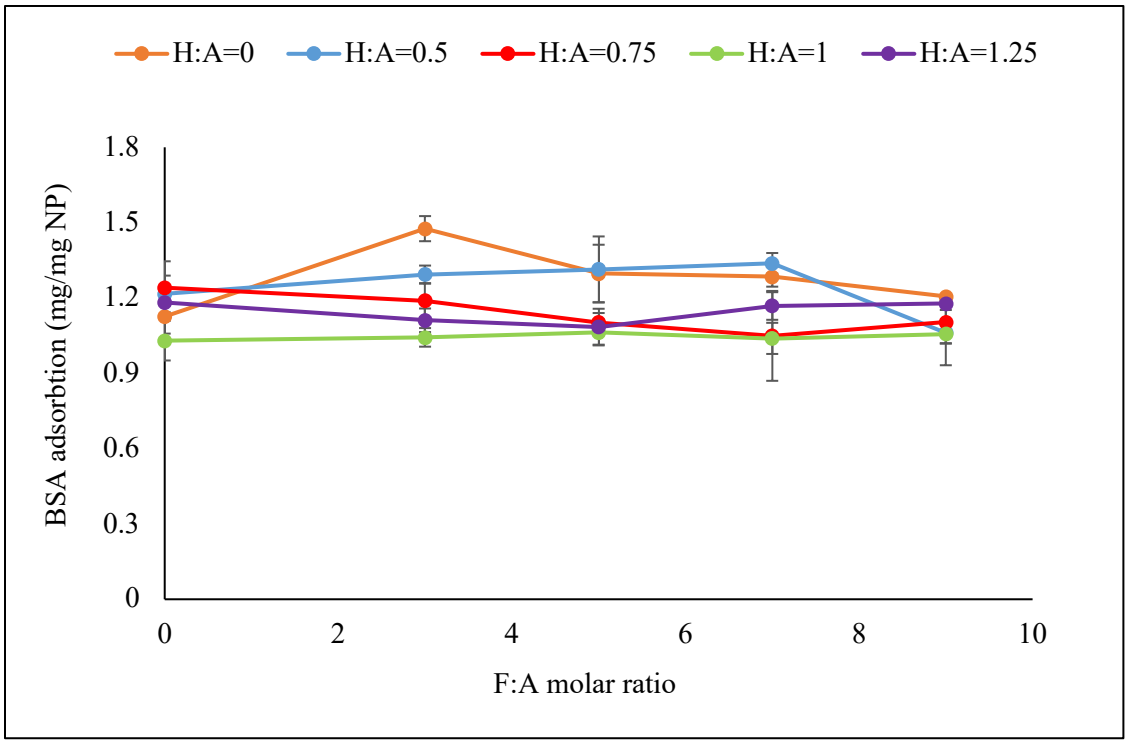

Figure 30 – BSA protein adsorption on targeted nanoparticles

3.5.13 Fluorescence stability

We have used FITC dye in our nanoparticle for cellular targeting which has some major drawbacks such as self-quenching, photobleaching and loss of fluorescence after conjugation. So, we have characterized our targeted nanoparticles for their fluorescence stability. Figure 31 shows the fluorescence stability of the targeted nanoparticles (H:F:A=1.25:9:1) measured by fluorescence spectrophotometer. As can be seen from the figure, the fluorescence of the targeted nanoparticle in three different concentration is maintained in the cell culture media for more than 24 hours without significant variation. Higher nanoparticle concentration exhibited higher fluorescence compared to the lower concentrations due to higher dye conjugation. This excellent stability can

be attributed to the covalent bond between primary amino groups of silica nanoparticles and isothiocyanate group of FITC which forms relatively stable substrate-dye complex [137]. These results suggested that the dye doped dual targeted nanoparticles can be used in the cellular targeting study without loss of fluorescence in the tested time range.

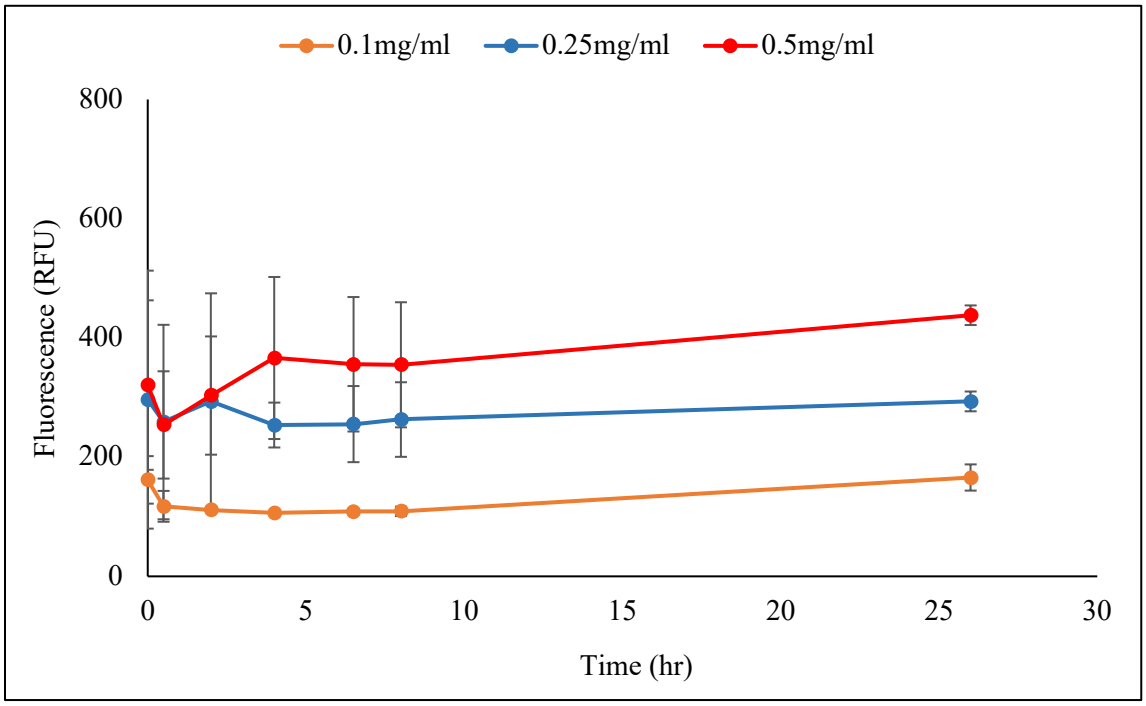

Figure 31 – Fluorescence stability of targeted nanoparticles (H:F:A=1.25:9:1)

3.6 Summary

In this chapter, we have demonstrated a novel approach for the synthesis of HA and FA conjugated nanoparticles from fluorescently tagged amine conjugated silica nanoparticles. We have discussed various characterization techniques of the nanoparticles. The zeta potential measurement and fluorescamine assay confirmed the amine group conjugation on the silica nanoparticle surface. The fluorescence measurement and images confirmed the successful conjugation of FITC dye with silica nanoparticle. The CTAB turbidimetric method and spectrophotometric method confirmed the successful conjugation of HA and FA respectively on silica nanoparticle surface. Finally, the targeted nanoparticles showed moderate size distribution, reduced protein adsorption and excellent fluorescence stability which are useful for cellular targeting.

Chapter 4: Cytotoxicity of Targeted Silica Nanoparticles

4.1 Motivation

Nanoparticle toxicity on cells has been an increasingly important issue over the past decades due to the rapid growth of their use in different biomedical applications. Non-toxic materials are most often used to synthesize nanoparticles but they possess many different physiochemical properties [192]. These properties make them convenient for theranostic application but also produces toxicity [193]. So, it is important to evaluate the nanoparticle cytotoxicity which helps to understand the action mechanisms of chemicals on cells and tissues. The key mechanism of nanoparticle toxicity is oxidative stress which is the imbalance between Reactive Oxygen Species (ROS) formation and the potential of the biological system to detoxify ROS. Nanoparticles increase ROS formation by physicochemical interaction with cell membrane that causes damage to cell membrane, proteins and DNA [194].

Researchers have begun conducting many *in vitro* cytotoxicity studies due to immense interest in nanoparticle toxicity. In the past years, various methods have been developed to study the cell viability and cell culture proliferation. The most convenient method has been optimized for the use of 96-well microplates which allows rapid and simultaneous analysis of many samples. *In vitro* cytotoxicity testing has many advantages. Elimination of the need of animal use and ability to determine cell or organ specific toxicity are few of those. Compared to animal studies, *in vitro* cytotoxicity testing is easier to control and reproduce, and is less expensive [195]. *In vitro* cytotoxicity testing can be useful in evaluating the biocompatibility of new particles at the early stages of development. Using *in vitro* cytotoxicity testing early in a project saves time, money and animals [196]. However, in the case of cytotoxicity assays, it is important to know that cell cultures are responsive to changes in their environment such as temperature and pH. Therefore, control of experimental conditions is an important factor to make sure that the toxicity has been caused by the tested nanoparticles but not the fluctuating culturing conditions [195].

We conducted a colorimetric MTT assay as a form of cytotoxicity study to confirm the biocompatibility of the targeted nanoparticles. The goal of the MTT assay is to provide an idea about the metabolic activity of the cells. MTT (3-[4, 5-dimethylthiazol-2-yl]-2, 5-diphenyltetrazolium bromide) is a yellow colored water soluble tetrazolium salt. It gets converted

into a blue colored insoluble formazan crystals with the cleavage of the tetrazolium ring by succinate dehydrogenase within the mitochondria. When cells die, they lose the ability to convert MTT into formazan i.e. MTT is converted only by metabolically active cells. So, color formation serves as a useful marker only for viable cells with active metabolism.

4.2 Materials

Tetramethyl orthosilicate (TMOS-98%), Triton X-100 and (3-Aminopropyl)trimethoxysilane (APTMS) were purchased from Acros Organics; n-hexanol (99%), fluorescamine, ethanolamine, 1-Ethyl-3-(3 dimethylaminopropyl)carbodiimide (EDC), N-Hydroxysuccinimide (NHS) and fluorescein isothiocyanate were purchased from Alfa Aesar; cyclohexane, aqueous ammonia solution (29wt% ammonia) and dimethyl sulfoxide (DMSO) were purchased from BDH Chemicals; ethanol was purchased from Decon Labs; hyaluronic Acid (8kDa) was purchased from Amazon; folic Acid (≥97%) was purchased from Enzo Life Sciences; cetrimonium bromide was purchased from Spectrum Chemicals; thiazoyl blue tetrazolium bromide (MTT), sodium acetate was purchased from Amresco; acetic acid was purchased from Macron Fine Chemicals; coomassie brilliant blue dye was purchased from Bio-Rad; bovine serum albumin was purchased from Sigma Aldrich. All chemicals were used without further purification. Deionized water used throughout the experiments was purified with an ELGA PURELAB Flex water purification system.

Cells were purchased from American Type Culture Collection (ATCC). Chinese Hamster Ovary (CHO) cells were maintained in Ham's F-12K nutrient mixture with L-glutamine (Corning cellgro, Manassas, VA), supplemented with 10% fetal bovine serum (VWR Life Science Seradigm) and 1% penicillin/streptomycin (Corning cellgro). Human Colon Adenocarcinoma (HCT116) cells were maintained in Dulbecco's Modified Eagles Medium (DMEM)/High Glucose (HyClone, GE Healthcare Life Sciences), supplemented with 10% FBS and 1% antibiotics. Both cell lines were incubated at 37°C in 5% CO_2.

4.3 Methods

20,000cells/well were seeded in a 96 well plate and incubated overnight at 37ºC. After incubation, the culture media was renewed with culture media containing different concentration of nanoparticles. Four hours before the time point of, 2 mg/ml of MTT was added to each well. After

4 hours, the culture media of each well was aspirated completely without touching the blue-purple crystals of insoluble formazan. DMSO was added to each well to dissolve the crystals. The well plate was vortexed for 5 minutes at around 500 rpm with the plate agitator until crystals have completely dissolved. Absorbance was measured at 540 nm wavelength using a spectrophotometer. Cells without nanoparticle treatment was used as control. The cell viability of each nanoparticle sample was measured using the equation,

%Viability = (Absorbance of cells with nanoparticles / Absorbance of control cells) x 100%

4.4 Results and Discussion

Cytotoxicity of targeted nanoparticles was evaluated after 24, 48 and 72 hours of nanoparticle exposure at doses range of 0.1-100 μg/ml on HCT116 and CHO cells. CHO cell is a commonly used cell line for cytotoxicity studies and HCT116 was selected to be used as a colon cancer cell model for toxicity studies. We selected the silica nanoparticle exposure time and dosage range based on literature because dosage level and exposure time below our selected range did not produce significant toxicity in mammalian cells [197-199]. We ran the experiments in triplicates and presented the data as mean ± standard deviation. H:F:A is defined as the HA and FA molar ratio with respect to surface amine group.

4.4.1 Exposure concentration

Nanoparticle concentration is a significant factor that affects toxicity. Figure 32A shows the effect of targeted nanoparticle concentration on colon cancer (HCT116) cell viability after 48 hours of nanoparticle exposure. As can be seen from the figure, cell viability of all the nanoparticle formulations depended on nanoparticle exposure concentration. The nanoparticles showed higher cell viability at 0.1 μg/ml of concentration. Cell viability reduced gradually with increasing concentration. One possible explanation based on literature is that, the number of nanoparticles interacted with the cells increased gradually with increasing exposure concentration which may have generated more ROS and subsequently reduced cell viability [200, 201]. At the highest tested concentration i.e. 100 μg/ml, all the nanoparticles exhibited ≥80% cell viability. We observed similar trends at other tested time point shown in Figure 32B.

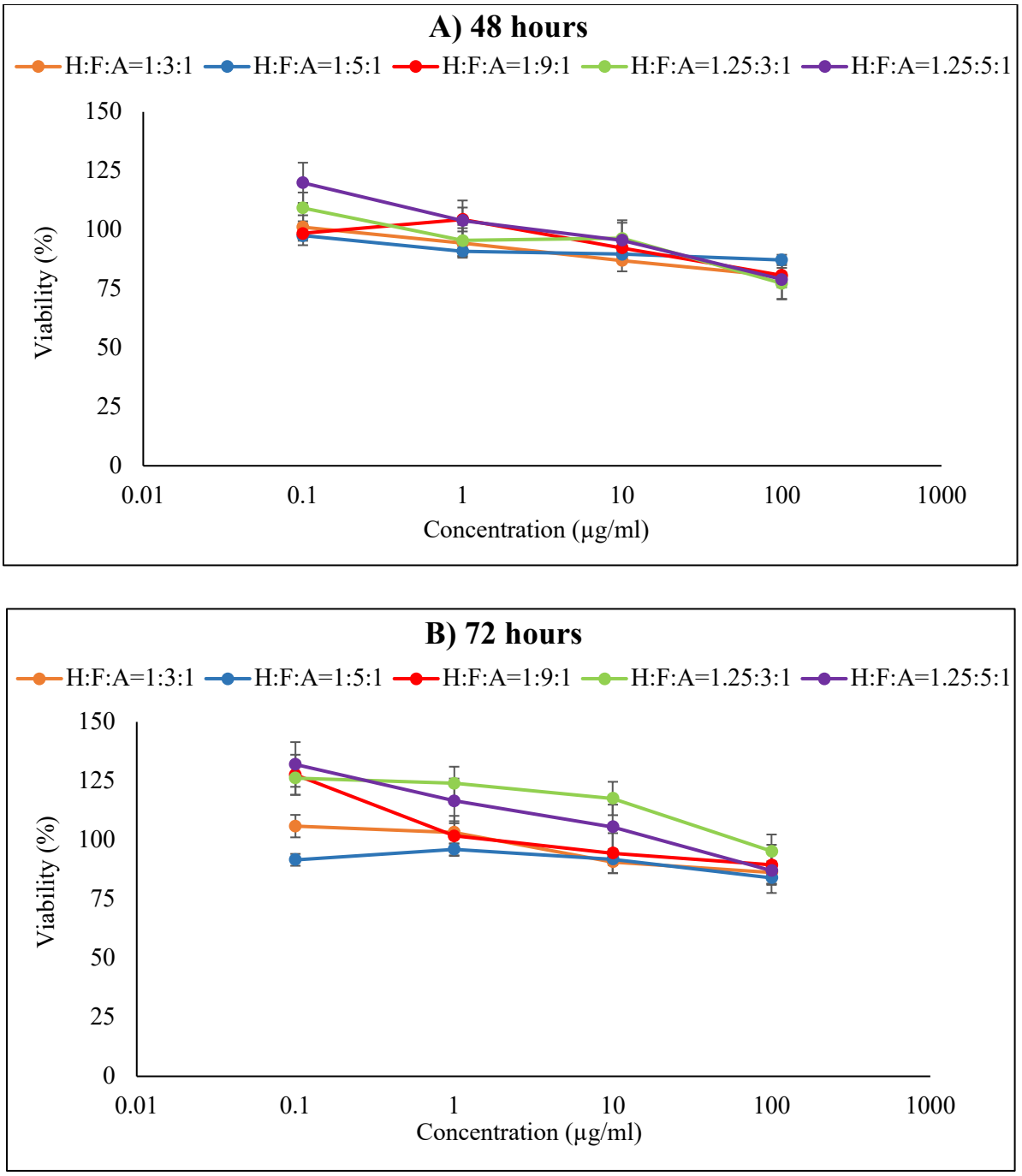

Figure 32 – Concentration dependent cytotoxicity study of targeted silica nanoparticle on HCT116 cell after A) 48 hours and B) 72 hours

4.4.2 Exposure time

Nanoparticle cytotoxicity is also impacted by exposure time. Figure 33A shows the effect of exposure time of targeted nanoparticle on colon cancer (HCT116) cell viability at 0.1 µg/ml of nanoparticle concentration. As can be seen from the figure, cell viability of all the nanoparticle formulations performed in an exposure time dependent manner. The nanoparticles showed higher cell viability at 24 hours. Cell viability reduced gradually with increasing exposure time. One possible explanation based on literature is that, the number of nanoparticles interacted with the cells increased gradually with increasing exposure time which may have generated more ROS and subsequently reduced cell viability [200, 201]. At the longest tested exposure time i.e. 72 hours, nanoparticles exhibited ≥80% cell viability. We observed similar trends at other tested time point shown in Figure 33B and C.

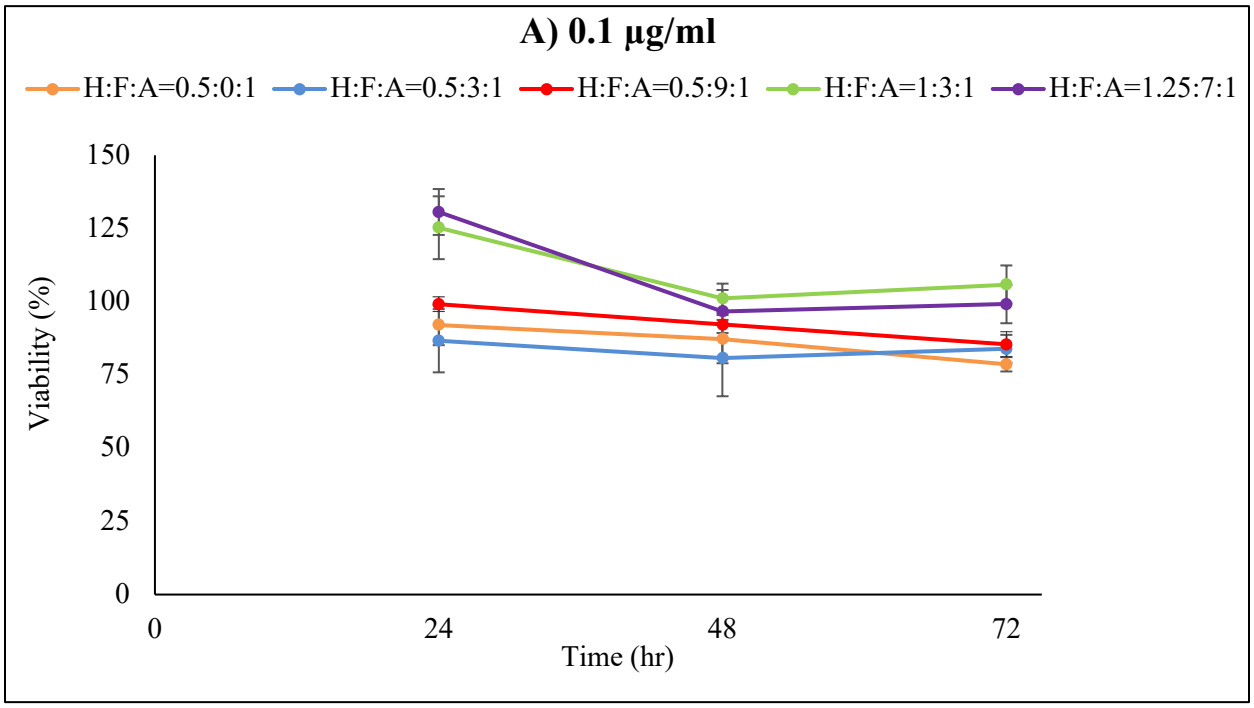

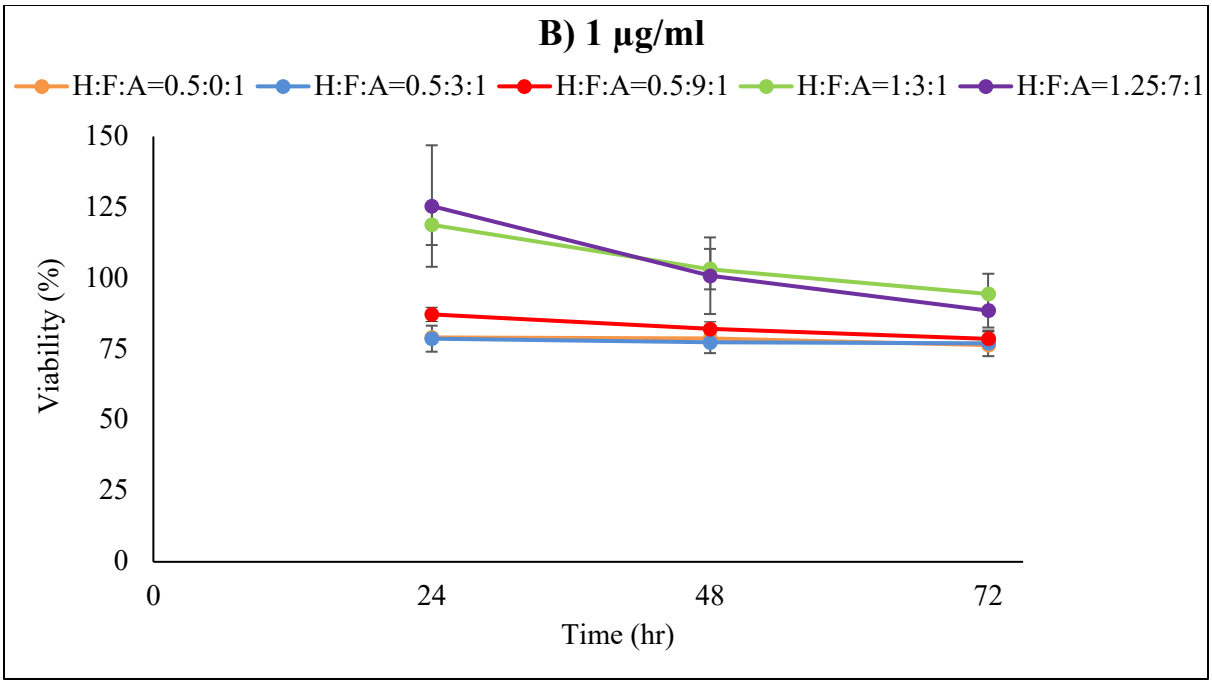

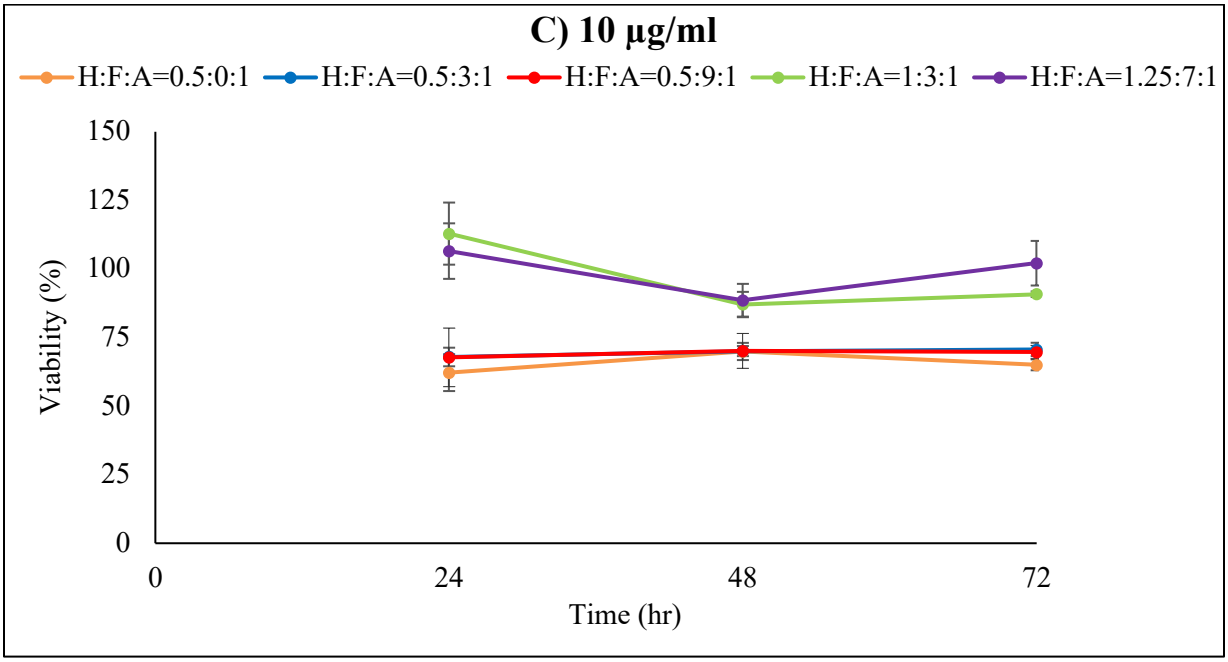

Figure 33 – Time dependent cytotoxicity study of targeted silica nanoparticle on HCT116 cell at A) 0.1 µg/ml, B) 1 µg/ml and C) 10 µg/ml

4.4.3 Cell type

Nanoparticle cytotoxicity varies from cell to cell which depends on cell physiology, proliferation rate and membrane characteristics [202]. Figure 34 shows the cell viability profiles of CHO and HCT116 cells at different nanoparticle concentrations for different time points. As can be seen from the figures, cell viability depends on cell type. We did not observe any effect of nanoparticle exposure time and concentration on CHO cell viability. All the nanoparticles showed ≥90% CHO cell viability at the tested concentrations and time points. On the other hand, HCT116 colon cancer cell showed exposure time and concentration dependent viability i.e. the cell viability reduced with exposure time and concentration. All the nanoparticles showed ≥70% HCT116 cell viability at the tested concentrations and time points. This can be explained by the difference in interaction between nanoparticles and different types of cells. The higher cell viability of CHO cells is due to the lower uptake of nanoparticles. Cancer cells on the other hand uptake more nanoparticles compared to normal cells because of the overexpression of biomarkers specific to some ligands conjugated on the nanoparticles (active targeting). All these make more nanoparticles to interact with cancer cells and cause cellular damage. So, nanoparticles are more toxic to cancer cell compared to normal cells [203].

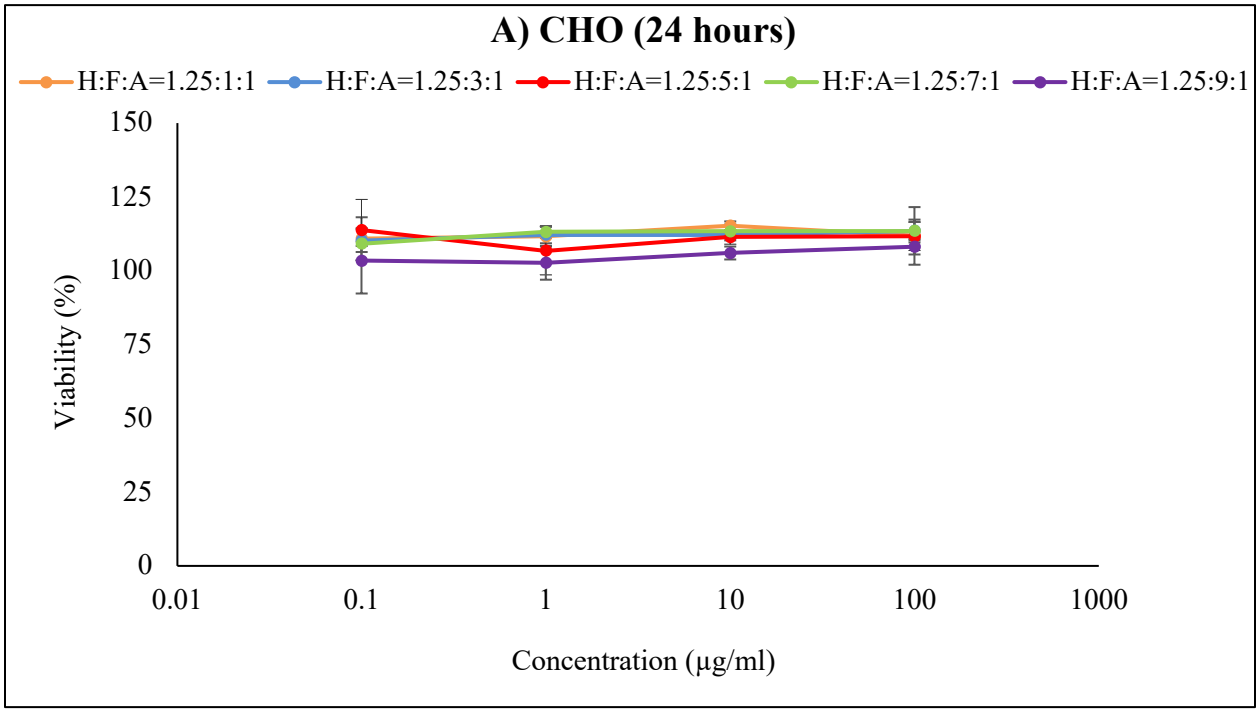

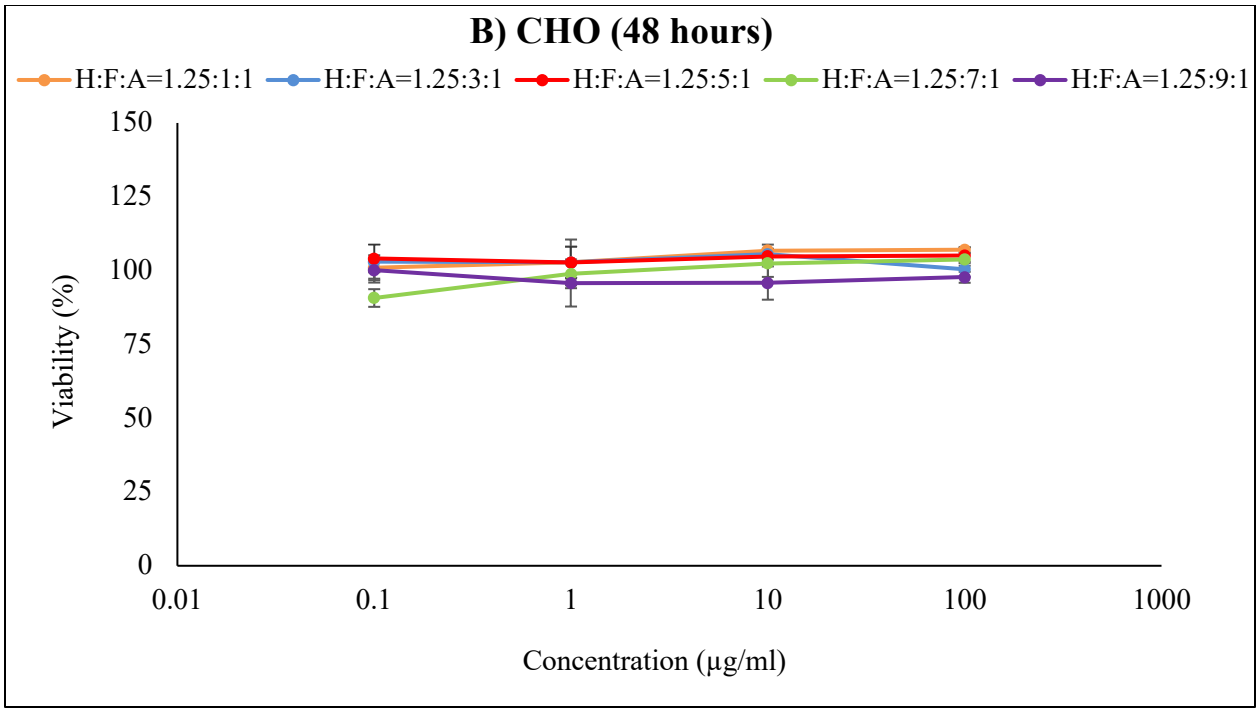
B) CHO (48 hours)
H:F:A=1.25:1:1
H:F:A=1.25:3:1
H:F:A=1.25:5:1
H:F:A=1.25:7:1
H:F:A=1.25:9:1
Viability (%)
150
125
100
75
50
25
0
0.01
0.1
1
10
100
1000
Concentration (µg/ml)

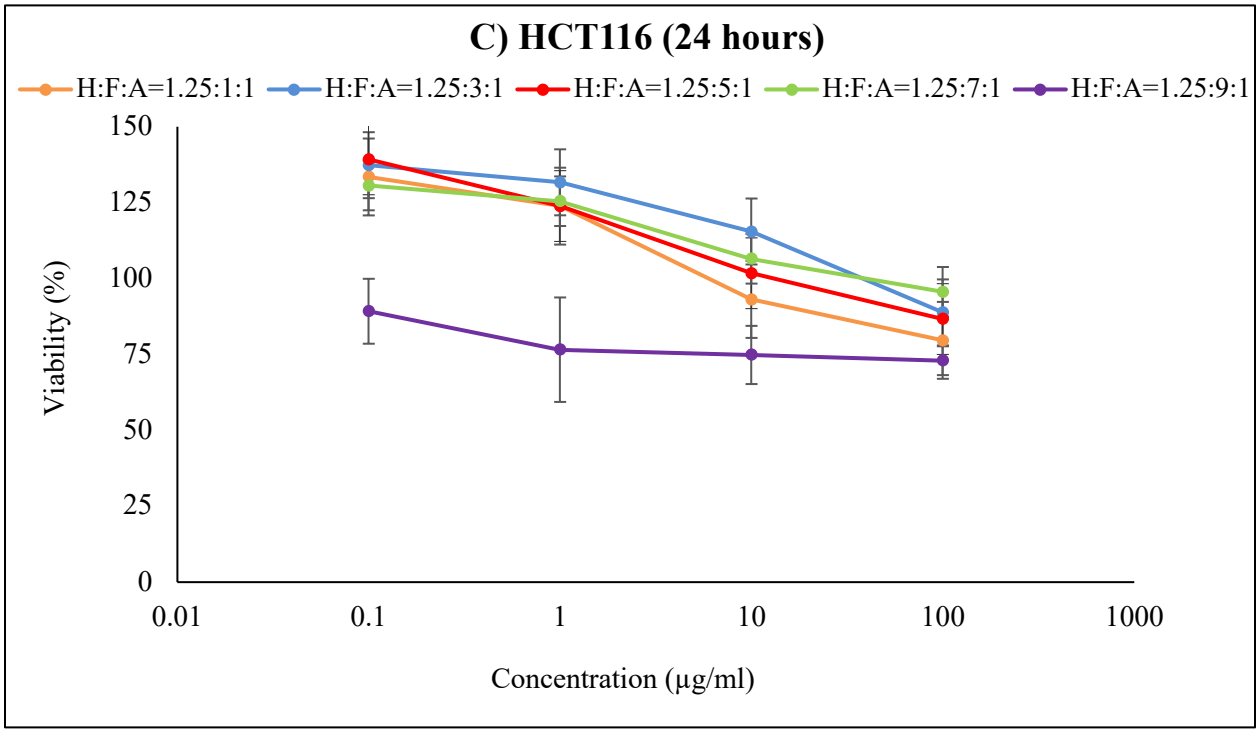
C) HCT116 (24 hours)
H:F:A=1.25:1:1
H:F:A=1.25:3:1
H:F:A=1.25:5:1
H:F:A=1.25:7:1
H:F:A=1.25:9:1
Viability (%)
150
125
100
75
50
25
0
0.01
0.1
1
10
100
1000
Concentration (µg/ml)

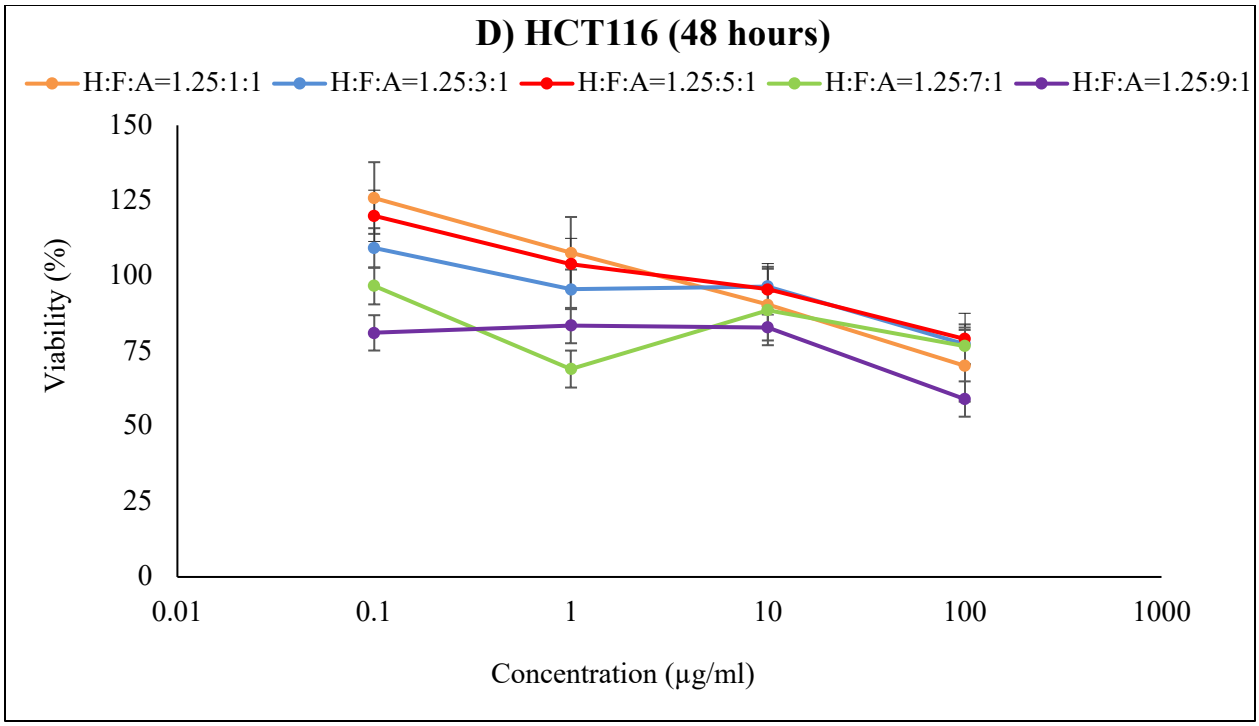

Figure 34 – Cell type dependent cytotoxicity study of targeted silica nanoparticle on A) CHO (24 hours), B) CHO (48 hours), C) HCT116 (24 hours) and D) HCT116 (48 hours)

4.4.4 Nanoparticle size

Nanoparticles possess many physicochemical properties which can impact its cytotoxicity. Figure 35 shows the cell viability profiles of 3 different sizes of dual targeted nanoparticles. HCT116 cells were treated with nanoparticle doses of 0.1-100 µg/ml for 72 hours. It has been observed that the smallest nanoparticle showed lowest cell viability and the largest nanoparticle showed highest cell viability within the tested concentration range. This trend can be related to nanoparticle size. When nanoparticle size decreases, surface area to volume ratio increases. This results in a greater number of molecules exposed on the particle surface leading to more interactions with cellular membrane. The greater surface area to volume ratio also increases ROS production. Therefore, the smaller the nanoparticle size, the higher the surface reactivity which is more toxic to biological systems. Moreover, it is also easier for smaller nanoparticles to cross the cell membrane and cause intracellular cellular damage compared to larger nanoparticles [202, 204].

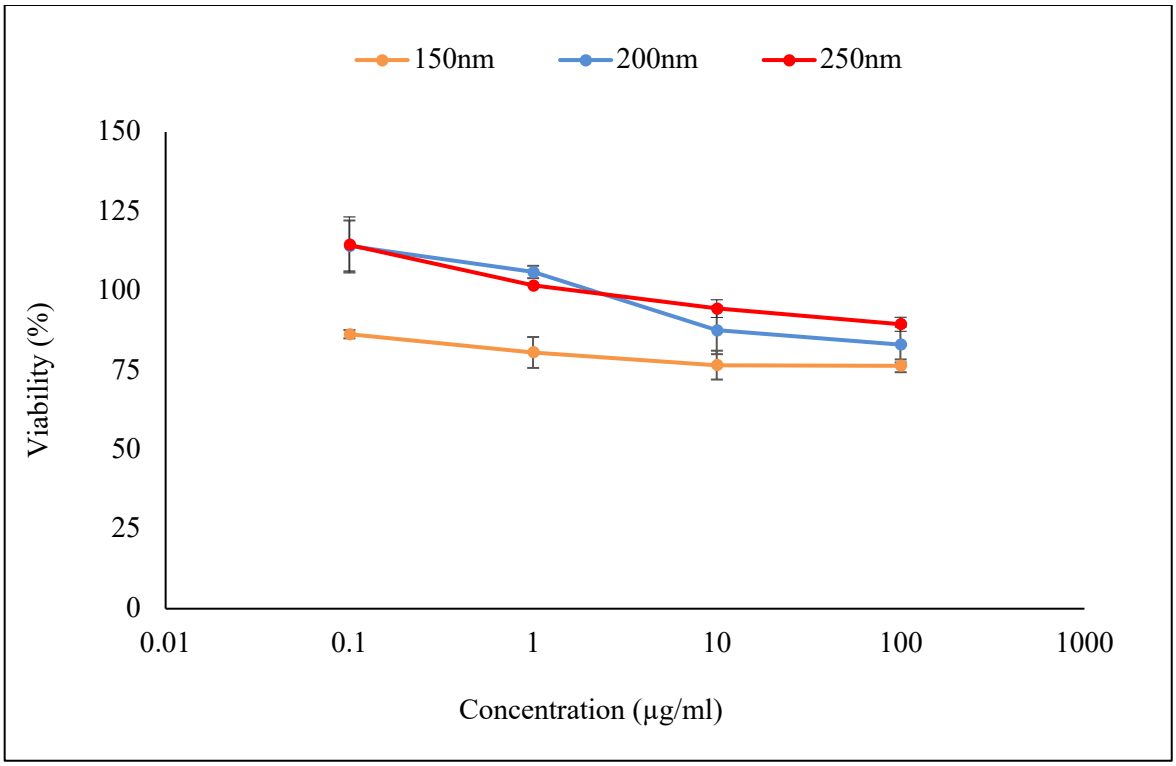

Figure 35 – Size dependent cytotoxicity study of targeted silica nanoparticle on HCT116 cell after 72 hours of nanoparticle exposure

4.5 Summary

Cell viability of HCT116 and CHO cells were evaluated by incubating them with targeted nanoparticles from 24 to 72 hours at doses range of 0.1-100 µg/ml. While HCT116 cells showed time and concentration dependent cell viability, the targeted nanoparticles had no impact on CHO cell viability. However, cell viability for both of the cells remained ~70% at the maximum time and concentration tested which is an indication of safe material according to literature.

Chapter 5: Receptor Expression Study

5.1 Motivation

Cell surface receptor expression plays a prime role in cellular uptake of the nanoparticles. An ideal target should have a high expression level on the cancer cell surface for the diagnostic and therapeutic application and it should also be highly specific to that cancer [184]. Targeting efficiency has been reported to be dependent on the cell surface receptor density and higher receptor density correlates with higher nanoparticles uptake [22]. *Zhang et al.* reported higher cellular uptake of hyaluronic acid-methotrexate prodrug self-assembling nanoparticles by HeLa cells compared to human lung adenocarcinoma cells (A549) due to the higher expression level of folate receptor on HeLa cells compared to A549 cells [17]. *Qhattal et al.* reported higher cellular uptake of hyaluronic acid conjugated liposomes by human lung adenocarcinoma cells (A549) compared to human breast cancer cells (MCF7) due to the higher expression level of CD44 receptor on A549 cells compared to MCF7 cells [22]. So, changes in receptor expression level on cell surface can affect the receptor-ligand interaction and consequently cellular uptake of the nanoparticles. [205].

The purpose of this experiment was to assess the expression of the targeted receptors i.e. CD44 and Folate receptor on various normal cells and colon cancer cells available in the laboratory. This study will help us to identify suitable cell models (cancer cell and control cell) for further targeting study.

5.2 Materials

Alexa Fluor 488 conjugated Rat (IgG2b,k) monoclonal antibody (anti human CD44), its' isotype control, zombie violet dye, fixation buffer were purchased from BioLegend. Alexa Fluor 647 conjugated Mouse (IgG1) monoclonal antibody (anti human FR) and its' isotype control were purchased from R&D systems. Stain buffer was made by dissolving Bovine Serum Albumin (Sigma Aldrich) in 1X Phosphate Buffer Saline (VWR). Block buffer was made by mixing Fetal Bovine Serum (VWR) with 1X Phosphate Buffer Saline. All chemicals were used without further purification.

Cells were purchased from American Type Culture Collection (ATCC). Human Colorectal Adenocarcinoma cells (HT-29, HCT-116 and SW-480) were maintained in Dulbecco's Modified Eagle's Medium (HyClone, GE Healthcare Life Sciences) supplemented with 10% FBS (VWR Life Science Seradigm), 1% L-glutamine (Corning cellgro, Manassas, VA) and 1% antibiotics. Human Epithelial Prostate (RWPE-1) cells were maintained in Keratinocyte Serum Free Medium supplemented with EGF and BPE (Gibco). Human Fibroblast (WI38) cells were maintained in Eagle's Minimum Essential Medium (HyClone, GE Healthcare Life Sciences) supplemented with 10% FBS (VWR Life Science Seradigm) and 1% antibiotics. Human Colorectal Adenocarcinoma (Caco-2) cells were maintained in Eagle's Minimum Essential Medium (HyClone, GE Healthcare Life Sciences) supplemented with 20% FBS (VWR Life Science Seradigm) and 1% antibiotics. Human Embryonic Kidney (HEK-293) cells were maintained in Eagle's Minimum Essential Medium (HyClone, GE Healthcare Life Sciences) supplemented with 10% FBS (VWR Life Science Seradigm). All cell lines were incubated at 37°C in 5% CO_2.

5.3 Methods

We have evaluated the expression of CD44 and Folate receptor on different mammalian cells with a BD Accuri C6 flow cytometer (BD Biosciences, San Jose, CA, USA) containing two lasers (488 and 635 nm). The instrument had a 533/30 band pass filter to examine the fluorescence emitted by 488 nm laser excitation and a 675/25 band pass filter to examine the florescence emitted by 635 nm laser excitation. We measured 10,000 events with a flow rate of 12 µL/min and recorded data for 2 minutes.

For each of the cell line, we have prepared nine eppendorf tubes with proper labeling. First, we have seeded 10^6cells/tube. 1µL/tube of zombie violet was added and kept for 15 minutes at room temperature in dark. Cells were washed twice with stain buffer. 5µL/tube of block buffer was added and kept for 1 hour at room temperature. 100µg/tube of CD44 and FR antibodies were added and kept for 2 hours at room temperature in dark. Cells were washed twice with stain buffer. 0.5 ml/tube of fixation buffer was added and kept for 1 hour at room temperature in dark. Cells were washed twice with stain buffer. Cells were re-suspended in 0.5 ml/tube stain buffer and filtered through 40µm filter. Cells were kept in 4°C and away from light before analysis in Flow

Cytometer. Unstained cells and cells with isotype antibodies were used as controls. Reagents in the 9 tubes were in the following manner-

Table 2– Reagents in the flow cytometer tubes

Tube#	Unstained cells	CD44 antibody	FR antibody	Zombie dye
1	x			
2		x		
3			x	
4				x
5		x	x	
6		x		x
7			x	x
8		x	x	x
9	Mixture of isotype antibodies			

5.4 Results and Discussion

We have evaluated the expression of CD44 and Folate Receptors on 4 different Human Colorectal Adenocarcinoma cells (HT-29, HCT-116, Caco-2 and SW-480) and 3 different normal cells - Human Fibroblast (WI38) cells, Human Embryonic Kidney (HEK-293) cells and Human Epithelial Prostate (RWPE-1) cells. We have analyzed the cells using FACS (Fluorescence Activated Cell Sorting) analysis which is a technique of flow cytometry. In this technique, we have investigated the cells with common characteristics and eliminated results from dead cells, debris and doublets using sequential gating process. For each of the cell line, we have presented the data in dot plots and histograms. The dot plots show the relationship between 2 parameters on a scatter plot with each event being represented as a single dot. In this study, the dot plots are showing the relationship between CD44 and FR positive cells. We have used quadrant gate in the dot plots. Top right quadrant shows the % of cells positive for both receptors, bottom right one for CD44 positive cells, bottom left one shows the % of cells negative for both receptors and top left one for FR positive cells. Histograms are plots of single parameter where the Y axis represents the number of events (cell count) that show a given fluorescence and the X axis represents the relative fluorescence intensity detected in a single channel. If a large number of events show a specific fluorescence intensity, it is identified as a peak on the histogram.

5.4.1 Colon cancer cells

Figure 36 shows the histogram of CD44 fluorescence of the 4 colon cancer cells. As can be seen from the figure, all the cancer cell lines except Caco2 express the CD44 receptor because the cells stained with CD44 antibody showed much higher fluorescence intensity compared to the unstained and control cells. However, the expression level of CD44 is not same in all the cell lines. Based on the fluorescence intensity, SW480 cells showed ~5 and ~8.5 fold higher expression of CD44 than HCT116 and HT29 cell lines.

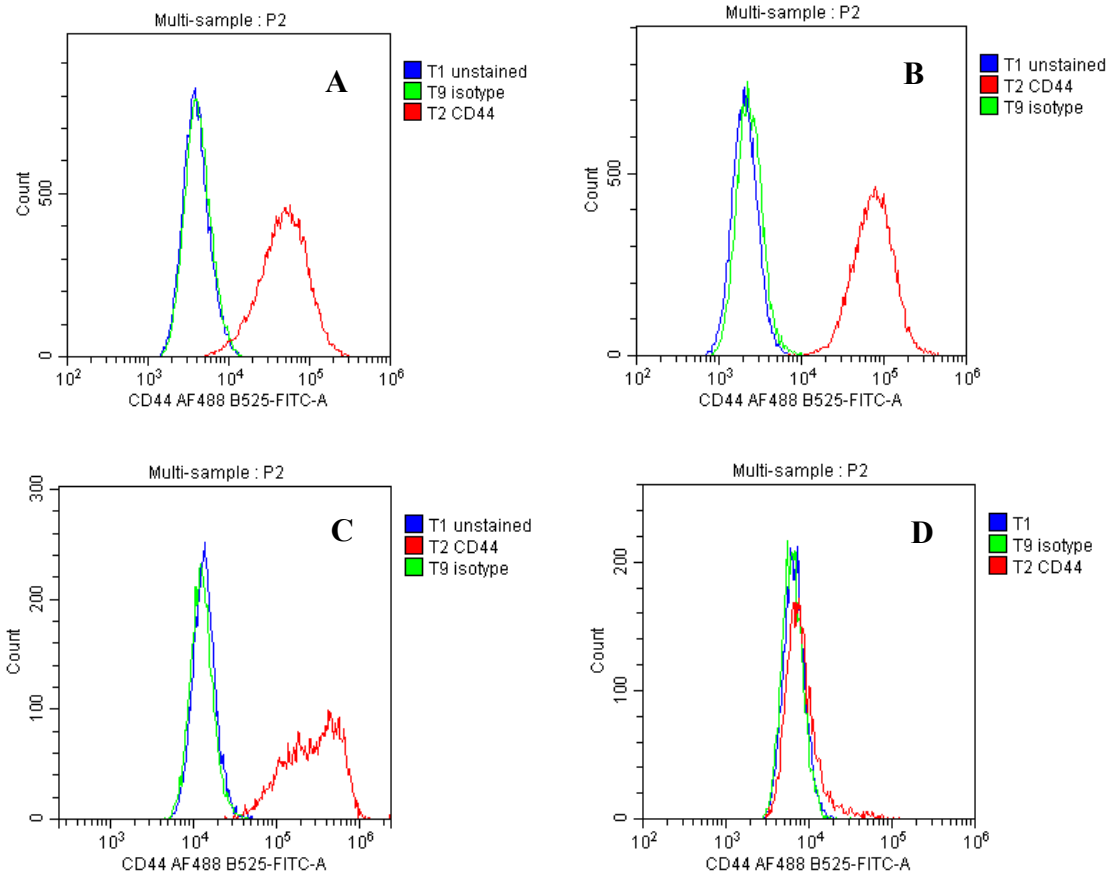

Figure 36 – Histogram with associated CD44 fluorescence of A) HT29, B) HCT116, C) SW480 and D) Caco2 cell lines

Figure 37 shows the histogram of FR fluorescence of the 4 colon cancer cells. As can be seen from the figure, all the cancer cell lines express the FR because the cells stained with FR antibody showed much higher fluorescence intensity compared to the unstained and control cells. However, the expression level of FR is not same in all the cell lines. Based on the fluorescence intensity, HT29 and HCT116 cell lines showed very similar expression of FR whereas SW480 and Caco2 cell lines were on the similar level. The later pair showed ~2 fold higher expression of FR than the former.

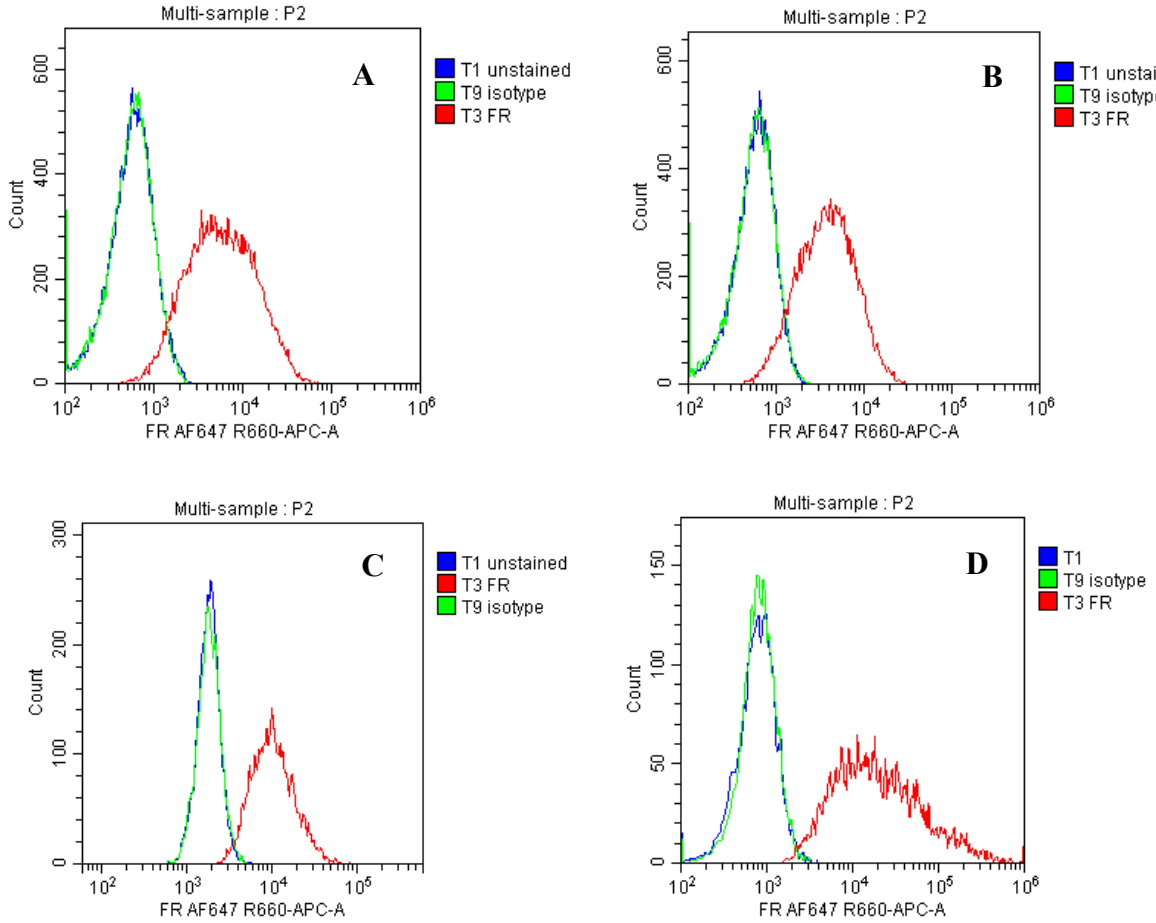

Figure 37 – Histogram with associated FR fluorescence of A) HT29, B) HCT116, C) SW480 and D) Caco2 cell lines

Figure 38 shows the dot plots of receptor positivity. As can be seen from the figure, 59% of HT29 cells, 74% of HCT116 cells and 85% of SW480 cells are positive for both CD44 and FR whereas only 9% of Caco2 cells show positivity for both receptors.

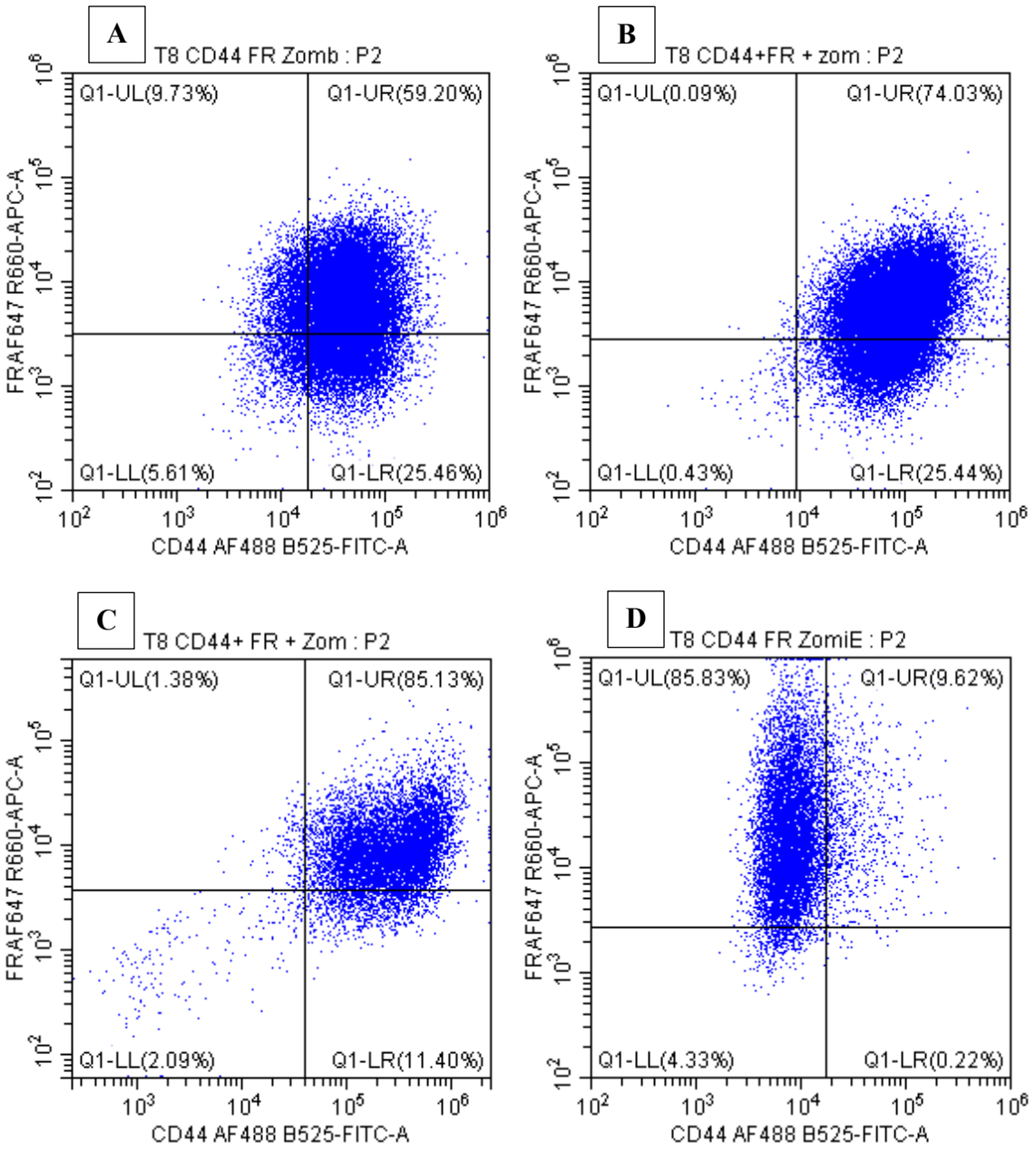

Figure 38 – Dot plots for receptor positivity of A) HT29, B) HCT116, C) SW480 and D) Caco2 cell lines

5.4.2 Normal cells

Figure 39 shows the histogram of CD44 fluorescence of the 3 normal cells. Based on the fluorescence intensity from the figure, it can be stated that all the normal cell lines express the CD44 receptor at different level. WI38 cells showed the highest expression level followed by HEK293 and RWPE1 cell lines.

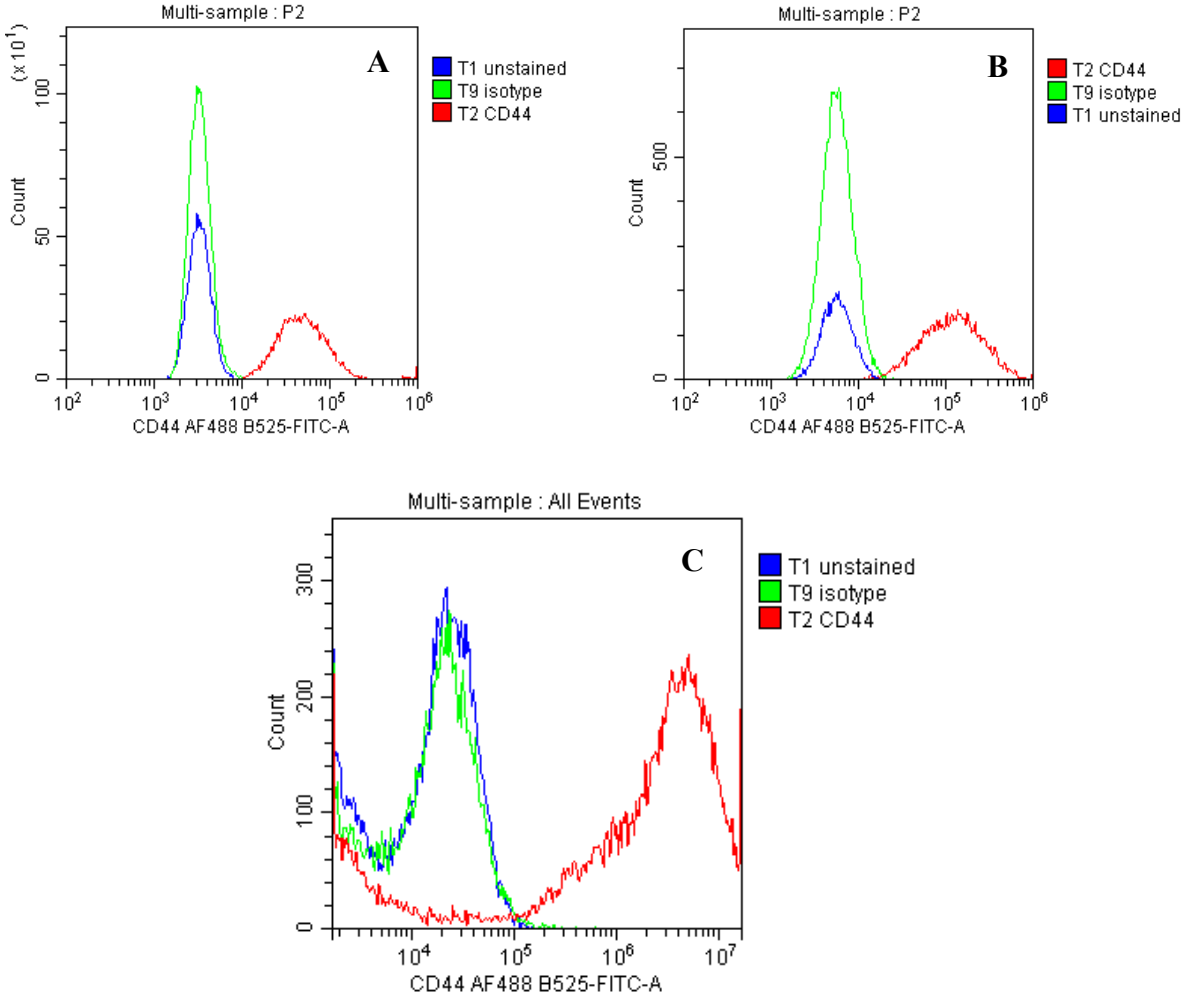

Figure 39 – Histogram with associated CD44 fluorescence of A) RWPE1, B) HEK293 and C) WI38 cell lines

Figure 40 shows the histogram of FR fluorescence of the 3 normal cells. Based on the fluorescence intensity from the figure, it can be said that all the normal cell lines except WI38 express the folate receptor at different level. HEK293 cells showed ~5.5 fold higher expression of FR than RWPE1 cell line. For WI38 cell line, the fluorescence intensity of the isotype control is similar to that of FR antibody which is why there is lack of presence of FR on WI38 cell line.

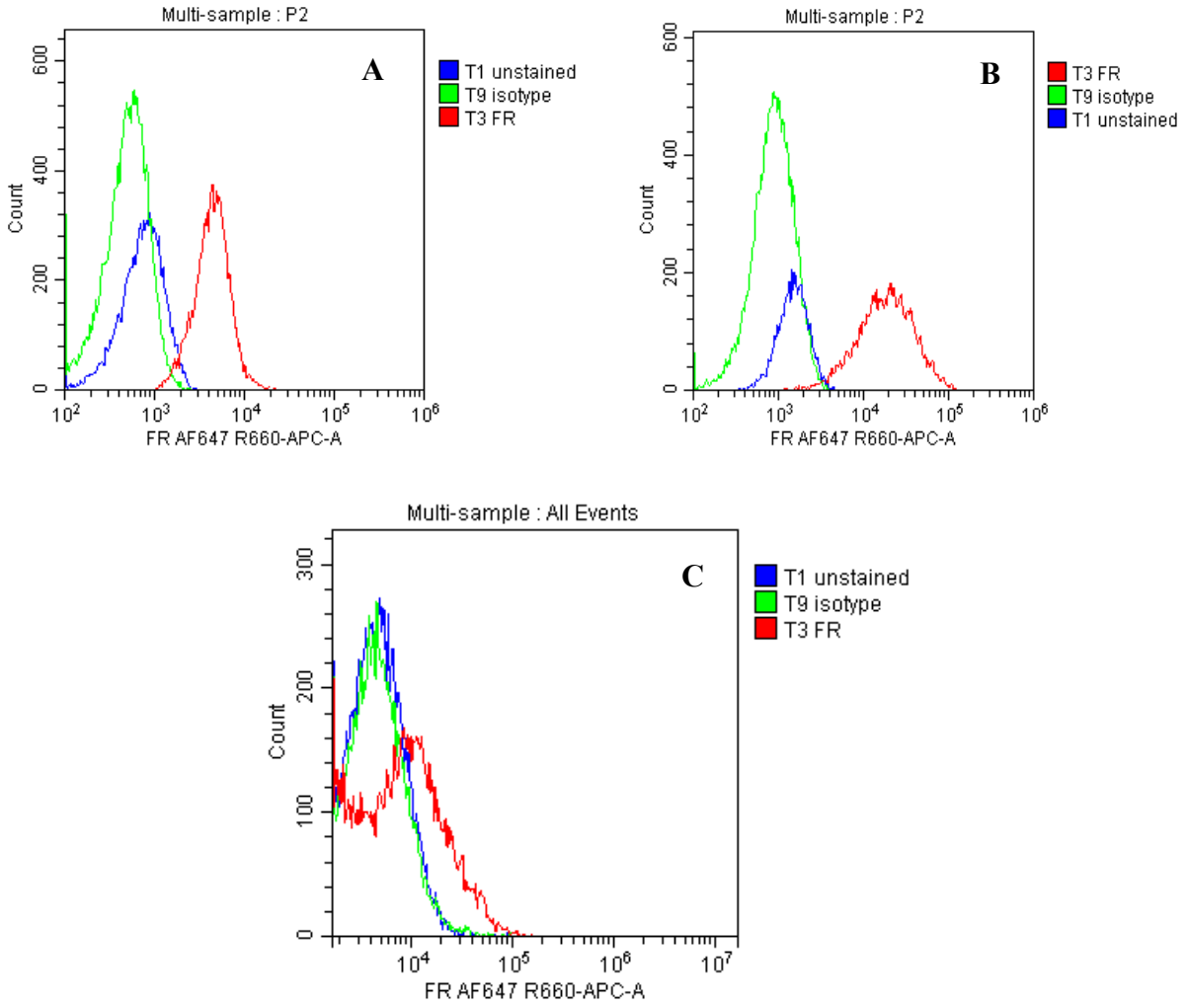

Figure 40 – Histogram with associated FR fluorescence of A) RWPE1, B) HEK293 and C) WI38 cell lines

Figure 41 shows the dot plots of receptor positivity. As can be seen from the figure, 60% of RWPE1 cells and 93% of HEK293 cells are positive for both CD44 and FR whereas only ~1% of WI38 cells show positivity for both receptors.

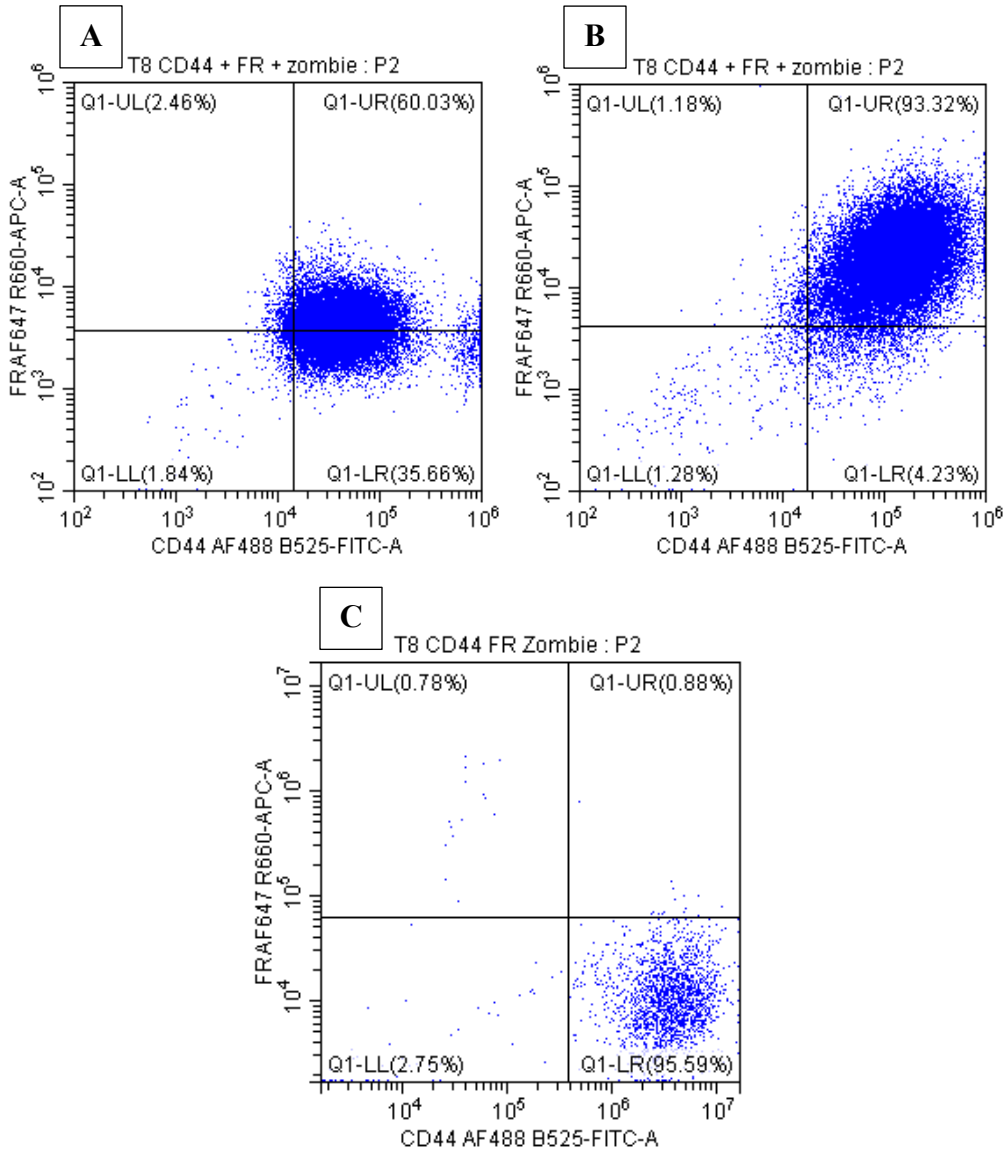

Figure 41 – Dot plots for receptor positivity of A) RWPE1, B) HEK293 and C) WI38 cell lines

5.5 Summary

The expression of CD44 and FR were evaluated using Flow Cytometer on four different colon cancer cell lines and three different normal cell lines available in the laboratory. All the cancer and normal cells except Caco2 and WI38 expressed both of the receptors. WI38 expressed only CD44 and Caco2 expressed only folate receptors. 85% of the SW480 cells expressed both of the receptors and the expression level for each of the receptor was higher compared to other cell lines. Based on this study, we have decided to use SW480 cell line as positive for both receptors, WI38 cell line as positive for only CD44 receptor and Caco2 cell line as positive for only folate receptor in the cellular targeting experiment.

Chapter 6: Immunohistochemical Staining (IHC) staining of Neuroendocrine tumor

6.1 Motivation

Neuroendocrine tumors (NETs) emerge from the neuroendocrine cells of the endocrine system. It is a slow growing malignant tumor of heterogeneous nature [206-210]. This tumor is most commonly found in gastrointestinal tract, lung and pancreas but may also grow in breast, prostate and skin [206, 208, 209]. NETs are divided into well differentiated (low grade tumor i.e. grade 1 and 2) and poorly differentiated (high grade tumor i.e. grade 3) tumors [208, 209]. NET biomarkers are divided into specific markers (Serotonin, Gastrin, Insulin, Glucagon and Somatostatin) and non-specific markers (Chromogranin A, Neuron-specific enolase, Pancreatic polypeptide and Human Chorionic Gonadotropin) [210]. NETs can be diagnosed by pathology testing, hormonal testing, diagnostic imaging (Computed Tomography or Magnetic Resonance Imaging) and endoscopic imaging (Ultrasonography) [208]. Major treatment options for NETs are surgery, chemotherapy, radiopeptide therapy, somatostatin analogues, vascular endothelial growth factor inhibitors etc. [211].

The purpose of this experiment was to analyze the expression of CD44 and FR in NET tissues of actual patients using Immunohistochemical (IHC) staining. IHC is a technique used to detect the presence and location of specific antigens in tissue sections. IHC staining is conducted with antibodies which bind to specific antigens. The antigen-antibody interaction is then visualized either with chromogenic detection or with fluorescent detection using fluorescence microscopy. The fluorescent detection can be ‘direct’ where the fluorophore is conjugated to the primary antibody or ‘indirect’ where the fluorophore is conjugated to the secondary antibody that binds to the primary antibody.

6.2 Materials

CD44 Recombinant Rabbit Monoclonal Antibody, Rabbit IgG Isotype Control, FOLR1 Monoclonal Antibody, Mouse IgG1 kappa Isotype Control, Alexa Fluor 647 conjugated Goat anti-mouse IgG1 Secondary Antibody, 2.5% normal goat serum and DAPI (4',6-Diamidino-2-Phenylindole, Dihydrochloride) were purchased from ThermoFisher Scientific. Alexa Fluor 555 conjugated Goat Anti-Rabbit IgG Secondary Antibody were purchased from Abcam. Xylene was

purchased from Thomas Scientific. Cytoseal mounting medium and 1X Phosphate Buffer Saline were purchased from VWR. All chemicals were used without further purification.

The study included 3 slides of neuroendocrine tumor of 3 different grades from actual patients. Formalin-fixed paraffin-embedded (FFPE) tumor tissue sections were mounted onto glass slides. Tissue slides were kept in room temperature until use.

6.3 Method

Multiplex Immunohistochemical (IHC) staining was used to analyze the expression of CD44 and FR on the slides. Slides were heated in an oven at 60°C for 2 hours prior to use.

6.3.1 Step 1 – De-paraffinization and Rehydration

Tissue sections were de-paraffinized using organic solvents (xylene, 100%, 3x) and an alcohol series (ethanol, 100%, 70%, 30%, 1x each). Tissue sections were hydrated using distilled water (2x).

6.3.2 Step 2 – Heat Induced Antigen Retrieval

Tissue slides were immersed in 100 ml of 10 mM sodium citrate buffer (pH 6). Slides were heated in a microwave for 1 minute at power level 10 and 5 minutes at power level 1. Slides were cooled for 15 minutes at room temperature and then washed with PBS (3x).

6.3.3 Step 3 – Staining

100µl of 2.5% normal goat serum was applied over the tissue section to inhibit non-specific binding of the antibodies. Slides were incubated for 1 hour at room temperature in a humidified chamber. Slides were washed with PBS (3x). 100 µl of 1 µg/ml primary antibody for CD44 was applied over the tissue section and incubated overnight at room temperature in a humidified chamber. Slides were washed with PBS (3x). 100 µl of 1 µg/ml secondary antibody for CD44 was applied over the tissue section and incubated for 1 hour at room temperature in a humidified chamber. Slides were washed with PBS (3x). Same procedure was followed for FR antibody. 75µl of DAPI was applied over the tissue section and incubated for 5 minutes at room temperature in a humidified chamber. Slides were washed with PBS (3x).

6.3.4 Step 4 – Mounting and Imaging

Mounting medium was added on the slide and coverslip was placed. Antibody staining was observed and images were taken with fluorescent microscope. Slides were stored at -20^{o}C before further use.

6.4 Results and Discussion

For qualitative analysis, we have taken images from 10 different locations of each slide. We have used 10x magnification under 3 fluorescent channels to take images of cell nucleus (DAPI), CD44 (RFP) and FR (Cy5). For quantitative analysis, we have used ImageJ software.

6.4.1 Qualitative analysis – Receptor expression

Figure 42-44 show the immunofluorescence images of grade 1, 2 and 3 NET tissues respectively. Images are of nuclei stained with DAPI (blue), CD44 (red) and FR (yellow) stained with their respective antibodies on 10 different locations of each grade slide. As can be seen from the qualitative images, both CD44 and FR showed some fluorescence signals around the cell nucleus which marks their existence in NETs. However, CD44 showed stronger fluorescence signal compared to FR in all 3 grades which gives us an idea about higher expression of CD44 compared to FR in NETs. From the qualitative images it is difficult to make a conclusion about the dependence of receptor expression intensity on tumor grade since the locations were random in each grade.

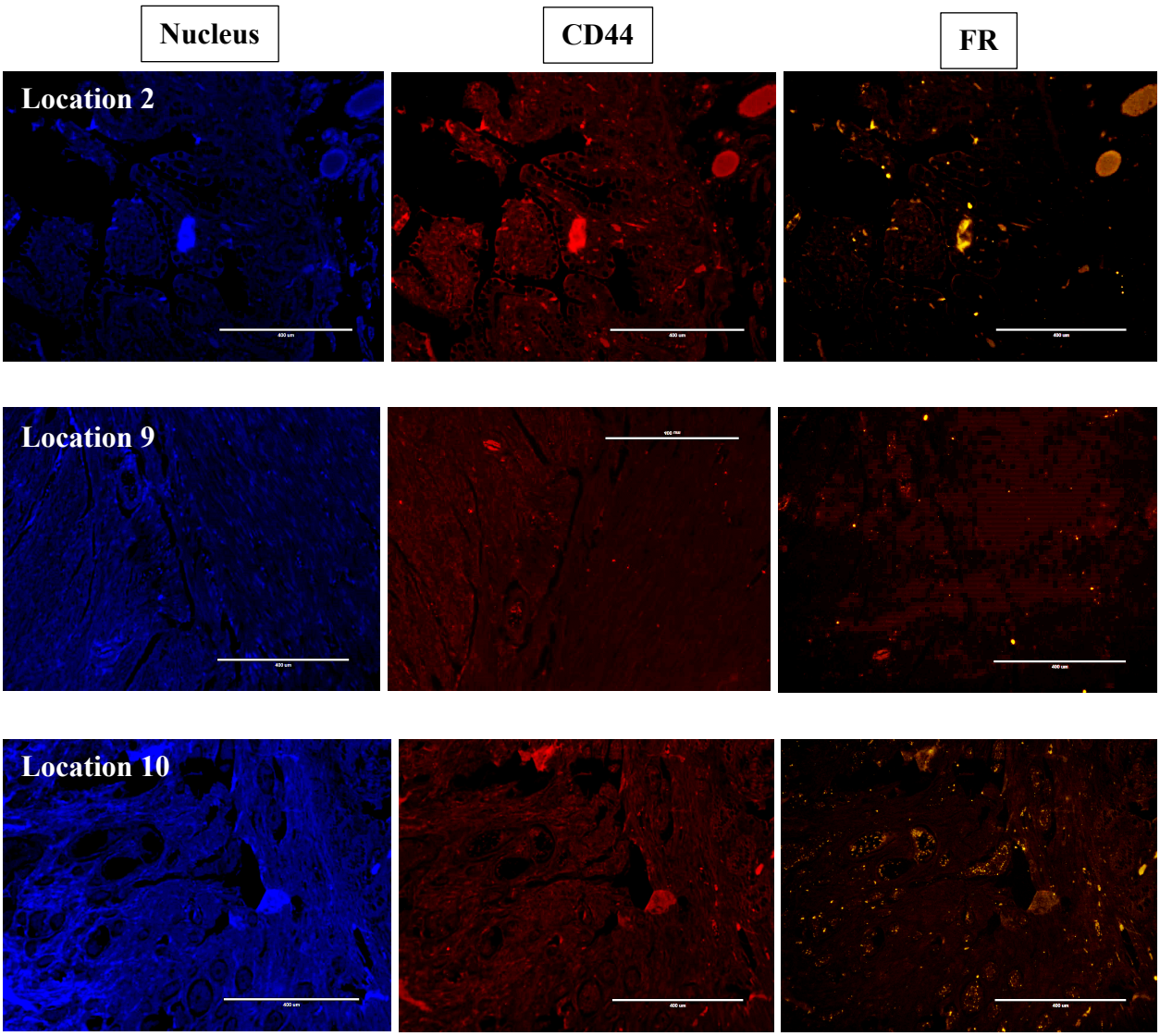

Figure 42 – IHC staining on Grade 1 NET

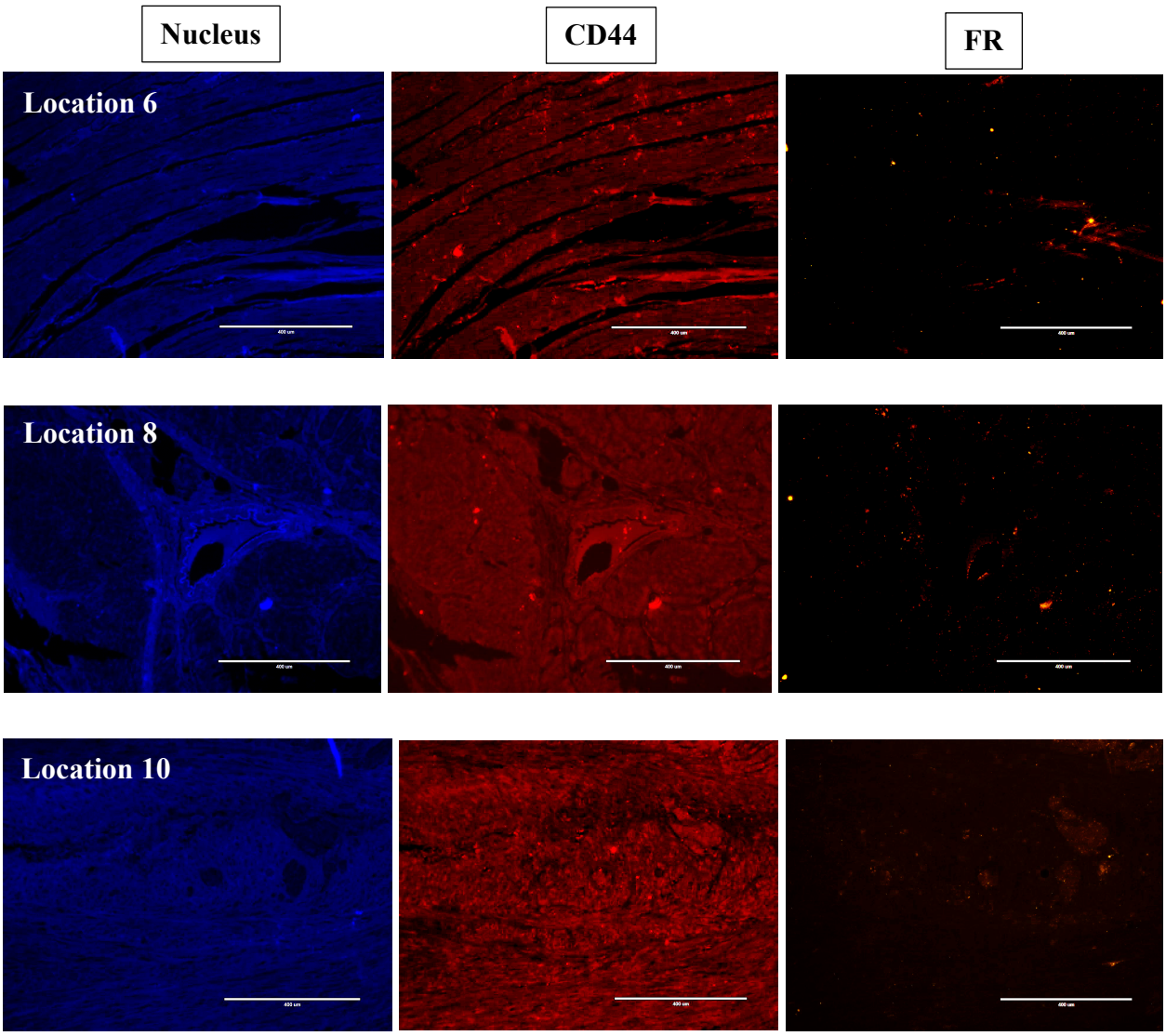

Figure 43 – IHC staining on Grade 2 NET

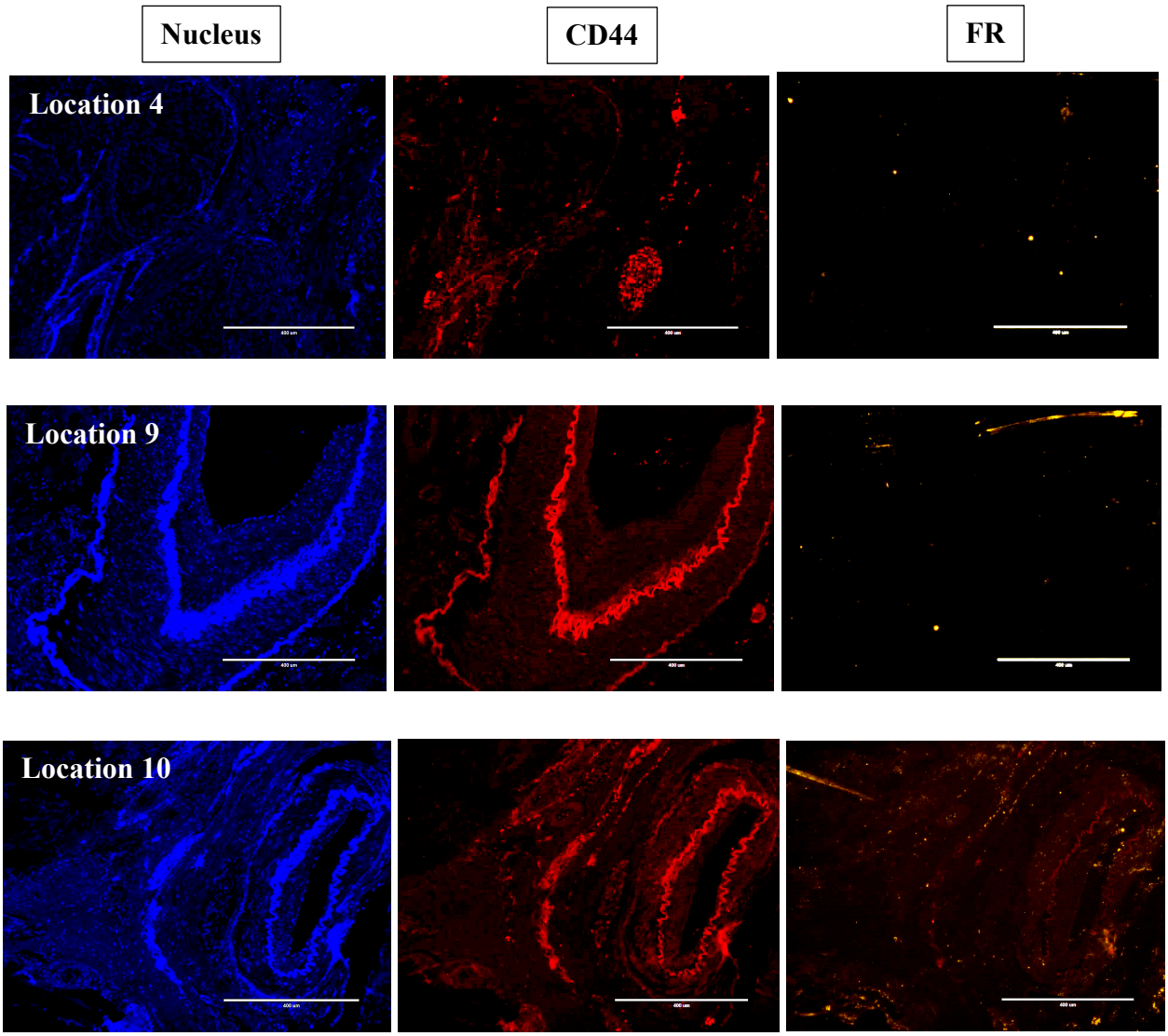

Figure 44 – IHC staining on Grade 3 NET

6.4.2 Semi-quantitative analysis – Receptor expression

Percentage area positivity for CD44 and FR were compared among grade 1, 2 and 3 NET tissues. Figure 45 and 46 show the percentage area positivity for CD44 and FR respectively on 10 different locations of each grade slide. As can be observed from figure 45, grade 1 and 2 showed similar percentage of area positivity for CD44 receptor. However, grade 3 showed much higher percentage of area positivity for CD44 receptor compared to the other 2 grades. Figure 46 showed that there was a stepwise increase in the percentage area positivity for FR with tumor grade. So, it can be

concluded from the figures that density of CD44 and FR depend on tumor grade and it increases with tumor stage. Comparison between CD44 and FR area positivity showed that grade 1 and 3 had higher percentage of area positivity for CD44 compared to FR which can be correlated with our qualitative results.

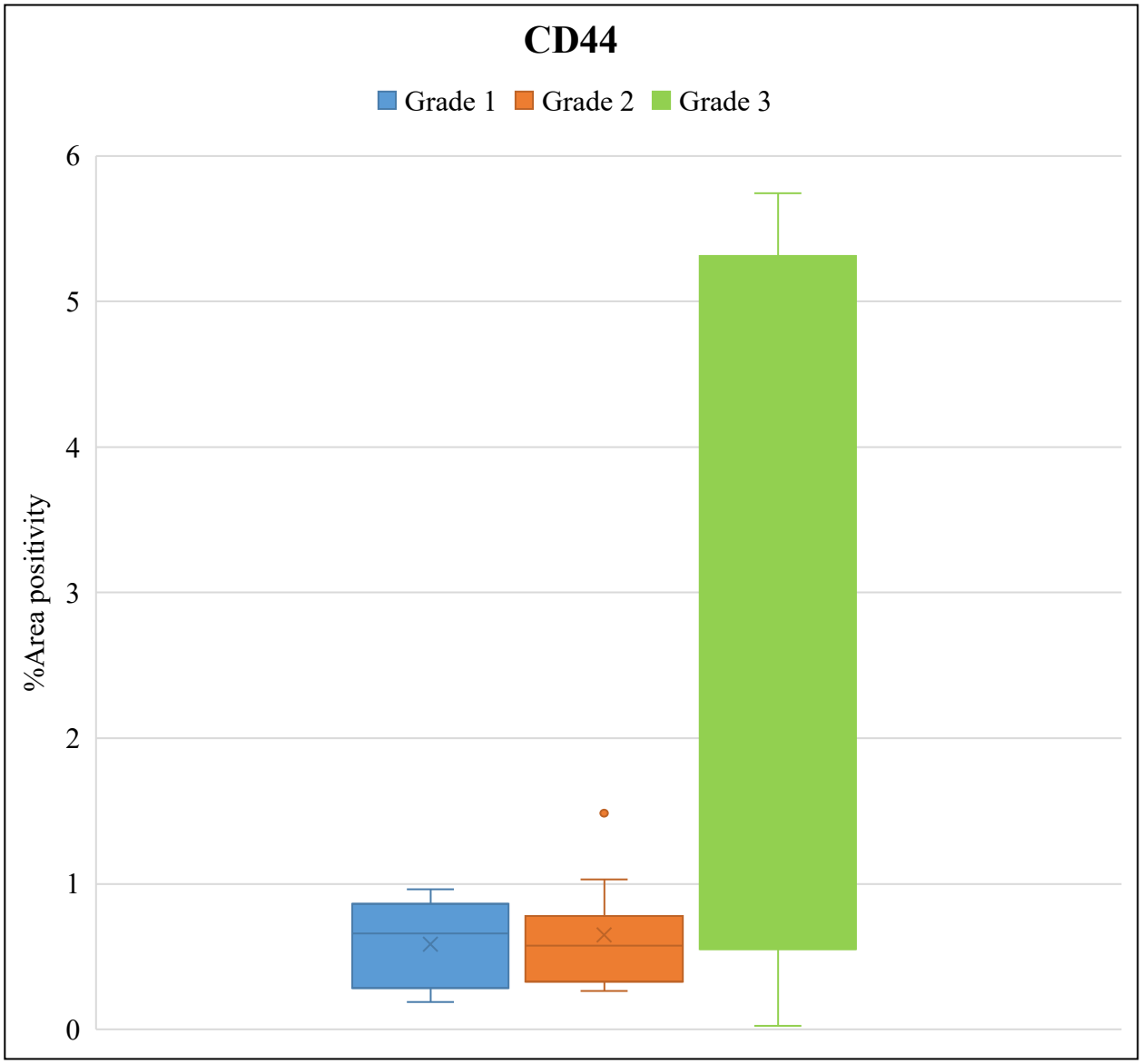

Figure 45 – Semi-quantitative analysis of CD44 expression on NET

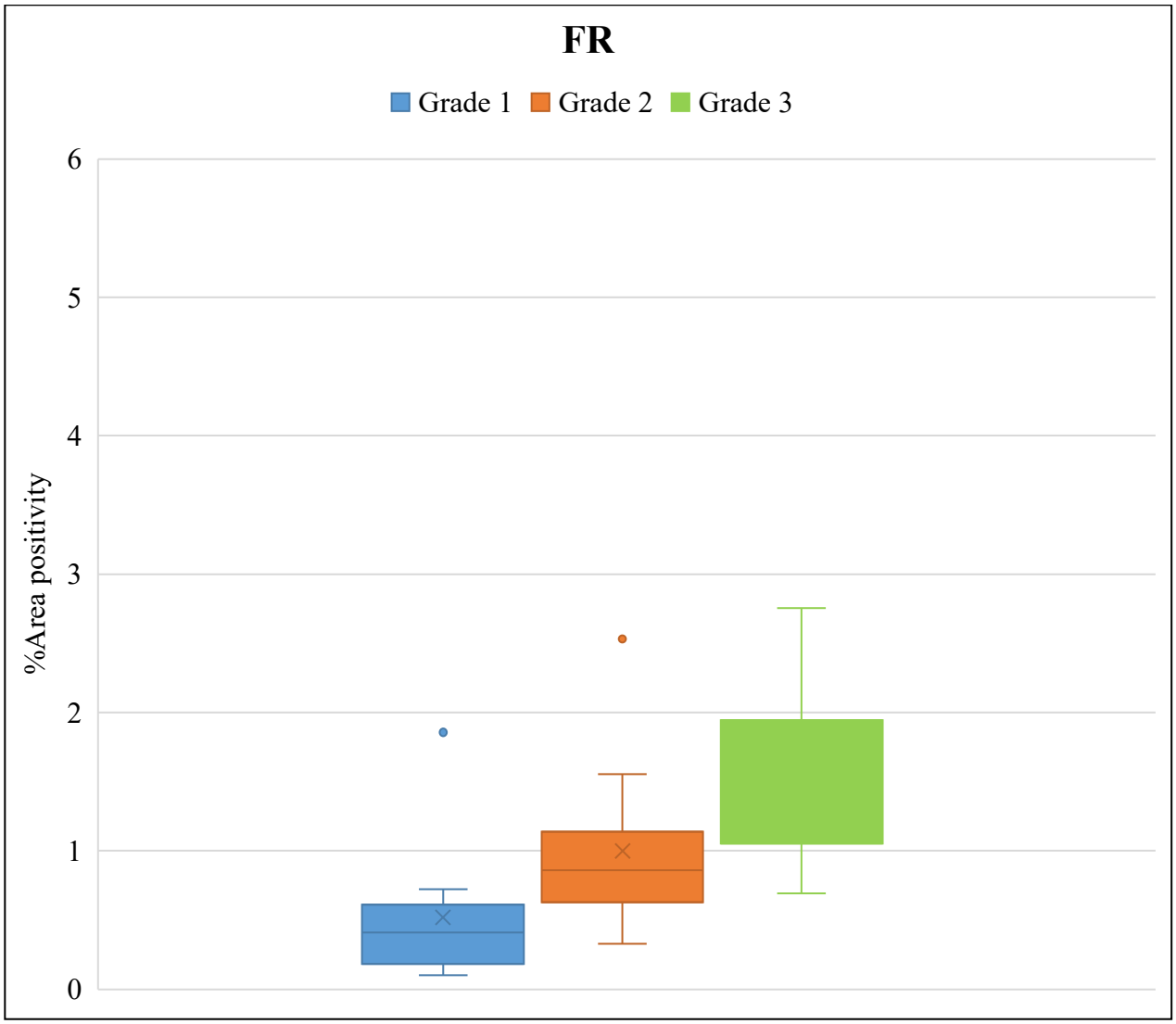

Figure 46 – Semi-quantitative analysis of FR expression on NET

6.4.3 Qualitative analysis – Targeted nanoparticle

Next, we have applied a non-targeted nanoparticle and a dual targeted nanoparticle (H:F:A=1.25:9:1) in the NET tissue of grade 3. Figure 47 show the qualitative images from 4 different regions (out of 6) of each sample. As can be seen from the images, both types of nanoparticles showed some fluorescence signals in the tissues. However, targeted NP showed comparatively stronger fluorescence than the non-targeted one which gives us an idea about their targeting efficacy.

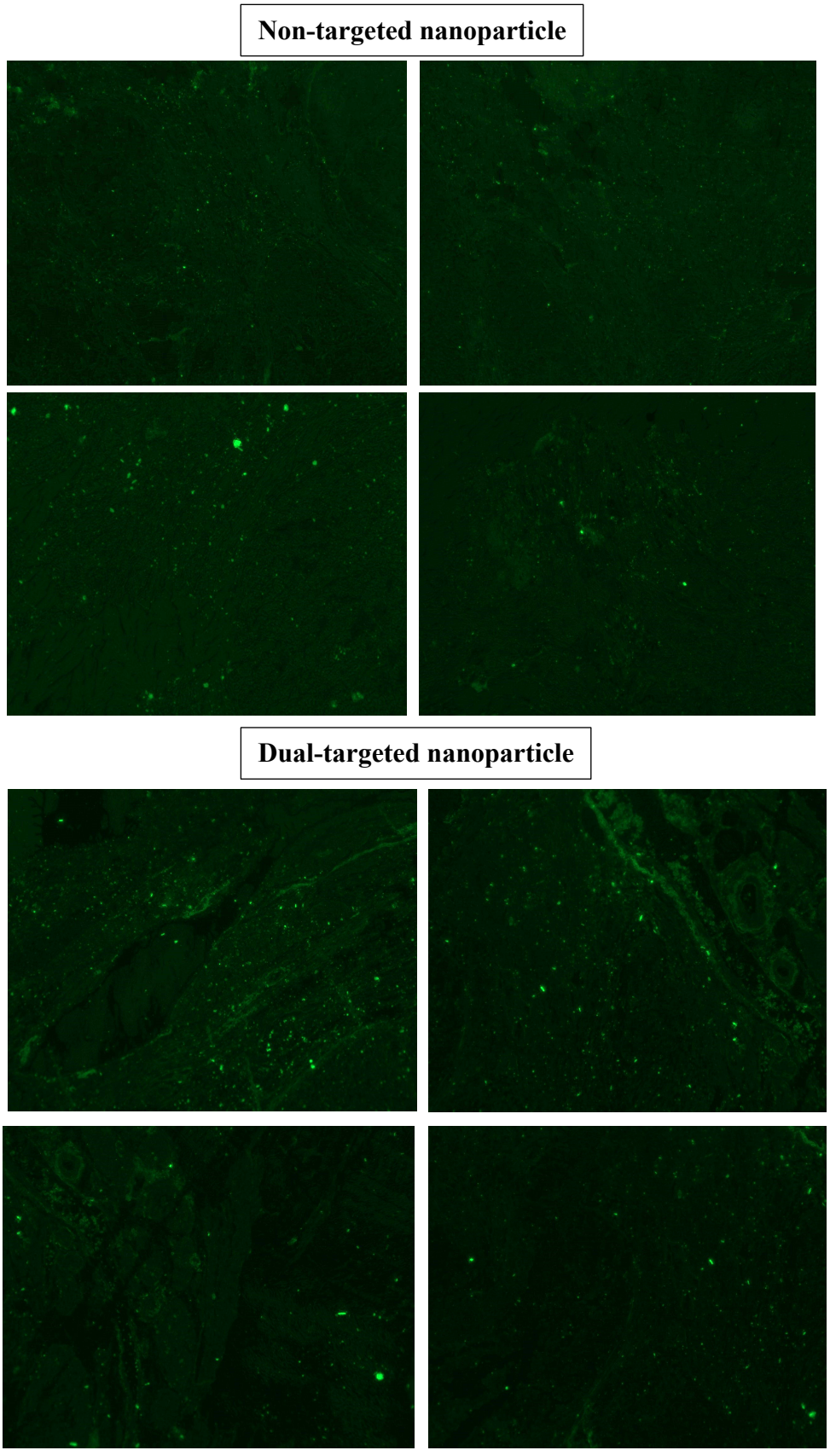

Figure 47 – IHC staining on Grade 3 NET by nanoparticle

6.4.4 Semi-quantitative analysis – Targeted nanoparticle

From figure 48 which is the semi-quantitative analysis of 6 different regions under each slide, it can be observed that, the dual targeted nanoparticle showed much higher percentage of area positivity compared to the non-targeted one which gives us an idea about their targeting efficacy. This could be due to the CD444-HA and FA-FR interactions since we have observed the existence of our 2 targeted receptors in NETs.

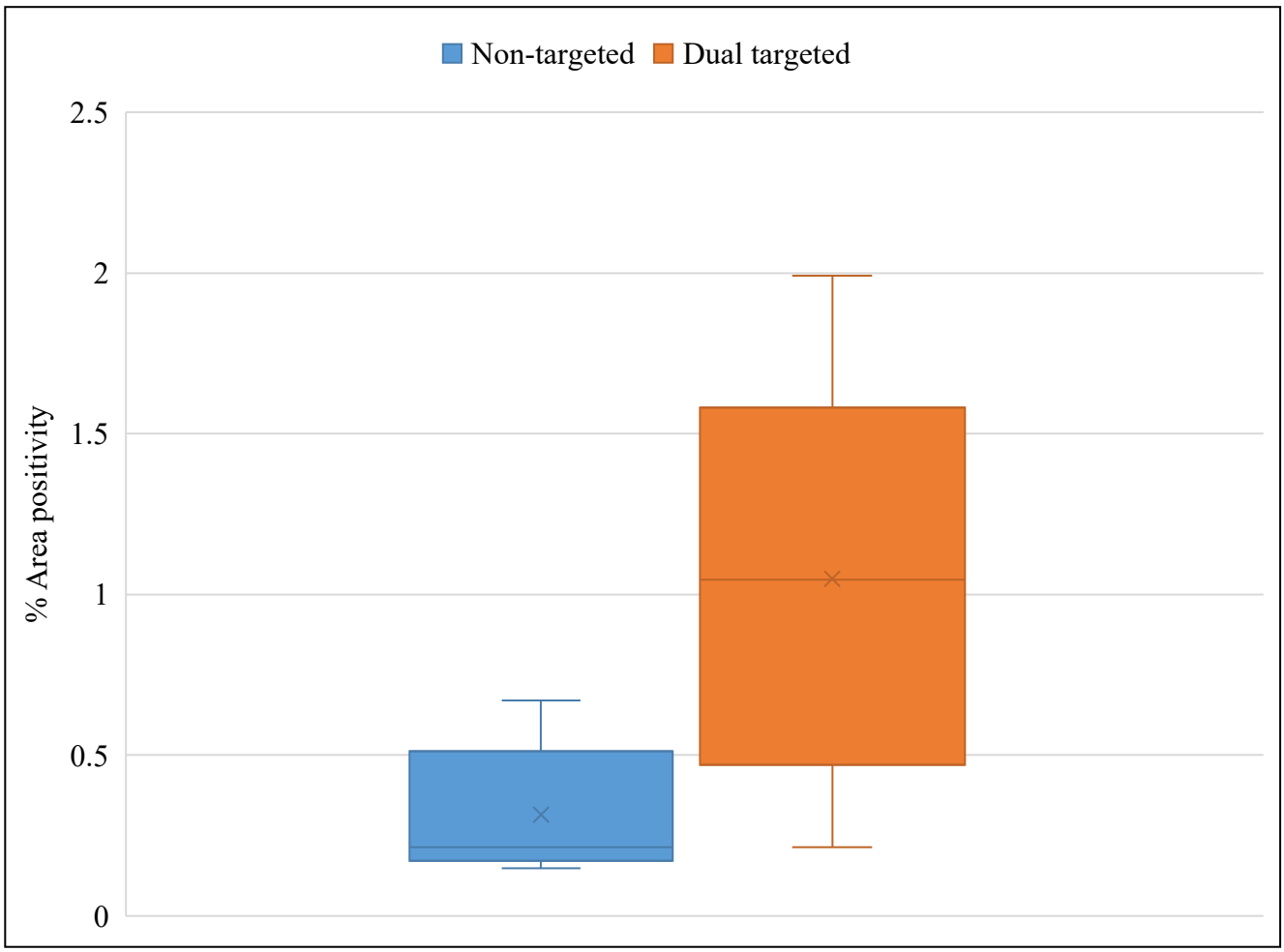

Figure 48 – Semi-quantitative analysis of NET targeting by nanoparticle

6.5 Summary

The expression of CD44 and FR were evaluated using IHC staining on 3 different grades of NET tissues. From the preliminary results, it can be concluded that NETs have higher expression of CD44 compared to FR and their expression increases as a function of tumor grade. The dual

targeted nanoparticle showed much higher percentage of area positivity compared to the non-targeted one which gives us an idea about their targeting efficacy. However, experiment with other targeted nanoparticles on different grades of NETs is required to study the impact of nanoparticle ligand density on targeting of different grades of tumor tissues from actual patients.

Chapter 7: Cellular Uptake of Targeted Silica Nanoparticles

7.1 Motivation

The success of the nanoparticles developed for delivering different molecules (i.e. genes, drugs, and contrast agents) to the nucleus and other intracellular sites depends on their intracellular fate. To achieve high therapeutic efficacy, nanoparticles safe passage to the cells is an important step [42]. Nanoparticle surface is modified with targeting ligands which recognize and bind to overexpressed specific biomarkers on cancer cells [5, 8, 12, 13] and deliver chemotherapeutic drug to the cancer cells. This specific targeting increases the concentration of the cytotoxic drug at the cancer site and reduces non-specific toxicity [9, 10, 14]. Targeted nanoparticles can also deliver the imaging agent to the cancer cells. However, for efficient cancer targeting, the targeted receptors should be exclusively overexpressed by the cancer cells and this expression should be homogeneous on all the targeted cancer cells [9, 26, 31]. Multiple receptors targeting is also necessary because of the heterogeneous nature of the cancer cell [16] and expression of some targeted receptors on normal cells [17]. Apart from the cell surface receptor, cancer targeting efficiency also depends on the targeting ligand's density, binding affinity and selectivity towards targeted receptor [26, 38]. The targeting ligand should have high specificity and binding affinity towards the targeted receptor which will strengthen their interaction. It should also possess low immunogenicity. Another way to increase the cancer cell targeting efficiency is to conjugate dual targeting ligands on the nanoparticle surface. While single targeted nanoparticles target only one type of cell surface receptor, dual targeted nanoparticles simultaneously target two different types of cell surface receptors which enhances the targeting potency of the nanoparticles. In order to evaluate the targeting efficacy of the nanoparticles, we conducted qualitative and quantitative *in vitro* cellular uptake studies.

7.2 Materials

Tetramethyl orthosilicate (TMOS-98%), Triton X-100 and (3-Aminopropyl)trimethoxysilane (APTMS) were purchased from Acros Organics; n-hexanol (99%), fluorescamine, ethanolamine, 1-Ethyl-3-(3 dimethylaminopropyl)carbodiimide (EDC), N-Hydroxysuccinimide (NHS) and fluorescein isothiocyanate were purchased from Alfa Aesar; cyclohexane, aqueous ammonia solution (29wt% ammonia), sodium hydroxide and dimethyl sulfoxide (DMSO) were purchased

from BDH Chemicals; ethanol was purchased from Decon Labs; hyaluronic Acid (8kDa) was purchased from Amazon; folic Acid (≥97%) was purchased from Enzo Life Sciences; cetrimonium bromide was purchased from Spectrum Chemicals; thiazoyl blue tetrazolium bromide (MTT), sodium acetate was purchased from Amresco; acetic acid was purchased from Macron Fine Chemicals; coomassie brilliant blue dye was purchased from Bio-Rad; bovine serum albumin was purchased from Sigma Aldrich. 1X Phosphate Buffer Saline was purchased from VWR. DAPI (4′,6-diamidino-2-phenylindole) was purchased from ThermoFisher Scientific. All chemicals were used without further purification. Deionized water used throughout the experiments was purified with an ELGA PURELAB Flex water purification system.

Cells were purchased from American Type Culture Collection (ATCC). Human Colorectal Adenocarcinoma cells (SW-480) were maintained in Dulbecco's Modified Eagle's Medium (HyClone, GE Healthcare Life Sciences) supplemented with 10% FBS (VWR Life Science Seradigm), 1% L-glutamine (Corning cellgro, Manassas, VA) and 1% antibiotics. Human Fibroblast (WI38) cells were maintained in Eagle's Minimum Essential Medium (HyClone, GE Healthcare Life Sciences) supplemented with 10% FBS (VWR Life Science Seradigm) and 1% antibiotics. Human Colorectal Adenocarcinoma (Caco-2) cells were maintained in Eagle's Minimum Essential Medium (HyClone, GE Healthcare Life Sciences) supplemented with 20% FBS (VWR Life Science Seradigm) and 1% antibiotics. All cell lines were incubated at 37°C in 5% CO_2.

7.3 Methods

7.3.1 Quantitative cellular uptake

40,000cells/well were seeded in a 96 well plate and incubated overnight at 37ºC. After overnight incubation, the culture media was renewed with culture media containing different concentration of nanoparticles. Plates with each nanoparticle concentration was incubated for desired time point. Then the media was aspirated and kept to a different 96 well-plate. The cells were thoroughly rinsed thrice with ice cold 1X PBS (pH 7.4, 4 °C) to eliminate excess nanoparticles and dead cells. Then the cells were lysed using lysis buffer for 60 minutes at room temperature. After lysis, the well plate was vortexed for 5 minutes at 500 rpm. The fluorescence intensity of FITC associated with the cells and the media were measured in the lysis buffer extract and the aspirated culture

media respectively by a fluorescent spectrophotometer at an excitation wavelength of 495 nm and emission wavelength of 525 nm. Then the fluorescence was converted to the number of internalized nanoparticles based on the standard curve obtained with known nanoparticle concentration in the lysis buffer and culture media using fluorescent spectrophotometer. Cells without nanoparticle treatment was used as control.

Cellular uptake of each nanoparticle sample was calculated using the equation,

$$\% \text{ Uptake} = \frac{\text{Fluorescence of cell associated nanoparticle}}{\text{Fluorescence of nanoparticle added}} \text{ x } 100\%$$

Selectivity of each nanoparticle sample was calculated using the equation,

$$\text{Selectivity} = \frac{\text{Concentration of nanoparticle uptaken by SW480 cell}}{\text{Concentration of nanoparticle uptaken by WI38 or Caco2 cell}}$$

Distribution co-efficient of each nanoparticle sample was calculated using the equation,

$$\text{Distribution co-efficient} = \frac{\text{Concentration of nanoparticle uptaken by cell}}{\text{Concentration of nanoparticle in the media}}$$

We have followed the same protocol while conducting the competitive inhibition study with an exception that the cells were incubated with different concentration of free ligand mixture for 3 hours before nanoparticle addition.

7.3.2 Qualitative cellular uptake

100,000cells/well were seeded in a 6 well plate and incubated overnight at 37ºC. After incubation, the culture media was renewed with culture media containing different concentration of nanoparticles. Plates with each nanoparticle concentration was incubated for desired time point. The cells were thoroughly rinsed thrice with ice cold 1X PBS (pH 7.4, 4 °C) to eliminate excess nanoparticles and dead cells. Then the cells were fixed with 4% paraformaldehyde for 1 hour at room temperature. The cells were thoroughly rinsed thrice with ice cold 1X PBS (pH 7.4, 4 °C). Then the cells were stained with 300nM DAPI solution for 5 minutes in the dark at room temperature. The cells were thoroughly rinsed thrice with ice cold 1X PBS (pH 7.4, 4 °C). Finally, the cells were viewed under a fluorescence microscope. Cells without nanoparticle treatment was used as control.

7.4 Results and Discussion

Initially, we have conducted the cellular uptake study based on nanoparticle exposure time, concentration, and free ligand concentration (competitive inhibition study). For these experiments we have incubated SW480 cancer cell line with nanoparticle samples of high yields. After optimizing nanoparticle exposure time and concentration we have conducted the cellular uptake study of targeted nanoparticles with SW480 (positive for both receptors), WI38 (positive for CD44 only) and Caco2 (positive for FR only) cell lines. We have also calculated the selectivity and distribution co-efficient of the targeted nanoparticles from their respective uptake studies. We ran the experiments in triplicates and presented the data as mean ± standard deviation. H:F:A is defined as the HA and FA molar ratio with respect to surface amine group.

7.4.1 Exposure concentration

Nanoparticle concentration is a significant factor that affects cellular targeting. Figure 49A shows the effect of targeted nanoparticle concentration on colon cancer (SW480) cell targeting after 4 hours of nanoparticle exposure. As can be seen from the qualitative images, cellular uptake of the nanoparticle formulations depended on nanoparticle exposure concentration. A weak green fluorescence signal was observed around the cell nucleus when 0.1 mg/ml of targeted nanoparticles were incubated with cells. In contrast, a strong green fluorescence signal was observed around the cell nucleus when 0.4 mg/ml of targeted nanoparticles were incubated with cells [162]. The number of nanoparticles internalized by the cells increased gradually with increasing exposure concentration which resulted in this strong green fluorescence. We observed similar trends at other nanoparticle formulation shown in Figure 49B.

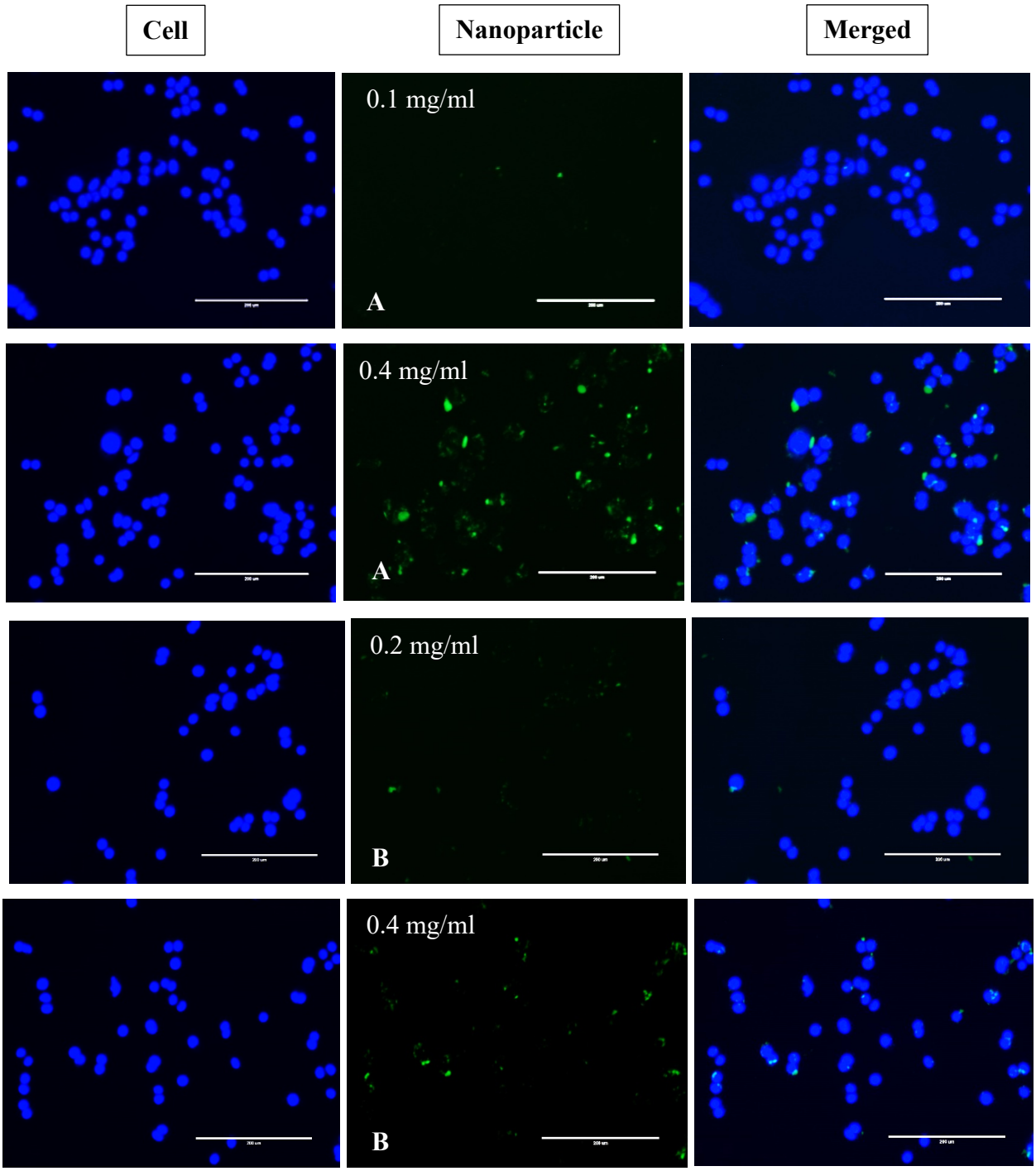

Figure 49 – Concentration dependent cellular uptake study of targeted silica nanoparticle on SW480 cell A) H:F:A=0.75:9:1 and B) H:F:A=1:9:1

Nanoparticle concentration dependent cellular uptake was further confirmed by quantitative study with fluorescence plate reader. Figure 50 shows the effect of targeted nanoparticle concentration on colon cancer (SW480) cell targeting after 4 hours of nanoparticle exposure. As can be seen

from the figure, cellular uptake of the nanoparticle formulations performed in a nanoparticle concentration dependent manner. All the nanoparticles showed lower cellular uptake at 0.1 mg/ml concentration. Cellular uptake increased gradually with increasing nanoparticle concentration. The uptake reached a plateau at 0.3 mg/ml concentration indicating about the uptake saturation of nanoparticles by the cells [212].

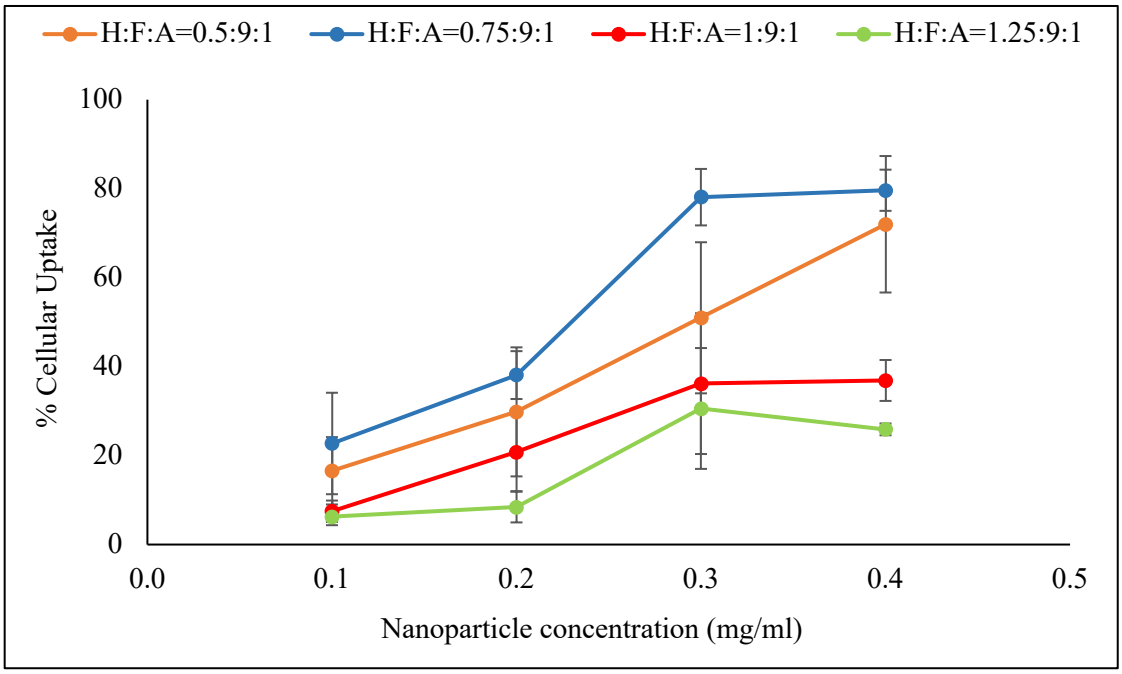

Figure 50 – Concentration dependent cellular uptake study of targeted silica nanoparticle on SW480 cell

7.4.2 Exposure time

Nanoparticle targeting of cell is also impacted by exposure time. Figure 51A shows the effect of targeted nanoparticle exposure time on colon cancer (SW480) cell targeting when incubated with 0.3 mg/ml of nanoparticle. As can be seen from the qualitative images, cellular uptake of the nanoparticle formulations depended on nanoparticle exposure time. A weak green fluorescence signal was observed around the cell nucleus when the targeted nanoparticles were incubated with cells for 1 hour. In contrast, a strong green fluorescence signal was observed around the cell nucleus when the targeted nanoparticles were incubated with cells for 4 hours [162]. The number of nanoparticles internalized by the cells increased gradually with increasing exposure time which

resulted in this strong green fluorescence. We observed similar trends at other nanoparticle formulation shown in Figure 51B.

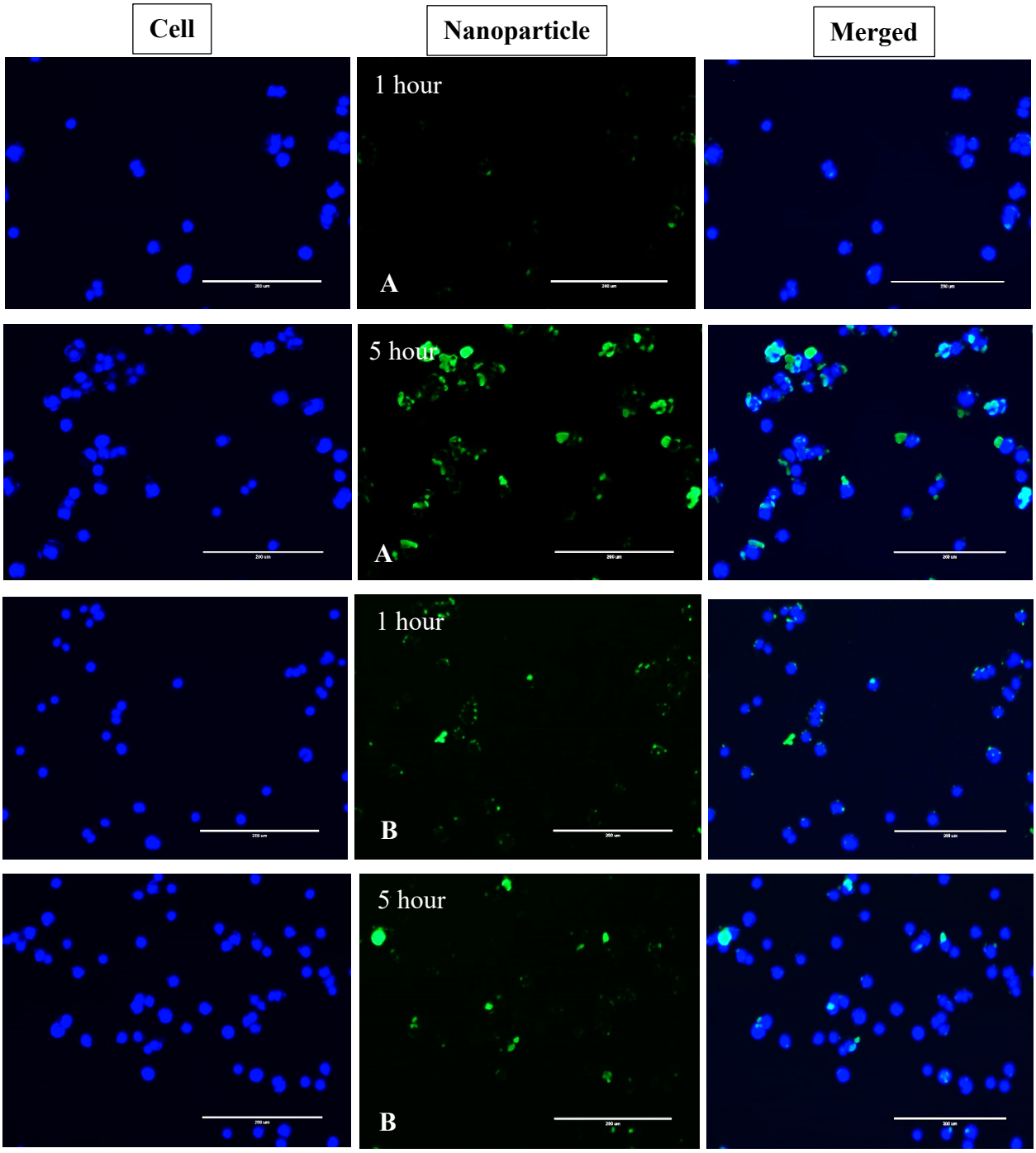

Figure 51 – Time dependent cellular uptake study of targeted silica nanoparticle on SW480 cell A) H:F:A=0.5:9:1 and B) H:F:A=1.25:9:1

Nanoparticle exposure time dependent cellular uptake was further confirmed by quantitative study with fluorescence plate reader. Figure 52 shows the effect of targeted nanoparticle exposure time on colon cancer (SW480) cell targeting when incubated with 0.3 mg/ml of nanoparticle. As can be seen from the figure, cellular uptake of the nanoparticle formulations performed in an exposure time dependent manner. All the nanoparticles showed lower cellular uptake when incubated for 0.5 hour. Cellular uptake increased gradually with increasing nanoparticle exposure time. The uptake reached a plateau at 3 hours suggesting about the uptake saturation of nanoparticles by the cells [213].

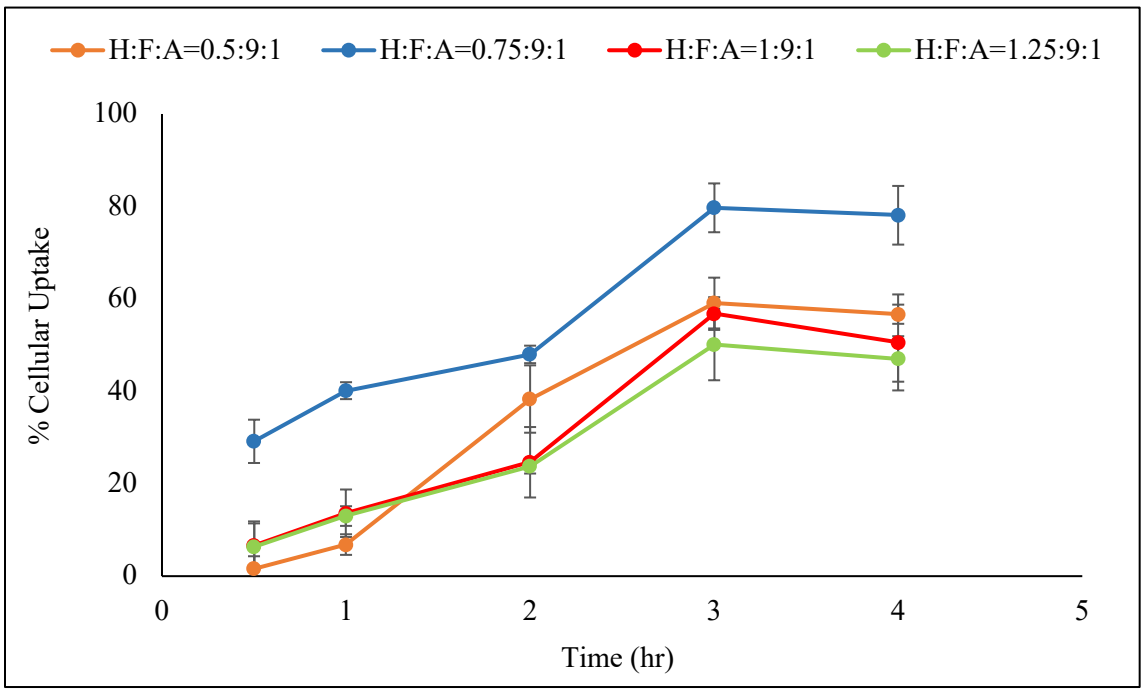

Figure 52 – Exposure time dependent cellular uptake study of targeted silica nanoparticle on SW480 cell

7.4.3 Competitive inhibition study

We have conducted the competitive inhibition study to confirm the interaction between HA-CD44 receptor and FA-folate receptor. Figure 53 shows the competitive inhibition study on colon cancer (SW480) cell targeting when pre-incubated with different concentration of free ligand mixture. As can be seen from the figure, pre-incubation of SW480 cells with free HA and FA mixture resulted in an inhibited amount of nanoparticle uptake by the cells compared to the non-incubated ones. One reason behind this phenomenon could be that the free HA and FA got effectively bound to

the CD44 and FR respectively, which blocked the receptors and prevented the nanoparticles from targeting the receptors. This lack of targeting eventually reduced the cellular uptake [18, 159, 172, 214]. The uptake decreased gradually with increasing free ligand concentration because with an enhancement of free ligand concentration, more receptors were getting blocked which prevented targeting. The uptake reached a plateau at 1 mg/ml indicating the possible uptake saturation of nanoparticles by the cells. These results confirmed that the uptake of the targeted nanoparticles was based on HA-CD44 receptor and FA- FR interactions.

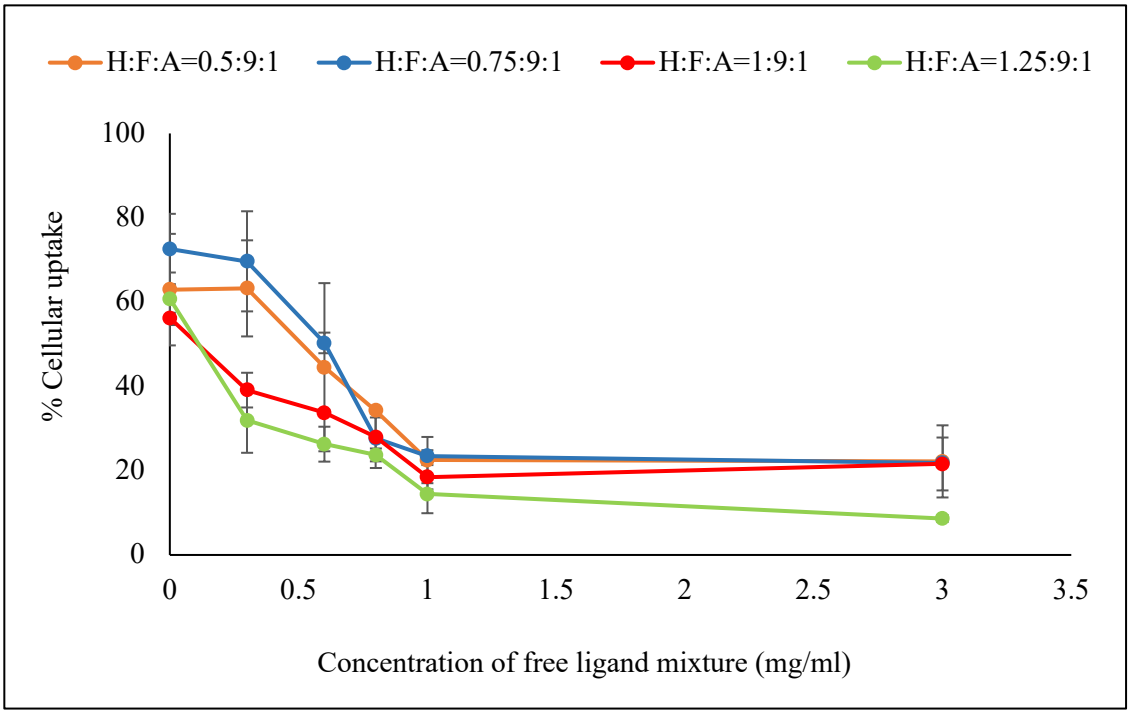

Figure 53 – Free ligand concentration dependent cellular uptake study of targeted silica nanoparticle on SW480 cell

7.4.4 Cellular uptake

Figure 54 shows the cellular uptake of the targeted silica nanoparticles on SW480 colon cancer cell line. As can be observed from the figure, for FA conjugated single targeted nanoparticles i.e. at H:A=0, increase in F:A molar ratio from 0 to 9 significantly increased the cellular uptake due to the presence of FR on SW480 cell line. For dual targeted nanoparticles i.e. at H:A≥0.5, increase in F:A molar ratio from 0 to 7 didn't significantly change the cellular uptake. The maximum cellular uptake was observed when F:A molar ratio was increased to 9. This trend can be correlated

to our FA conjugation data where increase in F:A molar ratio from 0 to 7 didn't significantly change the nanoparticle surface coverage by FA and the highest conjugation was achieved at F:A=9. This increase in cellular uptake could be due to FA-FR mediated endocytosis because SW480 cell line is positive for FR [189, 190]. Since SW480 cell line showed higher expression of CD44 compared to FR, different conjugation of HA on nanoparticle surface impacted the FA-FR interaction and subsequent cellular uptake. One interesting trend we observed here is that the cellular uptake increased when H:A molar ratio increased from 0 to 0.5 but the uptake decreased with further increase in H:A molar ratio up to 1.25. The reason behind the increased uptake with increasing ligand density could be HA-CD44 mediated endocytosis because SW480 cell line is also positive for CD44 [215, 216]. One possible reason behind the decreased uptake with further increase in ligand density could be steric crowding according to literature. Due to steric crowding, the conformation and reactivity of the ligands to effectively bind to the receptors get restricted with the addition of each ligand on the nanoparticle surface which eventually reduces the uptake [49, 184, 217, 218].

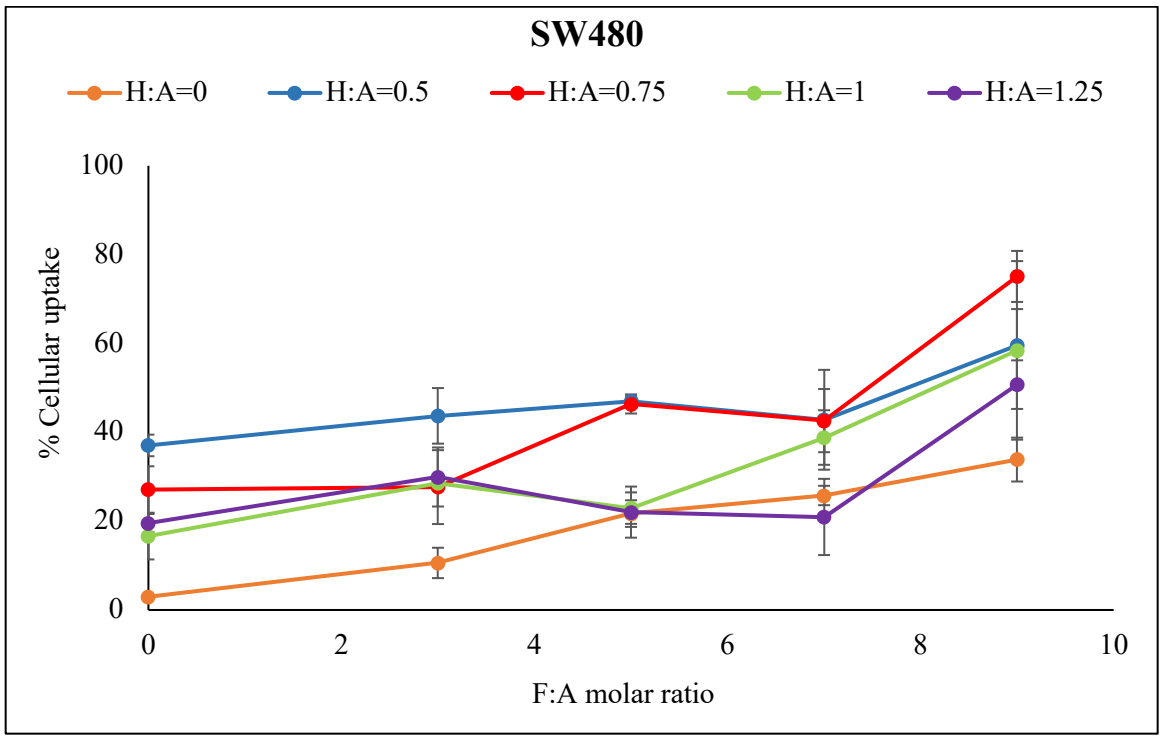

Figure 54 – Cellular uptake study of targeted silica nanoparticle on SW480 cell

Figure 55 shows the cellular uptake of the targeted silica nanoparticles on WI38 cell line. As can be observed from the figure, for FA conjugated single targeted nanoparticles i.e. at H:A=0, increase in F:A molar ratio from 0 to 3 increased the cellular uptake. However, further increase in F:A molar ratio from 3 to 9 didn't significantly change the cellular uptake which could be due to very poor expression of FR on WI38 cell line. At H:A≥0.5, increase in F:A molar ratio from 0 to 9 reduced the cellular uptake. This trend can be correlated to our HA conjugation data where increase in F:A molar ratio from 0 to 9 reduced the nanoparticle surface coverage by HA. Since WI38 cell line is positive for CD44, increase in F:A molar ratio reduced the subsequent HA-CD44 interaction. The minimum cellular uptake for H:A=0.5 reached at F:A=9, for H:A=0.75 at F:A=7, for H:A=1 at F:A=5 and for H:A=1.25 at F:A=3. The minimum cellular uptake for H:A≥0.75 continued up to F:A=9. Increase in H:A molar ratio reduces FA conjugation on nanoparticle surface and subsequent cellular uptake by FA-FR endocytosis. That is why the minimum cellular uptake for higher H:A molar ratio reached at lower FA conjugation. One interesting trend we observed here is that the cellular uptake increased when H:A molar ratio increased from 0 to 0.75 which could be due to HA-CD44 mediated endocytosis since WI38 cell line is positive for CD44 receptor [215, 216]. But the uptake decreased with further increase in H:A molar ratio up to 1.25 which could be due to steric crowding according to literature [49, 184, 217, 218].

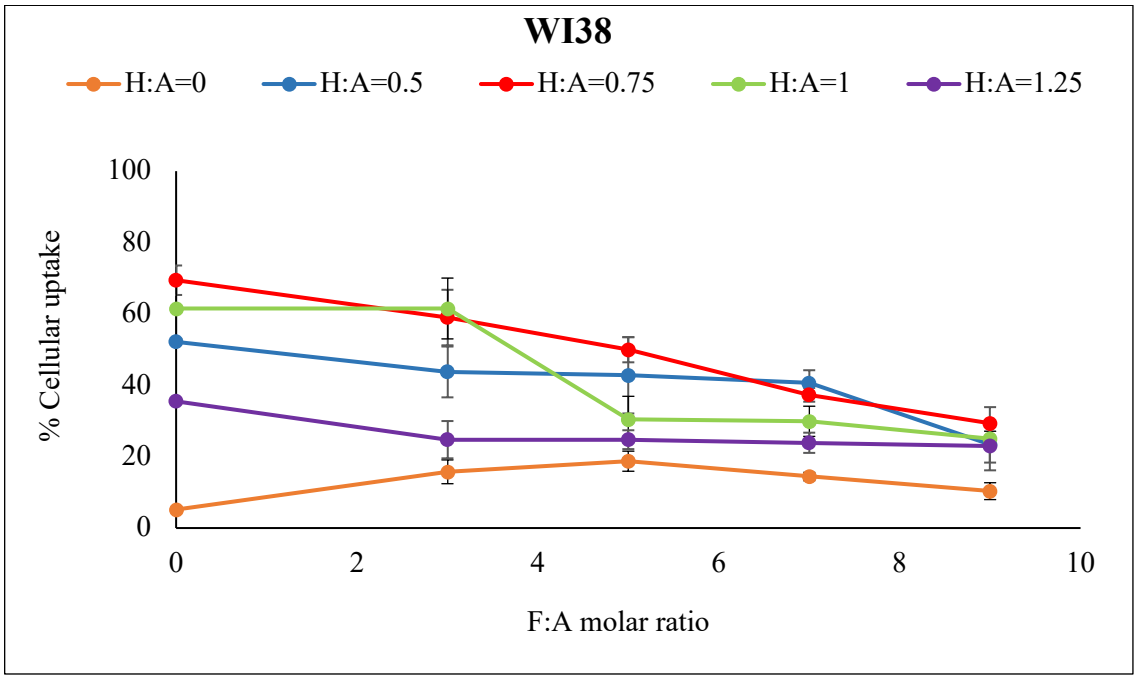

Figure 55 – Cellular uptake study of targeted silica nanoparticle on WI38 cell

Figure 56 shows the cellular uptake study of the targeted silica nanoparticles on Caco2 colon cancer cell line. As can be observed from the figure, at H:A≥0, increase in F:A molar ratio from 0 to 7 didn't significantly change the cellular uptake. The maximum cellular uptake was observed when F:A molar ratio was further increased to 9. Although, the maximum cellular uptake for H:A=0.5 and 1.25 reached at F:A=7, it was still maintained at F:A=9. This trend can be correlated to our FA conjugation data where increase in F:A molar ratio from 0 to 7 didn't significantly change the nanoparticle surface coverage by FA and the highest conjugation was achieved at F:A=9. This increase in cellular uptake could be due to FA-FR mediated endocytosis because Caco2 cell line is positive for FR [189, 190]. One interesting trend we observed here is that the cellular uptake increased when H:A molar ratio increased from 0 to 0.5. Although Caco2 cell line is positive for FR, ~10% cells showed positivity for CD44 in our flow cytometry study and the HA-CD44 mediated endocytosis could correspond to this uptake increase [215, 216]. However, the uptake decreased with further increase in H:A molar ratio up to 1.25. One possible reason can be the steric crowding according to literature [49, 184, 217, 218].

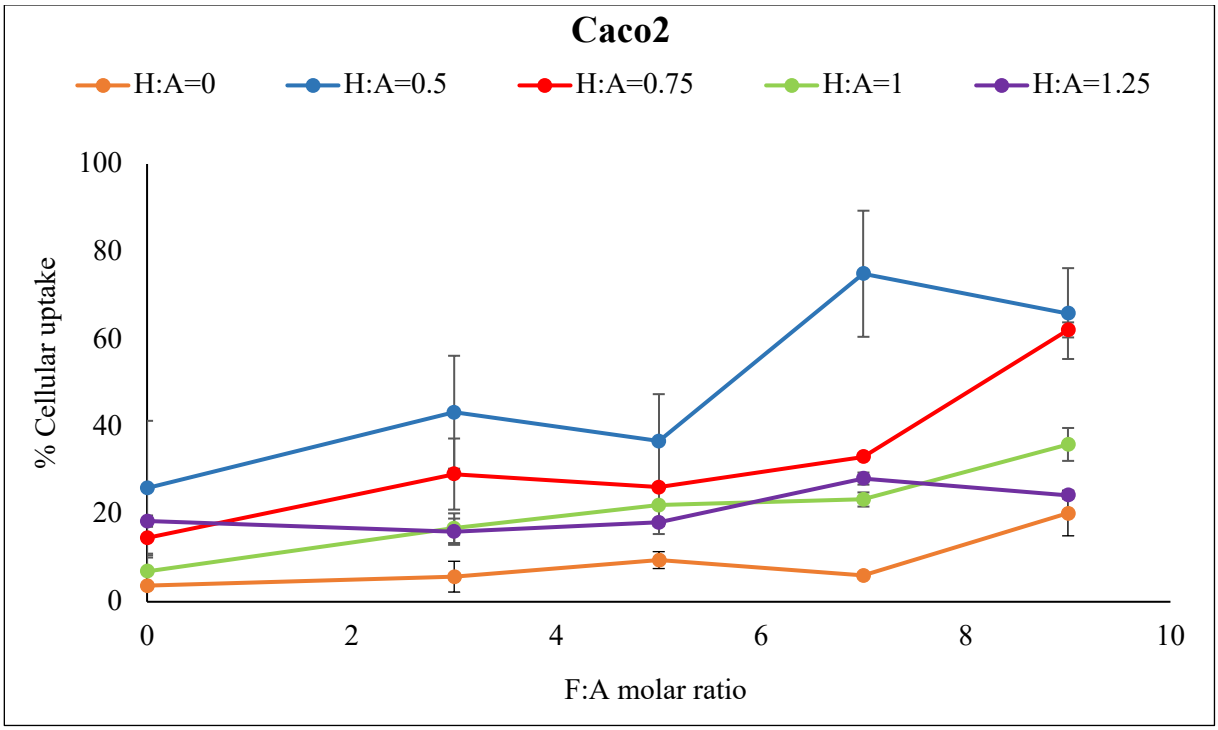

Figure 56 – Cellular uptake study of targeted silica nanoparticle on Caco2 cell

7.4.5 Selectivity

Figure 57 shows the selectivity of the targeted silica nanoparticles by comparison of the cancer cell with both CD44 and FR available (SW480) to the control cell with just CD44 available (WI38). As can be seen from the figure, the targeted nanoparticles showed higher selectivity with an increase in F:A molar ratio. With an enhancement of FA conjugation on nanoparticle surface the nanoparticles lead to target the cancer cell while limitedly target the control cell due to very low expression of FR on control cell. For H:A≥0, the highest selectivity was achieved at F:A=9. The targeted nanoparticles showed selectivity reduction with an increase in H:A molar ratio from 0 to 1.25. With an enhancement of HA conjugation on nanoparticle surface the nanoparticles lead to target both the cancer and control cells due to presence of CD44 on both types of cells. For F:A≥0, the highest selectivity was achieved at H:A=0.

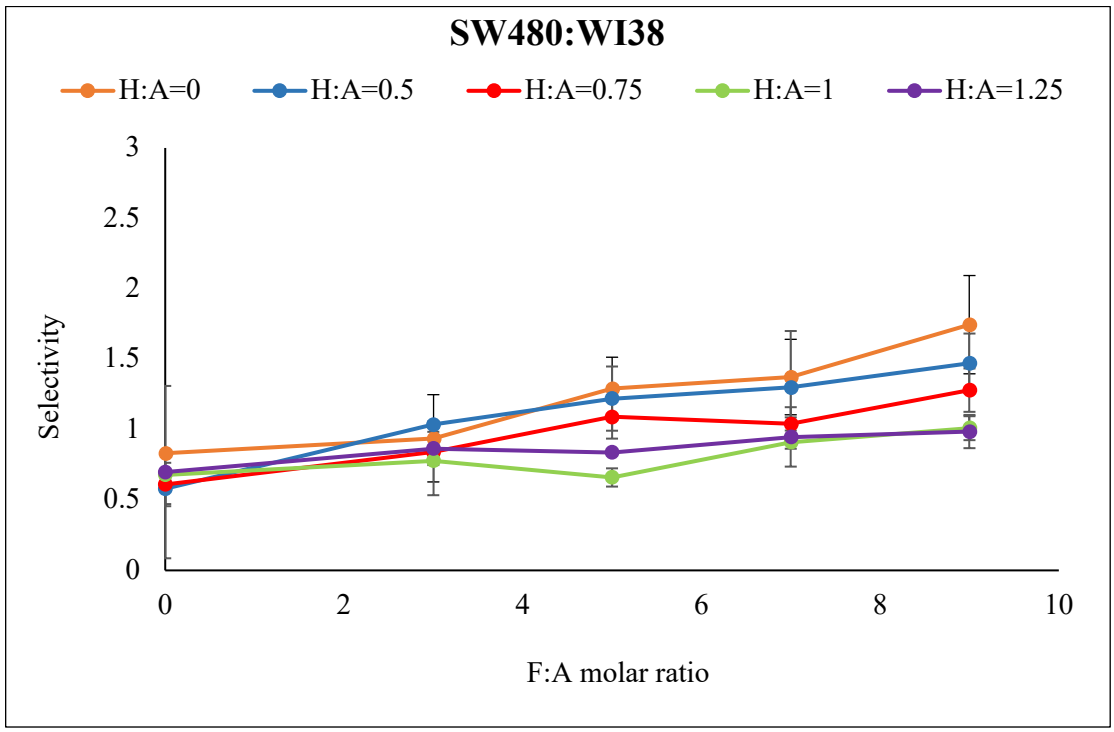

Figure 57 – Selectivity of targeted silica nanoparticle (SW480:WI38)

Figure 58 shows the selectivity of the targeted silica nanoparticles by comparison of the cancer cell with both CD44 and FR available (SW480) to the control cell with just FR available (Caco2). As can be seen from the figure, at H:A=0, the targeted nanoparticles showed higher selectivity with an increase in F:A molar ratio. With an enhancement of FA conjugation on nanoparticle

surface the nanoparticles lead to target both the cancer and control cells due to presence of FR on both types of cells. But the selectivity got increased due to the difference in relative change of uptake between the 2 types of cells. For H:A=0, the highest selectivity was achieved at F:A=9.At H:A≥0.5, the targeted nanoparticles showed selectivity reduction with an increase in F:A molar ratio. With an enhancement of FA conjugation on the nanoparticle surface the nanoparticles lead to target both the cancer and control cells due to expression of FR by both types of cells. But the selectivity got reduced due to the difference in relative change of uptake between the 2 types of cells. For H:A≥0.5, the highest selectivity was achieved at F:A=0. The targeted nanoparticles exhibited selectivity reduction with an increase in H:A molar ratio from 0.5 to 1.25. With an enhancement of HA conjugation on nanoparticle surface the nanoparticles lead to target the cancer cell while limitedly target the control cell due to very low expression of CD44 on control cell. For H:A≥0.5, the highest selectivity was achieved at H:A=0.5.

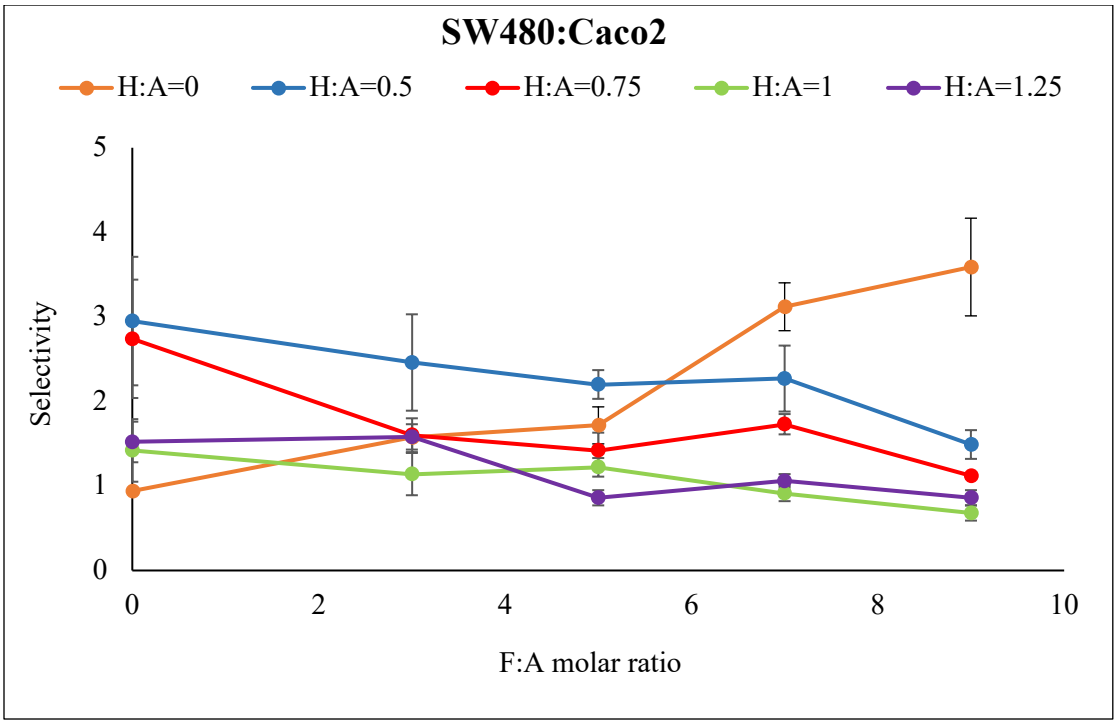

Figure 58 – Selectivity of targeted silica nanoparticle (SW480:Caco2)

7.4.6 Distribution co-efficient

Figure 59 shows the distribution co-efficient of the targeted silica nanoparticles on SW480 colon cancer cell line. As can be observed from the figure, at H:A≥0.75, increase in F:A molar ratio from 0 to 7 didn't significantly change the nanoparticle distribution. The maximum distribution was observed when F:A molar ratio was increased to 9. This trend can be correlated to our FA conjugation data where increase in F:A molar ratio from 0 to 7 didn't significantly change the nanoparticle surface coverage by FA and the highest conjugation was achieved at F:A=9. This increase in distribution could be due to FA-FR mediated endocytosis because SW480 cell line is positive for FR [189, 190]. Since SW480 cell line showed higher expression of CD44 compared to FR, different conjugation of HA on nanoparticle surface impacted the FA-FR interaction and subsequent nanoparticle distribution. The distribution co-efficient increased when H:A molar ratio increased from 0 to 0.5 but the co-efficient decreased with further increase in H:A molar ratio up to 1.25. While the reason behind increased distribution with increasing ligand density could be HA-CD44 mediated endocytosis because SW480 cell line is positive for CD44 also [215, 216], the reason behind decreased distribution with further increase in ligand density could be steric crowding based on literature [49, 184, 217, 218].

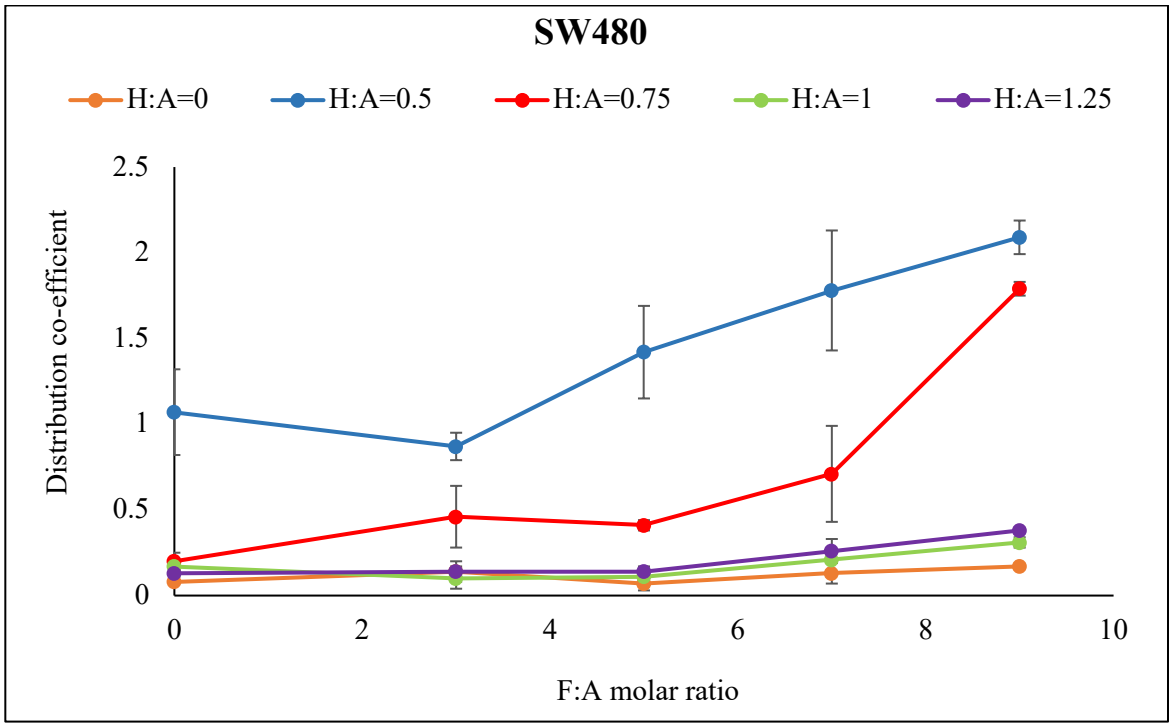

Figure 59 – Distribution co-efficient of targeted silica nanoparticle on SW480 cell

Figure 60 shows the distribution co-efficient of the targeted silica nanoparticles on WI38 cell line. As can be observed from the figure, for FA conjugated single targeted nanoparticles i.e. at H:A=0, increase in F:A molar ratio from 0 to 3 increased the nanoparticle distribution to cell. However, further increase in F:A molar ratio from 3 to 9 didn't have any significant impact on the distribution co-efficient due to very poor expression of FR on WI38 cell line. This trend can be correlated to our HA conjugation data where increase in F:A molar ratio from 0 to 9 reduced the nanoparticle surface coverage by HA. Since WI38 cell line is positive for CD44, increase in F:A molar ratio reduced the subsequent HA-CD44 interaction. The minimum distribution co-efficient for H:A=0.5 reached at F:A=9, for H:A=0.75 at F:A=7, for H:A=1 at F:A=5 and for H:A=1.25 at F:A=3. The minimum distribution co-efficient for H:A≥0.75 continued up to F:A=9. Increase in H:A molar ratio reduced the FA conjugation on nanoparticle surface and subsequent cellular uptake by FA-FR endocytosis. That is why the minimum distribution co-efficient for higher H:A molar ratio reached at lower FA conjugation. One interesting trend we observed here is that the distribution co-efficient increased when H:A molar ratio increased from 0 to 0.75 which could be due to HA-CD44 mediated endocytosis since WI38 cell line showed positivity for CD44 receptor [215, 216]. But the distribution co-efficient decreased with further increase in H:A molar ratio up to 1.25 which could be due to steric crowding based on literature [49, 184, 217, 218].

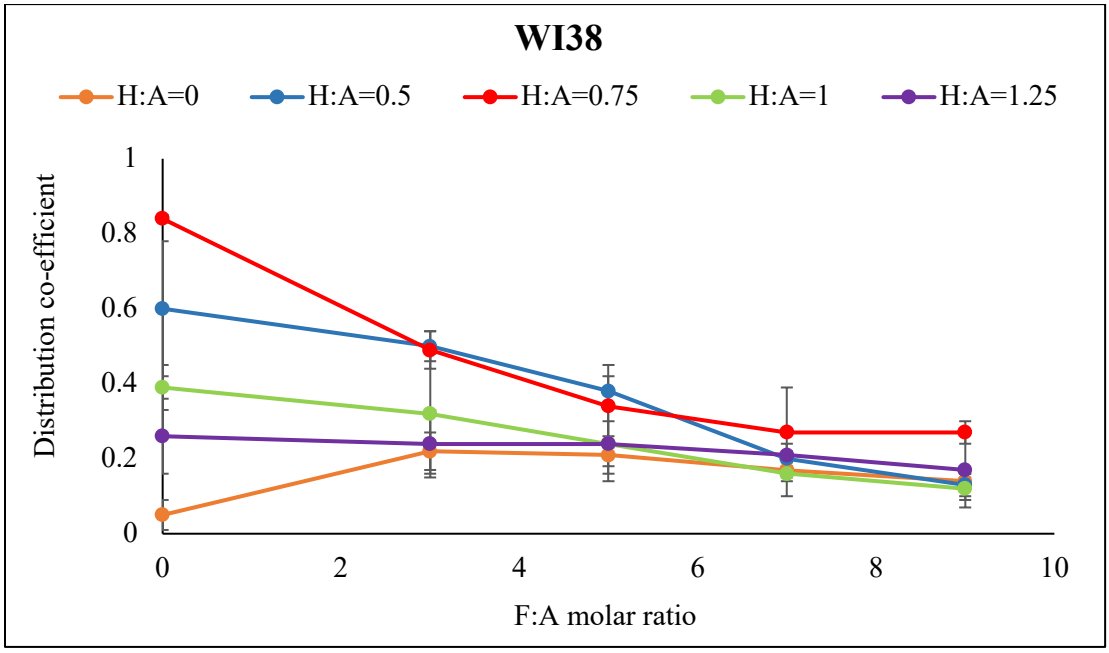

Figure 60 – Distribution co-efficient of targeted silica nanoparticle on WI38 cell

Figure 61 shows the distribution co-efficient of the targeted silica nanoparticles on Caco2 colon cancer cell line. As can be observed from the figure, at H:A=0, increase in F:A molar ratio from 0 to 3 increased the distribution co-efficient. However, further increase in F:A molar ratio from 3 to 9 didn't have any significant impact on the distribution co-efficient. At H:A≥0.5, increase in F:A molar ratio increased the distribution co-efficient and reached a plateau at F:A=7. Since Caco2 cell line is positive for FR, increase in F:A molar ratio increased the nanoparticle distribution to cell due to FA-FR mediated endocytosis [189, 190]. The distribution co-efficient increased when H:A molar ratio increased from 0 to 0.5 which could be due to the HA-CD44 mediated endocytosis since ~10% of Caco2 cells showed positivity for CD44 in our flow cytometry study [215, 216]. However, the distribution decreased with further increase in H:A molar ratio up to 1.25 which could be due to steric crowding according to literature [49, 184, 217, 218].

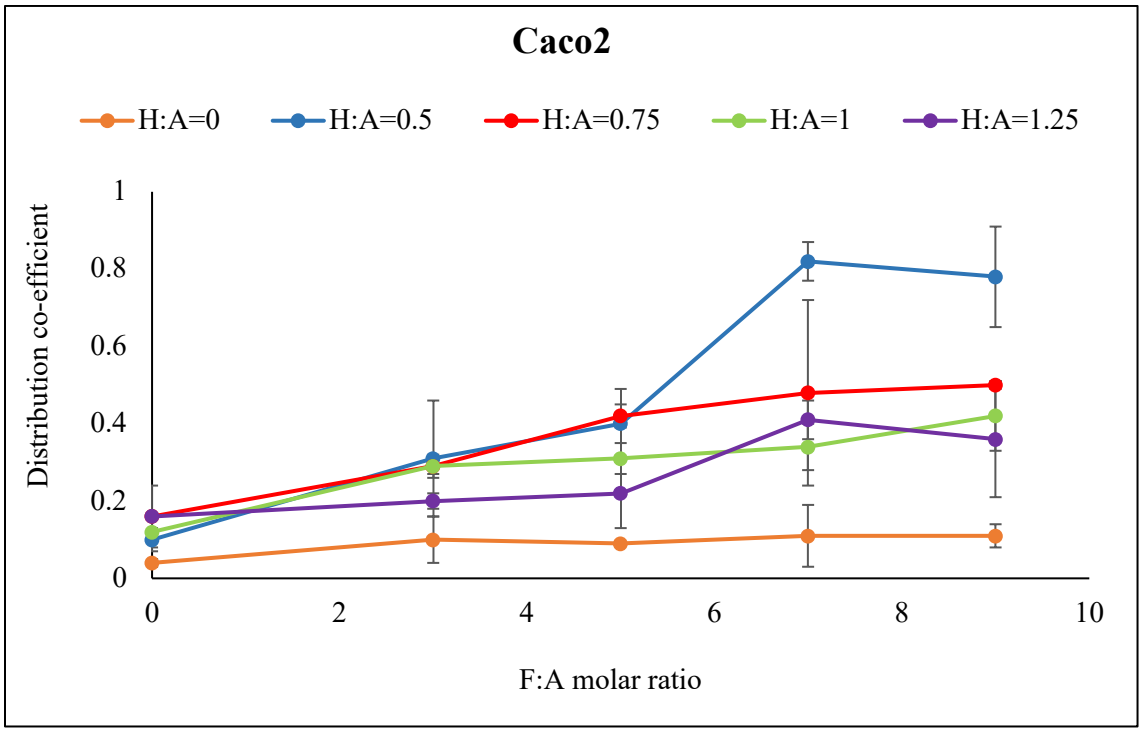

Figure 61 – Distribution co-efficient of targeted silica nanoparticle on Caco2 cell

7.5 Summary

We have conducted the cellular uptake study using SW480 (positive for both receptors), WI38 (positive for CD44) and Caco2 (positive for FR) cells. Cellular uptake of nanoparticles showed to function in an exposure time and concentration dependent manner. Competitive inhibition study confirmed that the uptake of the targeted nanoparticles was based on HA-CD44 and FA-FR interactions.

WI38 cells exhibited higher cellular uptake of HA conjugated single targeted nanoparticles (i.e. F:A=0) followed by SW480 and Caco2 cells since WI38 cells showed higher expression of CD44 receptor compared to SW480 and Caco2 cell lines. Although SW480 and Caco2 cells showed similar expression level of FR, SW480 cells exhibited higher cellular uptake of FA conjugated single targeted nanoparticles (i.e. H:A=0) followed by WI38 and Caco2 cells.

Based on FA conjugation, the highest cellular uptake was achieved at F:A=9 for SW480 and Caco2 cells and at F:A=0 for WI38 cell. The highest selectivity was achieved at F:A=9 for both SW480:WI38 and SW480:Caco2 cells. Based on HA conjugation, the highest cellular uptake was achieved at H:A=0.5-0.75 for SW480 cell, at H:A=0.75 for WI38 cell and at H:A=0.5 for Caco2 cell. The highest selectivity was achieved at H:A=0 for both SW480:WI38 and SW480:Caco2 cells.

Throughout the cellular uptake study we observed that increase in FA conjugation didn't have a significant impact on nanoparticle uptake increase at F:A≤7 and the highest cellular uptake was achieved at F:A=9 for FR positive cells which is the highest examined molar ratio. Since FA is small in size (MW=436g/mol), little increase in F:A molar ratio slightly increased the FA conjugation on nanoparticle surface which could correspond to this insignificant increase in nanoparticle uptake. On the other hand, increase in HA conjugation significantly impacted the nanoparticle uptake. For CD44 positive cells, the cellular uptake increased with increasing HA conjugation but started declining beyond a certain point. So we concluded that the optimum H:A molar ratio for targeted nanoparticles was 0.5-0.75. For our experiments, we used HA of large size (MW=8000g/mol). So, increase in H:A molar ratio increased HA conjugation on nanoparticle surface which could correspond to the significant impact on nanoparticle uptake.

Chapter 8: Future directions

Moving forward the dual targeted nanoparticles developed in this project can be used as a drug or imaging agent delivery vehicle. However, further modification of this model system is required to improve targeting. This chapter initially focuses on the optimization of the model system to improve targeting and then possible applications of the system.

8.1 Optimization of nanoparticles to improve targeting

It was observed that the dual targeted nanoparticles exhibited higher cellular uptake compared to the non-targeted and single targeted ones for receptor positive cells. There are several parameters that can help to improve the targeting which include ligand length, density and addition of linker.

The size or length or MW of the ligand is an important factor that impacts cellular targeting. There is a minimum threshold size of the ligand necessary to start cellular targeting. Higher MW of the ligand results in more cellular uptake of the nanoparticle compared to lower MW of the ligand which could correspond to the higher binding affinity of the ligand to its receptor. Also, longer length of the ligand provides more accessibility of the ligand to its receptor to cause multivalent binding [22, 154]. For dual ligand attachment, it is necessary to have similarity between the length of the two ligands. If one ligand is much longer than the other, then the access length can mask the targeting ability of the other ligand. The longer ligand can also fold itself and lose its ability to target [49].

Optimization of ligand density on nanoparticle surface has a great impact on cellular targeting. There is a minimum threshold density of the ligand necessary to start cellular targeting [22]. Higher ligand density on nanoparticle surface results in more cellular uptake of the nanoparticle compared to lower ligand density. However, after a certain ligand density the cellular uptake may reach a plateau or start declining. That certain ligand density is called ‘maximum density’. The maximum ligand density at plateau may correspond to the saturation of ligand-receptor binding. The decrease in cellular uptake after maximum ligand density may correspond to steric crowding. So, it is very important to optimize ligand density to maximize cellular uptake. Throughout the cellular uptake study we observed that increase in HA conjugation significantly impacted the nanoparticle uptake. For CD44 positive cells, the cellular uptake increased with increasing HA conjugation but started

declining after a certain conjugation. So, within our tested H:A molar ratio range, we achieved optimum ligand density at maximum which was H:A=0.5-0.75. On the other hand, increase in FA conjugation didn't have significant impact on nanoparticle uptake increase until F:A=7. The highest cellular uptake was achieved at F:A=9 for FR positive cells which is the highest examined molar ratio. Within our tested F:A molar ratio range, saturation of uptake wasn't achieved which could be achieved at F:A≥9.

However, increased ligand density and multivalency can promote protein adsorption on the nanoparticle surface which can lead to non-specific uptake by Reticuloendothelial System [26, 38]. So, nanoparticles with high ligand density may get cleared from the body before even reaching the target site. In order for a targeted nanoparticle to act as a delivery vehicle, it must present in the circulation long enough to reach the target site. Nanoparticles are covered with a hydrophilic coating like PEG which increases the circulation time by avoiding interaction with the proteins and subsequent non-specific uptake [142-146]. Normally, ligands are conjugated on nanoparticle surface using a PEG spacer which extends the ligand from the nanoparticle surface and makes it accessible to the receptors. However, higher ligand density may shield the PEG effect and make the nanoparticle susceptible to non-specific uptake [26, 29, 219]. The PEG spacer length needs to be similar to that of the surrounding ones. If the PEG spacer length is longer than the surrounding ones, the excess length can fold and cover the ligand [49, 219]. If both the PEG and ligand are attached on the nanoparticle surface then there is a need to optimize their length and density. Longer length and higher density of PEG can mask the targeting effect of the ligand [49]. On the other hand, longer length and higher density of ligand may shield the PEG effect. So, there is a need to fine tune the interplay between PEG and ligand properties in order to maximize targeting while minimizing non-specific uptake.

8.2 Optimization of off-target cell to improve selectivity

Cell surface receptor expression plays a key role in cellular uptake of the nanoparticles. An ideal target should have a high expression level on the cancer cell surface for the diagnostic and therapeutic application of the cancer and it should also be highly specific to that cancer [184]. Targeting efficiency has been reported to be dependent on the cell surface receptor density and higher receptor density correlates with higher nanoparticles uptake [22]. In this project we have used 1 target cell with positivity for both receptors (SW480) and 2 off-target cells - with positivity

of either receptor (WI38 with CD44 positivity and Caco2 with FR positivity). For these 2 types of off-target cells we have got different formulations that achieved maximum selectivity within our tested ligand density range. However, an ideal off-target cell for maximum selectivity would have been the one which is negative for both receptors. Although some of the literatures have identified human breast cancer cell (MCF-7) as CD44 and FR positive [153, 220-222], others have concluded it as negative for both receptors [154, 159, 177]. There is also debate about CD44 and FR positivity of human lung adenocarcinoma cell line (A549) in the literature [154, 163, 223]. Conducting flow cytometry study for all the cells to identify an ideal off-target one would have been a very time consuming and expensive study. So, we conducted the flow cytometry study only for the normal and colon cancer cells available in our laboratory.

8.3 Applications of targeted nanoparticles

The targeted nanoparticles developed in this project can be applied to tissue slides of actual tumor patients. In chapter 6, we have evaluated the expression of CD44 and FR using IHC staining on three different grades of NET tissues. Qualitative analysis proved the existence of CD44 and FR in NETs. Semi-quantitative analysis proved the dependence of receptor expression on tumor grade. So, moving forward the dual targeted nanoparticles developed in this project have the potential to be used in IHC staining to target tumor tissue of actual patients. However, i.e. staining the receptors with antibodies first may block the receptors to be targeted by nanoparticles. Also, targeting the receptors with nanoparticles first may have impact on receptor staining. So, optimization of the IHC protocol is required to achieve desired result.

The targeted nanoparticles can also be translated to in vivo and ex vivo experiments to evaluate the targeting efficacy and bio-distribution of the system respectively. For this study, BALB/c mice nude mice can be used to create SW480 tumor transplanted mouse model. The tumor volumes will be measured at predetermined intervals using a digital caliper. When the tumor volume will reach approximately 100 mm^3, free Cy5.5, HA-Silica/Cy5.5, FA-Silica/Cy5.5 and HA-FA-Silica/Cy5.5 will be injected into the tail veins of mice. An in vivo imaging system (IVIS) will be used to take in vivo fluorescence images at 1, 3, 6, 12 and 24 hours after injection. The tumor targeting efficacy of the nanoparticles will be evaluated by comparing the fluorescence intensity in the tumor region. The mice will be sacrificed 24 hour after injection. The tumor and other organs like liver, spleen,

lung and kidney will be collected to take fluorescence images. It is expected that the tumor fluorescence intensity of the dual targeted silica nanoparticle will be significantly stronger than that of the free dye and single targeted silica nanoparticles in a time dependent manner indicating the increased in vivo tumor targeting ability of the model system. Successful completion of the in vivo experiment can make this model system potential for clinical translation.

Chapter 9: Conclusion

The goal of this project was to study the impact of nanoparticle dual ligand density on targeting of cells with different biomarker expression. To achieve this goal we have developed silica nanoparticles conjugated with hyaluronic acid and folic acid to target colon cancer specific CD44 and folate receptors respectively.

In chapter 3, we have discussed the synthesis and characterization of HA and FA conjugated targeted nanoparticles from fluorescently tagged silica nanoparticles. The fluorescamine assay and fluorescence measurement ensured the successful attachment of amine groups and FITC respectively on the silica nanoparticle surface. The targeted nanoparticles showed moderate size distribution, reduced protein adsorption and excellent fluorescence stability. The CTAB turbidimetric method and spectrophotometric method confirmed the successful conjugation of HA and FA respectively on the silica nanoparticle surface which are useful for cellular targeting.

In chapter 4, we have discussed the cytotoxicity of the targeted nanoparticles by incubating them with HCT116 and CHO cells from 24 to 72 hours at doses range of 0.1-100 μg/ml. While HCT116 cells showed time and concentration dependent cell viability, the targeted nanoparticles had no impact on CHO cell viability. However, cell viability for both of the cells remained ~70% at the maximum time and concentration tested which is an indication of safe material according to literature.

In chapter 5, we have evaluated the expression of CD44 and FR using Flow Cytometer on four different colon cancer cell lines and three different normal cell lines available in the laboratory. All the cancer and normal cells except Caco2 and WI38 expressed both of the receptors. WI38 expressed only CD44 and Caco2 expressed only folate receptors. The expression level of each of the receptor for SW480 cell line was higher compared to other cell lines. Based on this study, we have decided to use SW480 cell line as positive for both receptors, WI38 cell line as positive for only CD44 receptor and Caco2 cell line as positive for only folate receptor in the cellular targeting experiment.

In chapter 6, we have evaluated the expression of CD44 and FR using IHC staining on three different grades of NET tissues. Qualitative analysis showed us the existence of CD44 and FR in

NETs with higher expression of CD44 compared to FR. Semi-quantitative analysis from ImageJ showed us the dependence of receptor expression on tumor grade with higher percentage of area positivity for CD44 compared to FR.

In chapter 7, we have discussed the cellular uptake study using SW480 (positive for both receptors), WI38 (positive for CD44) and Caco2 (positive for FR) cells. Cellular uptake of nanoparticles showed to function in an exposure time and concentration dependent manner. Competitive inhibition study confirmed that the uptake of the targeted nanoparticles was based on HA-CD44 and FA-FR interactions. Based on FA conjugation, the highest cellular uptake was achieved at F:A=9 for SW480 and Caco2 cells and at F:A=0 for WI38 cell. The highest selectivity was achieved at F:A=9 for both SW480:WI38 and SW480:Caco2 cells. Based on HA conjugation, the highest cellular uptake was achieved at H:A=0.5-0.75 for SW480 cell, at H:A=0.75 for WI38 cell and at H:A=0.5 for Caco2 cell. The highest selectivity was achieved at H:A=0 for both SW480:WI38 and SW480:Caco2 cells. Due to the variation in receptor expression by the studied cell lines, we got different formulations that achieved maximum uptake and selectivity within our tested ligand density range.

One of the main accomplishments of this project is to present a novel synthesis approach for the synthesis of HA and FA conjugated dual targeted nanoparticle. Several articles have reported sequential approach for attaching these two ligands on nanoparticle surface [24, 163, 164, 224] but to the best of our knowledge, this project presents the first simultaneous approach for these dual ligand conjugation. Additionally, as far as we know there is no report of targeting colon cancer cells with this dual targeted model system. There are two articles that have reported the increase in cancer cellular uptake of nanoparticles as a function of HA and FA single ligand density [22, 225]. In this project, we have synthesized various dual ligand formulations with HA and FA to evaluate the impact of these dual ligand density on targeting of cells with different biomarker expression. We have hypothesized that, CD44 and folate dual receptor targeting of colon cancer cells will increase the cancer cellular uptake of nanoparticles as a function of surface ligand density. In addition to that, dual receptor targeted nanoparticles will internalize more nanoparticles into the cancer cells compared to the single receptor targeted nanoparticles. We have observed that cellular uptake depends on ligand length, density and number of ligand type. Cellular uptake increases as a function of ligand density and beyond an intermediate density, it starts declining.

Also, dual targeted nanoparticles showed higher cellular uptake compared to single targeted nanoparticles for dual receptor positive cell. Since we have used cell lines with different expression of the two biomarkers, we have achieved different formulations for maximum uptake and selectivity which indicates the dependency of cellular targeting also on biomarker expression.

The targeted nanoparticle formulations can be used in several future biomedical applications. The tumor targeting capability of the nanoparticle can be used to deliver chemotherapeutic drugs and imaging agents at the cancer site while sparing normal cells. Overall, this novel nanoparticle formulation will combine the benefits of dual targeting and enhanced ligand coverage to be used for theranostic applications.

Chapter 10: Reference

1. *Colorectal Cancer: Statistics*. November, 2018; Available from: https://www.cancer.net/cancer-types/colorectal-cancer/statistics.
2. Hamzehzadeh, L., et al., *New approaches to use Nanoparticles for treatment of colorectal cancer; a brief review.* Nanomedicine Research Journal, 2016. **1**(2): p. 59-68.
3. You, X., et al., *Polymeric nanoparticles for colon cancer therapy: overview and perspectives.* Journal of Materials Chemistry B, 2016. **4**(48): p. 7779-7792.
4. Chandran, S.P., et al., *Nano drug delivery strategy of 5-fluorouracil for the treatment of colorectal cancer.* Journal of Cancer Research and Practice, 2017. **4**(2): p. 45-48.
5. Banerjee, A., et al., *Strategies for targeted drug delivery in treatment of colon cancer: current trends and future perspectives.* Drug discovery today, 2017. **22**(8): p. 1224-1232.
6. Jaferian, S., B. Negahdari, and A. Eatemadi, *Colon cancer targeting using conjugates biomaterial 5-flurouracil.* Biomedicine & Pharmacotherapy, 2016. **84**: p. 780-788.
7. Kotelevets, L., et al., *Nanotechnologies for the treatment of colon cancer: From old drugs to new hope.* International journal of pharmaceutics, 2016. **514**(1): p. 24-40.
8. Cisterna, B.A., et al., *Targeted nanoparticles for colorectal cancer.* Nanomedicine, 2016. **11**(18): p. 2443-2456.
9. Peer, D., et al., *Nanocarriers as an emerging platform for cancer therapy.* Nature nanotechnology, 2007. **2**(12): p. 751.
10. Shi, M., et al., *Doxorubicin-conjugated immuno-nanoparticles for intracellular anticancer drug delivery.* Advanced functional materials, 2009. **19**(11): p. 1689-1696.
11. Danhier, F., O. Feron, and V. Préat, *To exploit the tumor microenvironment: passive and active tumor targeting of nanocarriers for anti-cancer drug delivery.* Journal of controlled release, 2010. **148**(2): p. 135-146.
12. Dong, Z., et al., *Nanoparticles for Colorectal Cancer Targeted Drug Delivery and MR Imaging: Current Situation and Perspectives.* Current cancer drug targets, 2016. **16**(6): p. 536-550.
13. Bazak, R., et al., *Cancer active targeting by nanoparticles: a comprehensive review of literature.* Journal of cancer research and clinical oncology, 2015. **141**(5): p. 769-784.

14. Jokerst, J.V. and S.S. Gambhir, *Molecular imaging with theranostic nanoparticles.* Accounts of chemical research, 2011. **44**(10): p. 1050-1060.
15. Egusquiaguirre, S.P., et al., *Nanoparticle delivery systems for cancer therapy: advances in clinical and preclinical research.* Clinical and Translational Oncology, 2012. **14**(2): p. 83-93.
16. An, J., et al., *Design and 3D printing of scaffolds and tissues.* Engineering, 2015. **1**(2): p. 261-268.
17. Zhang, Y., et al., *Redox-Responsive and Dual-Targeting Hyaluronic Acid–Methotrexate Prodrug Self-Assembling Nanoparticles for Enhancing Intracellular Drug Self-Delivery.* Molecular pharmaceutics, 2019. **16**(7): p. 3133-3144.
18. Wang, T., et al., *Hyaluronic acid-coated chitosan nanoparticles induce ROS-mediated tumor cell apoptosis and enhance antitumor efficiency by targeted drug delivery via CD44.* Journal of nanobiotechnology, 2017. **15**(1): p. 7.
19. Alvarez-Berrios, M.P. and J.L. Vivero-Escoto, *In vitro evaluation of folic acid-conjugated redox-responsive mesoporous silica nanoparticles for the delivery of cisplatin.* International journal of nanomedicine, 2016. **11**: p. 6251.
20. Zhang, M., et al., *A hyaluronidase responsive nanoparticle-based drug delivery system for targeting colon cancer cells.* Cancer research, 2016: p. canres. 1681.2016.
21. Rosenholm, J.M., et al., *Cancer-cell-specific induction of apoptosis using mesoporous silica nanoparticles as drug-delivery vectors.* Small, 2010. **6**(11): p. 1234-1241.
22. Qhattal, H.S.S. and X. Liu, *Characterization of CD44-mediated cancer cell uptake and intracellular distribution of hyaluronan-grafted liposomes.* Molecular pharmaceutics, 2011. **8**(4): p. 1233-1246.
23. Qu, W., et al., *Folic acid-conjugated mesoporous silica nanoparticles for enhanced therapeutic efficacy of topotecan in retina cancers.* International Journal of Nanomedicine, 2018. **13**: p. 4379.
24. Lee, J.-Y., et al., *Dual CD44 and folate receptor-targeted nanoparticles for cancer diagnosis and anticancer drug delivery.* Journal of controlled release, 2016. **236**: p. 38-46.
25. Li, X., et al., *Enhancement of cell recognition in vitro by dual-ligand cancer targeting gold nanoparticles.* Biomaterials, 2011. **32**(10): p. 2540-2545.

26. Jahan, S.T., et al., *Targeted therapeutic nanoparticles: an immense promise to fight against cancer.* Journal of drug delivery, 2017. **2017**.
27. Jones, A. and A.L. Harris, *New developments in angiogenesis: a major mechanism for tumor growth and target for therapy.* The cancer journal from Scientific American, 1998. **4**(4): p. 209-217.
28. Prabhu, R.H., V.B. Patravale, and M.D. Joshi, *Polymeric nanoparticles for targeted treatment in oncology: current insights.* International journal of nanomedicine, 2015. **10**: p. 1001.
29. Karra, N. and S. Benita, *The ligand nanoparticle conjugation approach for targeted cancer therapy.* Current drug metabolism, 2012. **13**(1): p. 22-41.
30. Yu, M.K., J. Park, and S. Jon, *Targeting strategies for multifunctional nanoparticles in cancer imaging and therapy.* Theranostics, 2012. **2**(1): p. 3.
31. ud Din, F., et al., *Effective use of nanocarriers as drug delivery systems for the treatment of selected tumors.* International journal of nanomedicine, 2017. **12**: p. 7291.
32. Toporkiewicz, M., et al., *Toward a magic or imaginary bullet? Ligands for drug targeting to cancer cells: principles, hopes, and challenges.* International journal of nanomedicine, 2015. **10**: p. 1399.
33. Hobbs, S.K., et al., *Regulation of transport pathways in tumor vessels: role of tumor type and microenvironment.* Proceedings of the National Academy of Sciences, 1998. **95**(8): p. 4607-4612.
34. Bae, Y.H., *Drug targeting and tumor heterogeneity.* Journal of controlled release: official journal of the Controlled Release Society, 2009. **133**(1): p. 2.
35. Allen, T.M., *Ligand-targeted therapeutics in anticancer therapy.* Nature Reviews Cancer, 2002. **2**(10): p. 750.
36. Pirollo, K.F. and E.H. Chang, *Does a targeting ligand influence nanoparticle tumor localization or uptake?* Trends in biotechnology, 2008. **26**(10): p. 552-558.
37. Kirpotin, D.B., et al., *Antibody targeting of long-circulating lipidic nanoparticles does not increase tumor localization but does increase internalization in animal models.* Cancer research, 2006. **66**(13): p. 6732-6740.
38. Ruoslahti, E., S.N. Bhatia, and M.J. Sailor, *Targeting of drugs and nanoparticles to tumors.* The Journal of cell biology, 2010. **188**(6): p. 759-768.

39. Shi, Y. and J. Massagué, *Mechanisms of TGF-β signaling from cell membrane to the nucleus.* cell, 2003. **113**(6): p. 685-700.
40. McMahon, H.T. and J.L. Gallop, *Membrane curvature and mechanisms of dynamic cell membrane remodelling.* Nature, 2005. **438**(7068): p. 590.
41. Edidin, M., *Lipids on the frontier: a century of cell-membrane bilayers.* Nature Reviews Molecular Cell Biology, 2003. **4**(5): p. 414.
42. Behzadi, S., et al., *Cellular uptake of nanoparticles: journey inside the cell.* Chemical Society Reviews, 2017. **46**(14): p. 4218-4244.
43. Chapman, D., *Phospholipid bilayers physical principles and models. Gregor Cevc and Derek Marsh (Eds), John Wiley and Sons Ltd. xvi+ 442 pages,£ 73.35 (1987).* Cell Biochemistry and Function: Cellular biochemistry and its modulation by active agents or disease, 1988. **6**(2): p. 147-148.
44. Van Meer, G., D.R. Voelker, and G.W. Feigenson, *Membrane lipids: where they are and how they behave.* Nature reviews Molecular cell biology, 2008. **9**(2): p. 112.
45. Contini, C., et al., *Nanoparticle–membrane interactions.* Journal of Experimental Nanoscience, 2018. **13**(1): p. 62-81.
46. Kumari, S., M. Swetha, and S. Mayor, *Endocytosis unplugged: multiple ways to enter the cell.* Cell research, 2010. **20**(3): p. 256.
47. Conner, S.D. and S.L. Schmid, *Regulated portals of entry into the cell.* Nature, 2003. **422**(6927): p. 37.
48. Doherty, G.J. and H.T. McMahon, *Mechanisms of endocytosis.* Annual review of biochemistry, 2009. **78**: p. 857-902.
49. Lane, L.A., et al., *Physical chemistry of nanomedicine: understanding the complex behaviors of nanoparticles in vivo.* Annual review of physical chemistry, 2015. **66**: p. 521-547.
50. Patel, L.N., J.L. Zaro, and W.-C. Shen, *Cell penetrating peptides: intracellular pathways and pharmaceutical perspectives.* Pharmaceutical research, 2007. **24**(11): p. 1977-1992.
51. Hu, Y., et al., *Cytosolic delivery of membrane-impermeable molecules in dendritic cells using pH-responsive core− shell nanoparticles.* Nano letters, 2007. **7**(10): p. 3056-3064.
52. Wolff, J.A., et al., *Direct gene transfer into mouse muscle in vivo.* Science, 1990. **247**(4949): p. 1465-1468.

53. Rojas-Chapana, J.A., et al., *Enhanced introduction of gold nanoparticles into vital acidothiobacillus ferrooxidans by carbon nanotube-based microwave electroporation.* Nano Letters, 2004. **4**(5): p. 985-988.
54. Mu, Q., et al., *Chemical basis of interactions between engineered nanoparticles and biological systems.* Chemical reviews, 2014. **114**(15): p. 7740-7781.
55. Jiang, X., et al., *Endo-and exocytosis of zwitterionic quantum dot nanoparticles by live HeLa cells.* ACS nano, 2010. **4**(11): p. 6787-6797.
56. Swanson, J.A., *Shaping cups into phagosomes and macropinosomes.* Nature reviews Molecular cell biology, 2008. **9**(8): p. 639.
57. Hillaireau, H. and P. Couvreur, *Nanocarriers' entry into the cell: relevance to drug delivery.* Cellular and molecular life sciences, 2009. **66**(17): p. 2873-2896.
58. Schäfer, V., et al., *Phagocytosis of nanoparticles by human immunodeficiency virus (HlV)-infected macrophages: a possibility for antiviral drug targeting.* Pharmaceutical research, 1992. **9**(4): p. 541-546.
59. Tabata, Y. and Y. Ikada, *Effect of the size and surface charge of polymer microspheres on their phagocytosis by macrophage.* Biomaterials, 1988. **9**(4): p. 356-362.
60. Gustafson, H.H., et al., *Nanoparticle uptake: the phagocyte problem.* Nano today, 2015. **10**(4): p. 487-510.
61. Zhao, F., et al., *Cellular uptake, intracellular trafficking, and cytotoxicity of nanomaterials.* small, 2011. **7**(10): p. 1322-1337.
62. Fadaee-Shohada, M.J., et al., *The behaviour of both Listeria monocytogenes and rat ciliated ependymal cells is altered during their co-culture.* PloS one, 2010. **5**(5): p. e10450.
63. Cedervall, T., et al., *Understanding the nanoparticle–protein corona using methods to quantify exchange rates and affinities of proteins for nanoparticles.* Proceedings of the National Academy of Sciences, 2007. **104**(7): p. 2050-2055.
64. Cedervall, T., et al., *Detailed identification of plasma proteins adsorbed on copolymer nanoparticles.* Angewandte Chemie International Edition, 2007. **46**(30): p. 5754-5756.
65. Mortensen, N.P., et al., *Dynamic development of the protein corona on silica nanoparticles: composition and role in toxicity.* Nanoscale, 2013. **5**(14): p. 6372-6380.

66. Lynch, I., K.A. Dawson, and S. Linse, *Detecting cryptic epitopes created by nanoparticles.* Sci. Stke, 2006. **2006**(327): p. pe14-pe14.
67. Shang, L., K. Nienhaus, and G.U. Nienhaus, *Engineered nanoparticles interacting with cells: size matters.* Journal of nanobiotechnology, 2014. **12**(1): p. 5.
68. Zhu, M., et al., *Physicochemical properties determine nanomaterial cellular uptake, transport, and fate.* Accounts of chemical research, 2012. **46**(3): p. 622-631.
69. Chithrani, B.D. and W.C. Chan, *Elucidating the mechanism of cellular uptake and removal of protein-coated gold nanoparticles of different sizes and shapes.* Nano letters, 2007. **7**(6): p. 1542-1550.
70. Zhang, S., et al., *Size-dependent endocytosis of nanoparticles.* Advanced materials, 2009. **21**(4): p. 419-424.
71. Shang, L., et al., *Nanoparticle interactions with live cells: quantitative fluorescence microscopy of nanoparticle size effects.* Beilstein journal of nanotechnology, 2014. **5**(1): p. 2388-2397.
72. Meng, X. and X. Li, *Size limit and energy analysis of nanoparticles during wrapping process by membrane.* Nanomaterials, 2018. **8**(11): p. 899.
73. Yuan, H., et al., *Variable nanoparticle-cell adhesion strength regulates cellular uptake.* Physical review letters, 2010. **105**(13): p. 138101.
74. Bao, G. and X.R. Bao, *Shedding light on the dynamics of endocytosis and viral budding.* Proceedings of the National Academy of Sciences, 2005. **102**(29): p. 9997-9998.
75. Lipowsky, R. and H.-G. Döbereiner, *Vesicles in contact with nanoparticles and colloids.* EPL (Europhysics Letters), 1998. **43**(2): p. 219.
76. Decuzzi, P. and M. Ferrari, *The role of specific and non-specific interactions in receptor-mediated endocytosis of nanoparticles.* Biomaterials, 2007. **28**(18): p. 2915-2922.
77. Gao, H., W. Shi, and L.B. Freund, *Mechanics of receptor-mediated endocytosis.* Proceedings of the National Academy of Sciences, 2005. **102**(27): p. 9469-9474.
78. Chithrani, B.D., A.A. Ghazani, and W.C. Chan, *Determining the size and shape dependence of gold nanoparticle uptake into mammalian cells.* Nano letters, 2006. **6**(4): p. 662-668.

79. Cho, Y., et al., *Functional silica nanoparticle-mediated neuronal membrane sealing following traumatic spinal cord injury.* Journal of neuroscience research, 2010. **88**(7): p. 1433-1444.
80. Choi, H.S., et al., *Renal clearance of quantum dots.* Nature biotechnology, 2007. **25**(10): p. 1165.
81. Li, S.-D. and L. Huang, *Pharmacokinetics and biodistribution of nanoparticles.* Molecular pharmaceutics, 2008. **5**(4): p. 496-504.
82. Florez, L., et al., *How shape influences uptake: interactions of anisotropic polymer nanoparticles and human mesenchymal stem cells.* Small, 2012. **8**(14): p. 2222-2230.
83. Verma, A. and F. Stellacci, *Effect of surface properties on nanoparticle–cell interactions.* Small, 2010. **6**(1): p. 12-21.
84. Decuzzi, P. and M. Ferrari, *The receptor-mediated endocytosis of nonspherical particles.* Biophysical journal, 2008. **94**(10): p. 3790-3797.
85. Ferrari, M., *Nanogeometry: beyond drug delivery.* Nature Nanotechnology, 2008. **3**(3): p. 131.
86. Zhang, Y., et al., *Permission to enter cell by shape: nanodisk vs nanosphere.* ACS applied materials & interfaces, 2012. **4**(8): p. 4099-4105.
87. Harush-Frenkel, O., et al., *Targeting of nanoparticles to the clathrin-mediated endocytic pathway.* Biochemical and biophysical research communications, 2007. **353**(1): p. 26-32.
88. Leroueil, P.R., et al., *Wide varieties of cationic nanoparticles induce defects in supported lipid bilayers.* Nano letters, 2008. **8**(2): p. 420-424.
89. Fröhlich, E., *The role of surface charge in cellular uptake and cytotoxicity of medical nanoparticles.* International journal of nanomedicine, 2012. **7**: p. 5577.
90. Cho, E.C., et al., *Understanding the role of surface charges in cellular adsorption versus internalization by selectively removing gold nanoparticles on the cell surface with a I2/KI etchant.* Nano letters, 2009. **9**(3): p. 1080-1084.
91. Hirsch, V., et al., *Surface charge of polymer coated SPIONs influences the serum protein adsorption, colloidal stability and subsequent cell interaction in vitro.* Nanoscale, 2013. **5**(9): p. 3723-3732.

92. Schweiger, C., et al., *Quantification of the internalization patterns of superparamagnetic iron oxide nanoparticles with opposite charge.* Journal of nanobiotechnology, 2012. **10**(1): p. 28.
93. Patil, S., et al., *Protein adsorption and cellular uptake of cerium oxide nanoparticles as a function of zeta potential.* Biomaterials, 2007. **28**(31): p. 4600-4607.
94. Hong, S., et al., *The binding avidity of a nanoparticle-based multivalent targeted drug delivery platform.* Chemistry & biology, 2007. **14**(1): p. 107-115.
95. Montet, X., et al., *Multivalent effects of RGD peptides obtained by nanoparticle display.* Journal of medicinal chemistry, 2006. **49**(20): p. 6087-6093.
96. Carlson, C.B., et al., *Selective tumor cell targeting using low-affinity, multivalent interactions.* ACS chemical biology, 2007. **2**(2): p. 119-127.
97. Gantert, M., et al., *Receptor-Specific Targeting With Liposomes In Vitro Based on Sterol-PEG 1300 Anchors.* Pharmaceutical research, 2009. **26**(3): p. 529.
98. Lu, B., M.R. Smyth, and R. O'Kennedy, *Tutorial review. Oriented immobilization of antibodies and its applications in immunoassays and immunosensors.* Analyst, 1996. **121**(3): p. 29R-32R.
99. Salvati, A., et al., *Transferrin-functionalized nanoparticles lose their targeting capabilities when a biomolecule corona adsorbs on the surface.* Nature nanotechnology, 2013. **8**(2): p. 137.
100. Gu, F., et al., *Precise engineering of targeted nanoparticles by using self-assembled biointegrated block copolymers.* Proceedings of the National Academy of Sciences, 2008. **105**(7): p. 2586-2591.
101. de Azevedo, J., F. Walter, and R. Dias, *Experimental approaches to evaluate the thermodynamics of protein-drug interactions.* Current drug targets, 2008. **9**(12): p. 1071-1076.
102. Bronowska, A.K., *Thermodynamics of ligand-protein interactions: implications for molecular design*, in *Thermodynamics-Interaction Studies-Solids, Liquids and Gases*. 2011, IntechOpen.
103. Kastritis, P.L. and A.M. Bonvin, *On the binding affinity of macromolecular interactions: daring to ask why proteins interact.* Journal of The Royal Society Interface, 2013. **10**(79): p. 20120835.

104. Du, X., et al., *Insights into protein–ligand interactions: mechanisms, models, and methods.* International journal of molecular sciences, 2016. **17**(2): p. 144.
105. Liberman, A., et al., *Synthesis and surface functionalization of silica nanoparticles for nanomedicine.* Surface science reports, 2014. **69**(2): p. 132-158.
106. Liu, K., et al., *Hyaluronic acid-tagged silica nanoparticles in colon cancer therapy: therapeutic efficacy evaluation.* International journal of nanomedicine, 2015. **10**: p. 6445.
107. Jung, H.-S., D.-S. Moon, and J.-K. Lee, *Quantitative analysis and efficient surface modification of silica nanoparticles.* Journal of Nanomaterials, 2012. **2012**: p. 48.
108. He, X., et al., *In vivo study of biodistribution and urinary excretion of surface-modified silica nanoparticles.* Analytical chemistry, 2008. **80**(24): p. 9597-9603.
109. Bagwe, R.P., et al., *Optimization of dye-doped silica nanoparticles prepared using a reverse microemulsion method.* Langmuir, 2004. **20**(19): p. 8336-8342.
110. Zhou, Y., et al., *Mesoporous silica nanoparticles for drug and gene delivery.* Acta pharmaceutica sinica B, 2018. **8**(2): p. 165-177.
111. Watermann, A. and J. Brieger, *Mesoporous silica nanoparticles as drug delivery vehicles in cancer.* Nanomaterials, 2017. **7**(7): p. 189.
112. Jaramillo, N., C. Paucar, and C. García, *Influence of the reaction time and the Triton x-100/Cyclohexane/Methanol/H 2 O ratio on the morphology and size of silica nanoparticles synthesized via sol–gel assisted by reverse micelle microemulsion.* Journal of materials science, 2014. **49**(9): p. 3400-3406.
113. Kardys, A.Y., D.J. Bharali, and S.A. Mousa, *Amino-functionalized silica nanoparticles: In vitro evaluation for targeted delivery and therapy of pancreatic cancer.* Journal of Nanotechnology, 2013. **2013**.
114. Cho, K., et al., *Mechanisms of the formation of silica particles from precursors with different volatilities by flame spray pyrolysis.* Aerosol Science and Technology, 2009. **43**(9): p. 911-920.
115. Graham, T., *XXXV.—On the properties of silicic acid and other analogous colloidal substances.* Journal of the Chemical Society, 1864. **17**: p. 318-327.
116. Hench, L.L. and J.K. West, *The sol-gel process.* Chemical reviews, 1990. **90**(1): p. 33-72.
117. Buckley, A. and M. Greenblatt, *The sol-gel preparation of silica gels.* journal of chemical education, 1994. **71**(7): p. 599.

118. Ibrahim, I.A., A. Zikry, and M.A. Sharaf, *Preparation of spherical silica nanoparticles: Stober silica.* J. Am. Sci, 2010. **6**(11): p. 985-989.
119. Brinker, C.J. and G.W. Scherer, *Sol-gel science: the physics and chemistry of sol-gel processing*. 2013: Academic press.
120. Malik, M.A., M.Y. Wani, and M.A. Hashim, *Microemulsion method: a novel route to synthesize organic and inorganic nanomaterials: 1st nano update.* Arabian journal of Chemistry, 2012. **5**(4): p. 397-417.
121. Talegaonkar, S., et al., *Microemulsions: a novel approach to enhanced drug delivery.* Recent Patents on Drug Delivery & Formulation, 2008. **2**(3): p. 238-257.
122. Jin, Y., et al., *Silica nanoparticles with continuously tunable sizes: synthesis and size effects on cellular contrast imaging.* Chemistry of Materials, 2008. **20**(13): p. 4411-4419.
123. Lopez-Quintela, M.A., *Synthesis of nanomaterials in microemulsions: formation mechanisms and growth control.* Current Opinion in Colloid & Interface Science, 2003. **8**(2): p. 137-144.
124. Ruckenstein, E. and J. Chi, *Stability of microemulsions.* Journal of the Chemical Society, Faraday Transactions 2: Molecular and Chemical Physics, 1975. **71**: p. 1690-1707.
125. Lin, C.-H., et al., *Formation of hollow silica nanospheres by reverse microemulsion.* Nanoscale, 2015. **7**(21): p. 9614-9626.
126. Finnie, K.S., et al., *Formation of silica nanoparticles in microemulsions.* Langmuir, 2007. **23**(6): p. 3017-3024.
127. dos Santos Neves, C.S., *Development of fluorescent silica nanoparticles encapsulating organic and inorganic fluorophores; synthesis and characterization.* 2014.
128. Carpenter, A.W., et al., *Influence of scaffold size on bactericidal activity of nitric oxide-releasing silica nanoparticles.* ACS nano, 2011. **5**(9): p. 7235-7244.
129. Rahman, I.A. and V. Padavettan, *Synthesis of silica nanoparticles by sol-gel: size-dependent properties, surface modification, and applications in silica-polymer nanocomposites—a review.* Journal of Nanomaterials, 2012. **2012**: p. 8.
130. Gomes, M.C., et al., *The role of surface functionalization of silica nanoparticles for bioimaging.* Journal of Innovative Optical Health Sciences, 2016. **9**(04): p. 1630005.
131. Xu, S., S. Hartvickson, and J.X. Zhao, *Increasing surface area of silica nanoparticles with a rough surface.* ACS applied materials & interfaces, 2011. **3**(6): p. 1865-1872.

132. Yoshitake, H., *Highly-controlled synthesis of organic layers on mesoporous silica: their structure and application to toxic ion adsorptions.* New Journal of Chemistry, 2005. **29**(9): p. 1107-1117.
133. Miyajima, T., et al., *Estimation of spacing between 3-bromopropyl functions grafted on mesoporous silica surfaces by a substitution reaction using diamine probe molecules.* Journal of Materials Chemistry, 2007. **17**(37): p. 3901-3909.
134. Lu, H.-T., *Synthesis and characterization of amino-functionalized silica nanoparticles.* Colloid Journal, 2013. **75**(3): p. 311-318.
135. Naka, Y., Y. Komori, and H. Yoshitake, *One-pot synthesis of organo-functionalized monodisperse silica particles in W/O microemulsion and the effect of functional groups on addition into polystyrene.* Colloids and surfaces A: physicochemical and engineering aspects, 2010. **361**(1-3): p. 162-168.
136. Peng, F., et al., *PEGylation of G-CSF in organic solvent markedly increase the efficacy and reactivity through protein unfolding, hydrolysis inhibition and solvent effect.* Journal of biotechnology, 2014. **170**: p. 42-49.
137. Mugica, L.C., et al., *Surface functionalization of silica particles for their efficient fluorescence and stereo selective modification.* Colloids and Surfaces A: Physicochemical and Engineering Aspects, 2016. **500**: p. 79-87.
138. Soto-Cantu, E., et al., *Synthesis and rapid characterization of amine-functionalized silica.* Langmuir, 2012. **28**(13): p. 5562-5569.
139. Thanh, N.T. and L.A. Green, *Functionalisation of nanoparticles for biomedical applications.* Nano Today, 2010. **5**(3): p. 213-230.
140. Kolate, A., et al., *PEG—a versatile conjugating ligand for drugs and drug delivery systems.* Journal of controlled release, 2014. **192**: p. 67-81.
141. Zhang, W., et al., *Fluorescent proteins as efficient tools for evaluating the surface PEGylation of silica nanoparticles.* Methods and applications in fluorescence, 2017. **5**(2): p. 024003.
142. Perry, J.L., et al., *PEGylated PRINT nanoparticles: the impact of PEG density on protein binding, macrophage association, biodistribution, and pharmacokinetics.* Nano letters, 2012. **12**(10): p. 5304-5310.

143. Jokerst, J.V., et al., *Nanoparticle PEGylation for imaging and therapy.* Nanomedicine, 2011. **6**(4): p. 715-728.
144. Sharma, S., et al., *PLGA-based nanoparticles: a new paradigm in biomedical applications.* TrAC Trends in Analytical Chemistry, 2016. **80**: p. 30-40.
145. Glorani, G., et al., *Pegylated silica nanoparticles: cytotoxicity and macrophage uptake.* Journal of Nanoparticle Research, 2017. **19**(8): p. 294.
146. Xu, Q., et al., *Impact of surface polyethylene glycol (PEG) density on biodegradable nanoparticle transport in mucus ex vivo and distribution in vivo.* ACS nano, 2015. **9**(9): p. 9217-9227.
147. Bamberger, D., et al., *Surface modification of polysaccharide-based nanoparticles with PEG and dextran and the effects on immune cell binding and stimulatory characteristics.* Molecular pharmaceutics, 2017. **14**(12): p. 4403-4416.
148. Ikeda, J., et al., *Application of carbodiimide derivatized synovial fluid to enhance extrasynovial tendon gliding ability.* The Journal of hand surgery, 2011. **36**(3): p. 456-463.
149. Bart, J., et al., *Room-temperature intermediate layer bonding for microfluidic devices.* Lab on a Chip, 2009. **9**(24): p. 3481-3488.
150. Senbanjo, L.T. and M.A. Chellaiah, *CD44: a multifunctional cell surface adhesion receptor is a regulator of progression and metastasis of cancer cells.* Frontiers in cell and developmental biology, 2017. **5**: p. 18.
151. Xiao, B., et al., *Hyaluronic acid-functionalized polymeric nanoparticles for colon cancer-targeted combination chemotherapy.* Nanoscale, 2015. **7**(42): p. 17745-17755.
152. Kim, J.H., et al., *Hyaluronic acid-based nanomaterials for cancer therapy.* Polymers, 2018. **10**(10): p. 1133.
153. Almeida, P.V., et al., *Amine-modified hyaluronic acid-functionalized porous silicon nanoparticles for targeting breast cancer tumors.* Nanoscale, 2014. **6**(17): p. 10377-10387.
154. Zhong, L., et al., *Exploring the relationship of hyaluronic acid molecular weight and active targeting efficiency for designing hyaluronic acid-modified nanoparticles.* Asian Journal of Pharmaceutical Sciences, 2018.

155. Mokhtarzadeh, A., et al., *Aptamers as smart ligands for nano-carriers targeting.* TrAC Trends in Analytical Chemistry, 2016. **82**: p. 316-327.
156. Zavros, Y., *Initiation and maintenance of gastric cancer: a focus on CD44 variant isoforms and cancer stem cells.* Cellular and molecular gastroenterology and hepatology, 2017. **4**(1): p. 55-63.
157. Xu, H., et al., *The role of CD44 in epithelial–mesenchymal transition and cancer development.* OncoTargets and therapy, 2015. **8**: p. 3783.
158. Kahmann, J.D., et al., *Localization and characterization of the hyaluronan-binding site on the link module from human TSG-6.* Structure, 2000. **8**(7): p. 763-774.
159. Ma, M., et al., *Hyaluronic acid-conjugated mesoporous silica nanoparticles: excellent colloidal dispersity in physiological fluids and targeting efficacy.* Journal of Materials Chemistry, 2012. **22**(12): p. 5615-5621.
160. Song, L., et al., *Dually folate/CD44 receptor-targeted self-assembled hyaluronic acid nanoparticles for dual-drug delivery and combination cancer therapy.* Journal of Materials Chemistry B, 2017. **5**(33): p. 6835-6846.
161. Zhang, W., et al. *Synthesis and Characterization of Hyaluronic Acid Modified Colloidal Mesoporous Silica Nanoparticles*. in *IOP Conference Series: Materials Science and Engineering*. 2017. IOP Publishing.
162. Yu, M., et al., *Hyaluronic acid modified mesoporous silica nanoparticles for targeted drug delivery to CD44-overexpressing cancer cells.* Nanoscale, 2013. **5**(1): p. 178-183.
163. Yang, Y., et al., *Reduction-sensitive CD44 receptor-targeted hyaluronic acid derivative micelles for doxorubicin delivery.* International Journal of Nanomedicine, 2018. **13**: p. 4361.
164. Liu, Y., et al., *Dual targeting folate-conjugated hyaluronic acid polymeric micelles for paclitaxel delivery.* International journal of pharmaceutics, 2011. **421**(1): p. 160-169.
165. Jiang, H., et al., *Hyaluronidase Enzyme-responsive Targeted Nanoparticles for Effective Delivery of 5-Fluorouracil in Colon Cancer.* Pharmaceutical research, 2018. **35**(4): p. 73.
166. Wang, Z., et al., *Using hyaluronic acid-functionalized pH stimuli-responsive mesoporous silica nanoparticles for targeted delivery to CD44-overexpressing cancer cells.* International journal of nanomedicine, 2016. **11**: p. 6485.

167. Kim, K., et al., *Hyaluronic Acid-Coated Nanomedicine for Targeted Cancer Therapy.* Pharmaceutics, 2019. **11**(7): p. 301.
168. Sharma, M., et al., *Folic acid conjugated guar gum nanoparticles for targeting methotrexate to colon cancer.* Journal of biomedical nanotechnology, 2013. **9**(1): p. 96-106.
169. Zwicke, G.L., G. Ali Mansoori, and C.J. Jeffery, *Utilizing the folate receptor for active targeting of cancer nanotherapeutics.* Nano reviews, 2012. **3**(1): p. 18496.
170. Blanco, M., et al., *Targeted nanoparticles for cancer therapy*, in *Recent advances in novel drug carrier systems*. 2012, IntechOpen.
171. Yoo, H.S. and T.G. Park, *Folate-receptor-targeted delivery of doxorubicin nano-aggregates stabilized by doxorubicin–PEG–folate conjugate.* Journal of controlled release, 2004. **100**(2): p. 247-256.
172. Cheng, W., et al., *pH-sensitive delivery vehicle based on folic acid-conjugated polydopamine-modified mesoporous silica nanoparticles for targeted cancer therapy.* ACS applied materials & interfaces, 2017. **9**(22): p. 18462-18473.
173. Wang, Y., et al., *Targeted delivery of 5-fluorouracil to HT-29 cells using high efficient folic acid-conjugated nanoparticles.* Drug delivery, 2015. **22**(2): p. 191-198.
174. Bahrami, B., et al., *Nanoparticles and targeted drug delivery in cancer therapy.* Immunology letters, 2017. **190**: p. 64-83.
175. Li, H., et al., *In vivo near infrared fluorescence imaging and dynamic quantification of pancreatic metastatic tumors using folic acid conjugated biodegradable mesoporous silica nanoparticles.* Nanomedicine: Nanotechnology, Biology and Medicine, 2018. **14**(6): p. 1867-1877.
176. Samanta, S., L. Pradhan, and D. Bahadur, *Mesoporous lipid-silica nanohybrids for folate-targeted drug-resistant ovarian cancer.* New Journal of Chemistry, 2018. **42**(4): p. 2804-2814.
177. Handali, S., et al., *A novel 5-Fluorouracil targeted delivery to colon cancer using folic acid conjugated liposomes.* Biomedicine & Pharmacotherapy, 2018. **108**: p. 1259-1273.
178. AbouAitah, K., et al., *Folic acid–conjugated mesoporous silica particles as nanocarriers of natural prodrugs for cancer targeting and antioxidant action.* Oncotarget, 2018. **9**(41): p. 26466.

179. Sarkar, A., et al., *Targeted delivery of quercetin loaded mesoporous silica nanoparticles to the breast cancer cells.* Biochimica Et Biophysica Acta (BBA)-General Subjects, 2016. **1860**(10): p. 2065-2075.
180. Nho, T.D.T., et al., *Enhanced anticancer efficacy and tumor targeting through folate-PEG modified nanoliposome loaded with 5-fluorouracil.* Advances in Natural Sciences: Nanoscience and Nanotechnology, 2017. **8**(1): p. 015008.
181. Garcia-Bennett, A., M. Nees, and B. Fadeel, *In search of the Holy Grail: folate-targeted nanoparticles for cancer therapy.* Biochemical pharmacology, 2011. **81**(8): p. 976-984.
182. Kelemen, L.E., *The role of folate receptor α in cancer development, progression and treatment: cause, consequence or innocent bystander?* International journal of cancer, 2006. **119**(2): p. 243-250.
183. Large, D.E., et al., *Advances in Receptor-Mediated, Tumor-Targeted Drug Delivery.* Advanced Therapeutics, 2019. **2**(1): p. 1800091.
184. Elias, D.R., et al., *Effect of ligand density, receptor density, and nanoparticle size on cell targeting.* Nanomedicine: nanotechnology, biology and medicine, 2013. **9**(2): p. 194-201.
185. Rahman, I., M. Jafarzadeh, and C.S. Sipaut, *Synthesis of organo-functionalized nanosilica via a co-condensation modification using γ-aminopropyltriethoxysilane (APTES).* Ceramics International, 2009. **35**(5): p. 1883-1888.
186. Oliveira, L.F.d., et al., *Tailored silica nanoparticles surface to increase drug load and enhance bactericidal response.* Journal of the Brazilian Chemical Society, 2017. **28**(9): p. 1715-1724.
187. Yang, G., et al., *Breast Cancer Imaging with Fluoresce in Isothiocyanate-Modified Gold Nanoparticles In-Vidro and In-Vivo.* Int. J. Clin. Exp. Med, 2016. **9**: p. 753-759.
188. Meng, F., et al., *Quantitative assessment of nanoparticle biodistribution by fluorescence imaging, revisited.* ACS nano, 2018. **12**(7): p. 6458-6468.
189. Yang, H., et al., *Investigation of folate-conjugated fluorescent silica nanoparticles for targeting delivery to folate receptor-positive tumors and their internalization mechanism.* International journal of nanomedicine, 2011. **6**: p. 2023.
190. Zhou, Z., et al., *Folic acid-conjugated silica capped gold nanoclusters for targeted fluorescence/X-ray computed tomography imaging.* Journal of nanobiotechnology, 2013. **11**(1): p. 17.

191. Zhao, Q., et al., *Hyaluronic acid oligosaccharide modified redox-responsive mesoporous silica nanoparticles for targeted drug delivery.* ACS applied materials & interfaces, 2014. **6**(22): p. 20290-20299.
192. Grassian, V.H., *When size really matters: size-dependent properties and surface chemistry of metal and metal oxide nanoparticles in gas and liquid phase environments.* The Journal of Physical Chemistry C, 2008. **112**(47): p. 18303-18313.
193. Buzea, C., I.I. Pacheco, and K. Robbie, *Nanomaterials and nanoparticles: sources and toxicity.* Biointerphases, 2007. **2**(4): p. MR17-MR71.
194. Ajdary, M., et al., *Health concerns of various nanoparticles: a review of their in vitro and in vivo toxicity.* Nanomaterials, 2018. **8**(9): p. 634.
195. Lewinski, N., V. Colvin, and R. Drezek, *Cytotoxicity of nanoparticles.* small, 2008. **4**(1): p. 26-49.
196. Knox, P., et al., *The FRAME multicentre project on in vitro cytotoxicology.* Food and Chemical Toxicology, 1986. **24**(6-7): p. 457-463.
197. Lin, W., et al., *In vitro toxicity of silica nanoparticles in human lung cancer cells.* Toxicology and applied pharmacology, 2006. **217**(3): p. 252-259.
198. Kim, I.-Y., et al., *Toxicity of silica nanoparticles depends on size, dose, and cell type.* Nanomedicine: Nanotechnology, Biology and Medicine, 2015. **11**(6): p. 1407-1416.
199. Wang, F., et al., *Oxidative stress contributes to silica nanoparticle-induced cytotoxicity in human embryonic kidney cells.* Toxicology in vitro, 2009. **23**(5): p. 808-815.
200. Dong, X., et al., *The Size-dependent Cytotoxicity of Amorphous Silica Nanoparticles: A Systematic Review of in vitro Studies.* International Journal of Nanomedicine, 2020. **15**: p. 9089.
201. Khlebtsov, N. and L. Dykman, *Biodistribution and toxicity of engineered gold nanoparticles: a review of in vitro and in vivo studies.* Chemical Society Reviews, 2011. **40**(3): p. 1647-1671.
202. Kong, B., et al., *Experimental considerations on the cytotoxicity of nanoparticles.* Nanomedicine, 2011. **6**(5): p. 929-941.
203. AbouAitah, K., et al., *Targeted nano-drug delivery of colchicine against colon cancer cells by means of mesoporous silica nanoparticles.* Cancers, 2020. **12**(1): p. 144.

204. Canta, M. and V. Cauda, *The investigation of the parameters affecting the ZnO nanoparticles cytotoxicity behaviour: a tutorial review.* Biomaterials Science, 2020.
205. Ouasti, S., et al., *The CD44/integrins interplay and the significance of receptor binding and re-presentation in the uptake of RGD-functionalized hyaluronic acid.* Biomaterials, 2012. **33**(4): p. 1120-1134.
206. Shaheen, S., et al., *Patient Selection and Toxicities of PRRT for Metastatic Neuroendocrine Tumors and Research Opportunities.* Current Treatment Options in Oncology, 2020. **21**(3): p. 1-19.
207. Arora, G., et al., *PLGA nanoparticles for peptide receptor radionuclide therapy of neuroendocrine tumors: a novel approach towards reduction of renal radiation dose.* PLoS One, 2012. **7**(3): p. e34019.
208. Raphael, M.J., et al., *Principles of diagnosis and management of neuroendocrine tumours.* Cmaj, 2017. **189**(10): p. E398-E404.
209. Herrera-Martínez, A.D., et al., *Targeted systemic treatment of neuroendocrine tumors: current options and future perspectives.* Drugs, 2019. **79**(1): p. 21-42.
210. Sansone, A., et al., *Specific and non-specific biomarkers in neuroendocrine gastroenteropancreatic tumors.* Cancers, 2019. **11**(8): p. 1113.
211. Chan, J.A. and M.H. Kulke, *Progress in the treatment of neuroendocrine tumors.* Current oncology reports, 2009. **11**(3): p. 193-199.
212. Wu, Y., et al., *Cytotoxicity and cellular uptake of amorphous silica nanoparticles in human cancer cells.* Particle & Particle Systems Characterization, 2015. **32**(7): p. 779-787.
213. Yu, J., et al. *Effects of physicochemical properties of zinc oxide nanoparticles on cellular uptake*. in *Journal of Physics: Conference Series*. 2011. IOP Publishing.
214. Feng, S., et al., *Folate-conjugated, mesoporous silica functionalized boron nitride nanospheres for targeted delivery of doxorubicin.* Materials Science and Engineering: C, 2019. **96**: p. 552-560.
215. Saneja, A., et al., *Development and mechanistic insight into enhanced cytotoxic potential of hyaluronic acid conjugated nanoparticles in CD44 overexpressing cancer cells.* European Journal of Pharmaceutical Sciences, 2017. **97**: p. 79-91.

216. Edelman, R., et al., *Hyaluronic acid-serum albumin conjugate-based nanoparticles for targeted cancer therapy.* Oncotarget, 2017. **8**(15): p. 24337.
217. Alkilany, A.M., et al., *Ligand density on nanoparticles: A parameter with critical impact on nanomedicine.* Advanced drug delivery reviews, 2019. **143**: p. 22-36.
218. Cao, J., et al., *The effects of ligand valency and density on the targeting ability of multivalent nanoparticles based on negatively charged chitosan nanoparticles.* Colloids and Surfaces B: Biointerfaces, 2018. **161**: p. 508-518.
219. Wang, M. and M. Thanou, *Targeting nanoparticles to cancer.* Pharmacological research, 2010. **62**(2): p. 90-99.
220. Wu, J.-l., et al., *Preparation and characterization of nanoparticles based on histidine–hyaluronic acid conjugates as doxorubicin carriers.* Journal of Materials Science: Materials in Medicine, 2012. **23**(8): p. 1921-1929.
221. El-Hammadi, M.M., et al., *Folic acid-decorated and PEGylated PLGA nanoparticles for improving the antitumour activity of 5-fluorouracil.* International journal of pharmaceutics, 2017. **516**(1-2): p. 61-70.
222. Malekmohammadi, S., H. Hadadzadeh, and Z. Amirghofran, *Preparation of folic acid-conjugated dendritic mesoporous silica nanoparticles for pH-controlled release and targeted delivery of a cyclometallated gold (III) complex as an antitumor agent.* Journal of Molecular Liquids, 2018. **265**: p. 797-806.
223. Chuacharoen, T. and C.M. Sabliov, *Zein nanoparticles as delivery systems for covalently linked and physically entrapped folic acid.* Journal of Nanoparticle Research, 2017. **19**(2): p. 81.
224. Zhao, X., et al., *Double-cross-linked hyaluronic acid nanoparticles with pH/reduction dual-responsive triggered release and pH-modulated fluorescence for folate-receptor-mediated targeting visualized chemotherapy.* Biomacromolecules, 2016. **17**(4): p. 1496-1505.
225. Moradi, E., et al., *Ligand density and clustering effects on endocytosis of folate modified nanoparticles.* RSC Advances, 2012. **2**(7): p. 3025-3033.